METALAMPROPHYRE DIKE DEFORMATION IN THE HOMESTAKE RESERVOIR QUADRANGLE, LEADVILLE, COLORADO

by

Michael Geoffrey Frothingham

A thesis submitted in partial fulfillment
of the requirements for the degree

of

Master of Science

in

Earth Sciences

MONTANA STATE UNIVERSITY
Bozeman, Montana

April 2017

ACKNOWLEDGEMENTS

Colin A. Shaw is gratefully acknowledged as my supervisor and for the direction and revision of this project. Additional committee members are Mary S. Hubbard and David W. Mogk. This work was undertaken with partial financial assistance from the Graduate School at Montana State University, the United States Geological Survey EDMAP grant number G15AC00175, the Montana Association of Geographic Information Professionals, the Barry C. Bishop Scholarship at Montana State University, and NSF award number 1525590 to Concord University (J. Allen and S. Kuehn).

I would also like to thank my family, friends, Flysch, undergraduate research assistants Natali Kragh and Matthew Mersen, fellow graduate students in the bullpen, and Chester A. Ruleman of the USGS; because of whom my life, research, and future career as a field geologist are fundamentally metamorphosed.

TABLE OF CONTENTS

TABLE OF CONTENTS — CONTINUED

TABLE OF CONTENTS — CONTINUED

LIST OF TABLES

Table Page

LIST OF FIGURES

Figure Page

LIST OF FIGURES — CONTINUED

Figure Page

LIST OF PLATES

ABSTRACT

Field relations and microstructural observations show that intrusion of mafic, ultrapotassic, lamprophyre dikes in the Northern Sawatch Range near Leadville, Colorado localized shear zone deformation ca. 1.4 Ga. This suggests that lithologic contrasts and advective heating associated with magmatism contributed to localizing intracontinental deformation associated with a widespread tectonothermal event that affected the southwestern U.S. during the Mesoproterozoic. Dikes are concentrated in a distinct structural domain characterized by east striking, subvertical foliations in a localized zone of Paleoproterozoic hornblende gneiss, calc-silicate gneiss, and biotite gneiss country rock. Observations show that preexisting fabrics in Proterozoic units preferentially localized north south extension, which accommodated dike emplacement. Following emplacement, dikes were metamorphosed and sheared along their margins within relatively unaffected country rock. The *TitaniQ* titanium and quartz thermometer yields deformation temperatures in dikes of at least 564 ±45 ºC, hotter than previously calculated deformation temperatures of mylonite in the nearby Homestake Shear Zone (HSZ) and similar to deformation temperatures of the nearby Slide Lake Shear Zone (SLSZ). This implies that during deformation, the dikes were still hot from their recent intrusion and this may have localized early stages of progressive strain accumulation. Dike emplacement and subsequent deformation demonstrates that strain was more widely distributed than in previously mapped, strictly defined 1.4 Ga shear zones. This study identifies how the newly recognized element of strain partitioning in mafic dikes, in addition to coeval emplacement of St. Kevin batholith and deformation in the HSZ and SLSZ, suggests a multi-faceted, kinematically-linked system of deformation ca. 1.4 Ga, which illustrates the dynamic middle continental crustal effects of Proterozoic intracontinental deformation.

CHAPTER ONE

INTRODUCTION

Proterozoic accretion, deformation, and cratonization of Laurentia has been highly enigmatic for decades due to complex field relations and convolution by over a billion years of geologic overprinting. This research focuses on unraveling the Paleoproterozoic and Mesoproterozoic geologic history in the Northern Sawatch Range, Colorado. Characterization of middle crustal igneous intrusion and deformation addresses the controversial timing and styles of tectonic activity in the Yavapai and Mazatzal terranes. Modern geologic mapping, structural analysis, kinematic analysis, and quartz thermometry in this study provide an improved understanding of Mesoproterozoic tectonism, contributing to a vast body of research on the Proterozoic assembly and deformation of Laurentia, spearheaded by Paul Hoffman's (1988) seminal paper, "United Plates of America, The Birth of a Craton."

Proterozoic igneous and metamorphic rock exposures in the Northern Sawatch Range near Leadville, Colorado offer an exemplary glimpse of ancient intracontinental deformation that occurred during the early phases of continental stabilization, following accretion of the Archean and Proterozoic provinces of southwest Laurentia (Hoffman, 1988; Karlstrom and Bowring, 1988). Outcrops in and surrounding the Homestake Reservoir quadrangle display evidence for Paleoproterozoic assembly and deformation, as well as a complex interaction between Mesoproterozoic localized dike intrusion, granitic batholith emplacement, and mylonitic shear zone deformation in the middle

continental crust (Figure 1) (Shaw et al., 2001; Tweto and Sims, 1963). The research area lies along the northeast trending Colorado Mineral Belt (CMB) shear zone system (McCoy et al., 2005), which provides fundamental exposures of Mesoproterozoic tectonism in Laurentia. Along with major Mesoproterozoic shear zones, tectonism in the Homestake Reservoir and surrounding quadrangles demonstrate how intracontinental deformation may occur hundreds of kilometers from a plate boundary (Nyman et al., 1994).

This research identifies how localized, advective heating from igneous intrusions and concentrated deformation along favorably oriented structures may provide kinematic links between dikes, batholiths, and shear zones in the Northern Sawatch Range. This work challenges previous models which suggest that continental lithosphere stabilized into a relatively undeformable craton ca. 1.6 Ga in the late Paleoproterozoic (Hoffman, 1988; Karlstrom and Bowring, 1988; Whitmeyer and Karlstrom, 2007). Instead, tectonism in the Northern Sawatch Range supports models by Daniel et al. (2013) in which the final accretion of the Mazatzal province to southern Laurentia occurred during the Mesoproterozoic Era.

Location

Geologic mapping and research was conducted primarily in and immediately surrounding the Homestake Reservoir USGS 7.5’ quadrangle, approximately 10 km west of Leadville, Colorado (Figure 1). The Homestake Reservoir quadrangle is bounded by latitude 39.25° to 39.375° N and longitude 106.5° to 106.375°. The quadrangle contains

the continental divide within the Northern Sawatch Range of the Southern Rocky Mountains (Figure 1). Elevation ranges from approximately 3000 m in the valleys to over 4000 m at Homestake Peak. Outcrops are found along mountain creeks, reservoirs, cirque lakes, ridges, and peaks above tree line. The quadrangle is accessed by vehicle from Glenwood Springs from the West, Redcliff and Vail from the North, and Leadville from the East. Travel within the northern half the quadrangle is mostly by foot in the Holy Cross Wilderness of the White River National Forest.

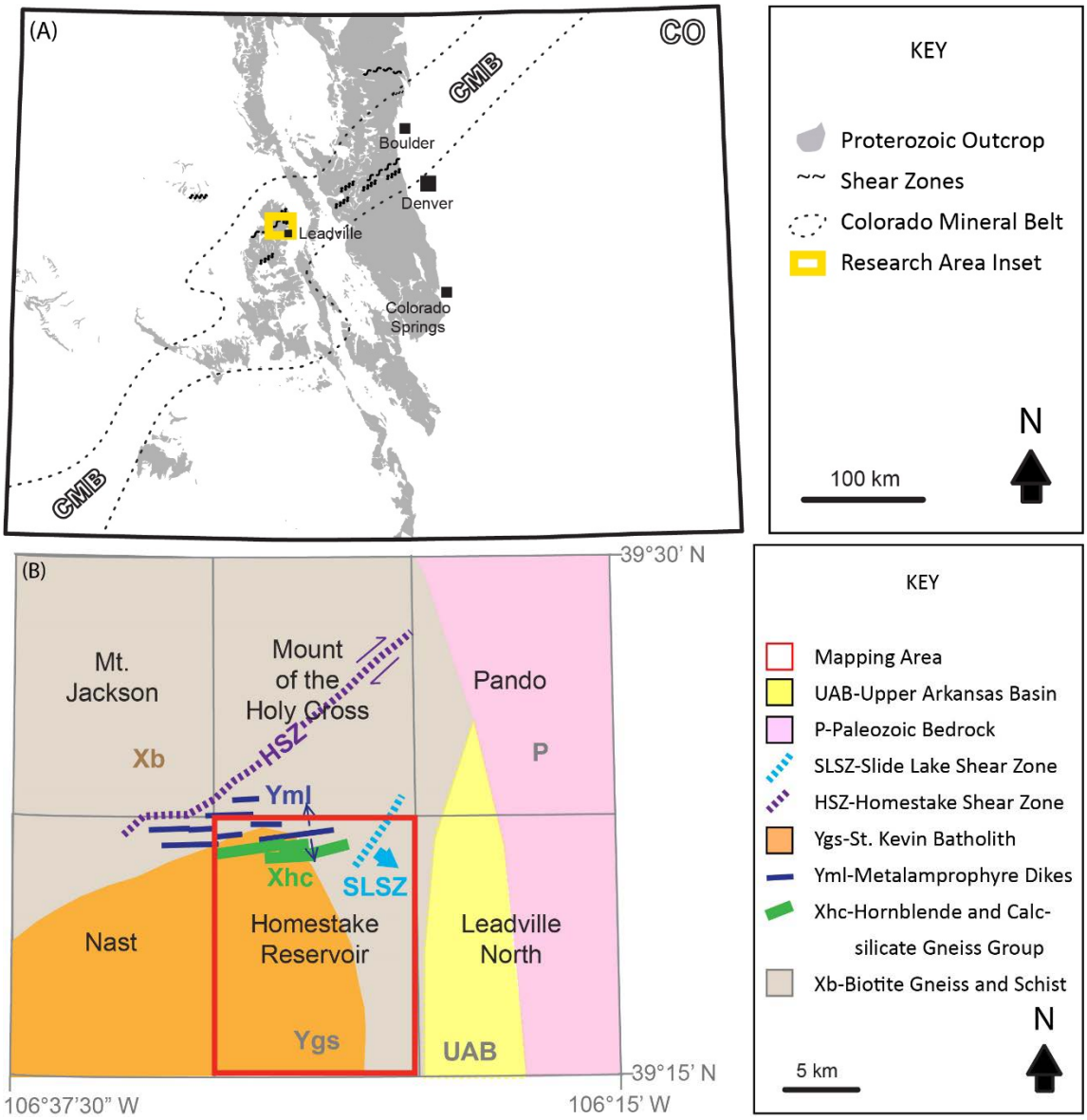

Figure 1. Location map. (A) Map of Colorado showing location of research area inset, Proterozoic outcrop in basement cored uplifts of the Colorado Southern Rocky Mountains, Shear Zones, and CMB. Adapted from (Allen and Shaw, 2013). (B) Inset map of research area, 7.5' quadrangles, generalized geology, and spatial relations between Proterozoic country rock, dikes, granite, and shear zones. Adapted from (Allen and Shaw, 2013; Lee et al., 2012; Tweto, 1974).

Geologic Setting of the Northern Sawatch Range

The Northern Sawatch Range is a basement-cored uplift in the Southern Rocky Mountains, in which Proterozoic basement is uplifted to over 4300 m. The Northern Sawatch Range consists of a north-plunging arch of Paleozoic bedrock on top of an exposed core of Precambrian basement (Figure 1), forming the "Great Unconformity" (Powell, 1876). Proterozoic basement includes varieties of metasedimentary gneiss, schist, mafic dikes, granite, and pegmatite overprinted by shear zone tectonites (Tweto, 1974). Paleozoic bedrock includes sandstone, dolomite, and other sedimentary rocks (Lovering and Goddard, 1950). Cretaceous to Oligocene magmatic and hydrothermal rocks pervasively intrude into the bedrock, contributing to mineralization in the northeast trending Colorado Mineral Belt (CMB) (Chapin, 2012; Tweto and Sims, 1963). Just east of the Sawatch Range is the northern extent of the Rio Grande Rift and associated Cenozoic faults (Chapin and Cather, 1994; Tweto, 1961), now occupied by the Tennessee Creek and Arkansas River basins. Pleistocene glaciation covered the high alpine terrain in the Northern Sawatch Range, and contributed to cirques, glacial valleys, and extensive moraines (Tweto, 1974).

Regional Tectonic History

Paleoproterozoic

Regional tectonic history begins with the amalgamation of Archean cratons along early Paleoproterozoic orogenic belts ca. 2.0-1.8 Ga in northern Laurentia, including for example the collision between the Archean and Superior Provinces represented by the ca.

1.9 Ga Trans Hudson Orogeny (Figure 2) (Hoffman, 1988; Karlstrom and Bowring, 1988; Whitmeyer and Karlstrom, 2007). This first stage of continental assembly produced the core of the Laurentian continent.

Prolonged accretion of juvenile arc-derived terranes along the southwestern Laurentian margin followed assembly of the Archean cratonic core. The Yavapai Province was formed as ca. 1.8-1.7 Ga juvenile island arcs were accreted onto the southern margin of Laurentia, separated via the Cheyenne Belt suture from the Archean Wyoming Province to the north (Figure 2) (Karlstrom and Humphreys, 1998; Van Schmus et al., 2007). Following formation of the Yavapai Terrane ca. 1.7 Ga, two different models prevail for the timing and style of accretion and deformation of the Mazatzal terrane.

Mazatzal Province — Model 1

In the first model, the Mazatzal Province was formed as ca. 1.7-1.6 Ga juvenile island-arcs accreted to the Yavapai Province along the southern margin of Laurentia (Bennett and DePaolo, 1987; Condie, 1980; Karlstrom and Bowring, 1993; Karlstrom and Bowring, 1988). Following accretion of the Yavapai and Mazatzal provinces, A-type magmatism perforated the tectonostratigraphic terranes approximately coeval to the accretion of ca. 1.5-1.4 Ga juvenile crust to southern Laurentia as the Granite-Rhyolite Province (Bickford and Van Schmus, 1985; Lidiak et al., 1966). In Model 1, Mesoproterozoic deformation in the southwestern U.S. is a distal inboard effect of plate margins where evidence for ca. 1.4 Ga tectonism is preserved within the ca. 1.1 Ga Grenville orogeny (Gower et al., 1990; Rivers, 1997).

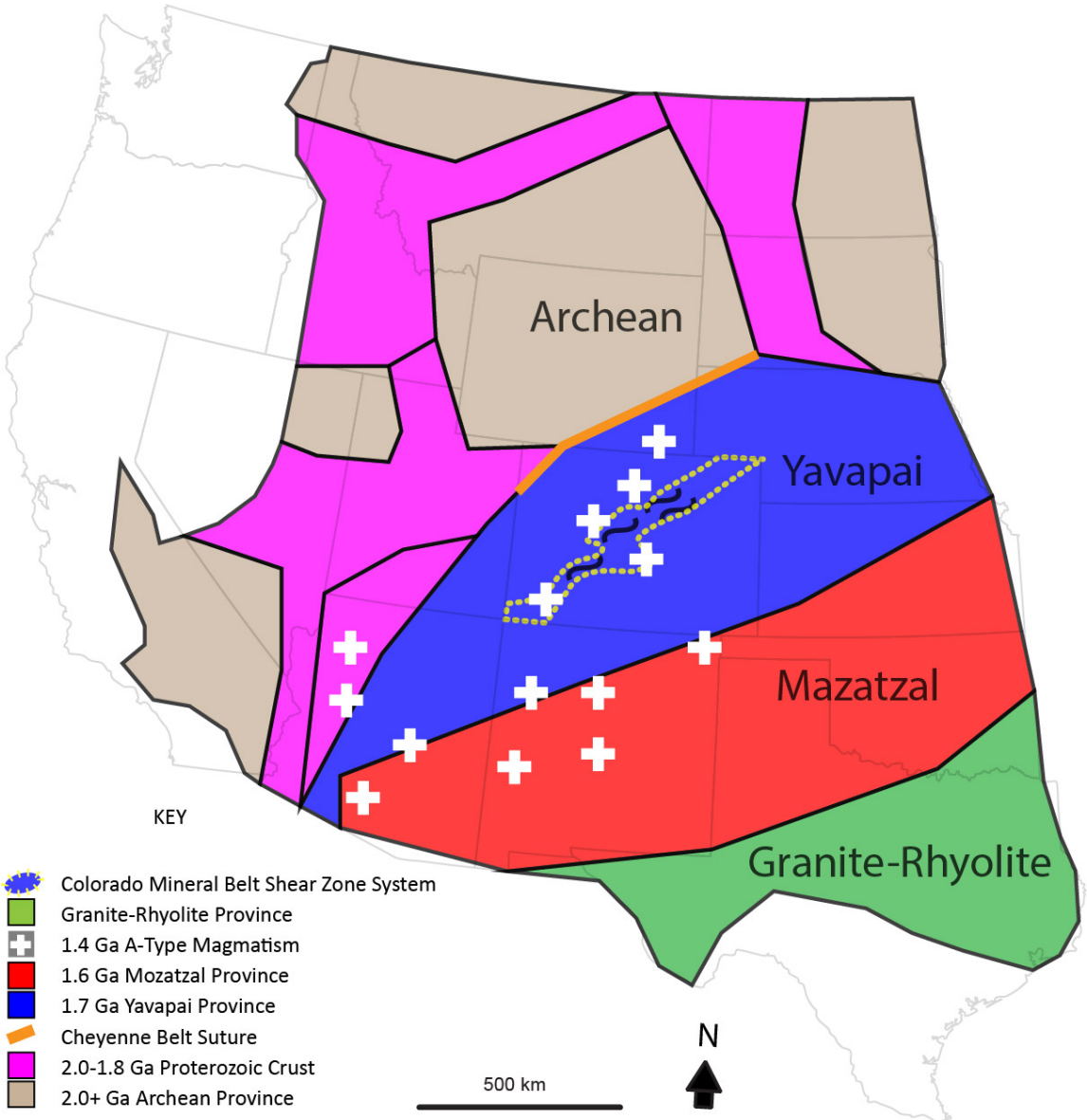

Figure 2. Geologic province map of southwest Laurentia ca. 1.4 Ga. Model 1 representation of Proterozoic accretion of Archean, Yavapai, Mazatzal, and Granite-Rhyolite Provinces overprinted by Mesoproterozoic magmatism and shear zone deformation. Adapted from (Aronoff et al., 2016; Daniel et al., 2013; Jones et al., 2015; McCoy et al., 2005; Whitmeyer and Karlstrom, 2007).

Mazatzal Province — Model 2

The second model fundamentally differs from the first by proposing the accretion and deformation of island arcs in the Mazatzal province ca. 1.4 Ga (Figure 3) (Aronoff et

al., 2016; Daniel et al., 2013; Jones et al., 2015), instead of ca. 1.6 Ga (Hoffman, 1988; Karlstrom and Bowring, 1988; Whitmeyer and Karlstrom, 2007). Following the Yavapai accretion ca. 1.7 Ga, the second model proposes a tectonic lull from ca. 1.7 Ga until ca. 1.4 Ga when significant activity resumes across the continent. Widespread ca. 1.4 Ga tectonic activity throughout Laurentia includes basin subsidence and sedimentation (Jones et al., 2015; Winston and Link, 1993), pervasive magmatism (Frost and Frost, 1997; Silver et al., 1977), intracontinental shear zone deformation (McCoy et al., 2005; Tweto and Sims, 1963), and the newly identified compressional Picuris Orogeny (Aronoff et al., 2012; Daniel et al., 2013).

The newly identified, Picuris Orogeny is a Mesoproterozoic contractional event associated with magmatism and deformation in the Picuris and Tusas mountains of northern New Mexico (Figure 3) (Aronoff et al., 2016; Daniel et al., 2013; Jones et al., 2015). Sediments of the Pilar, Piedre Lumbre, and Marqueñas Formations in the Trampas/Picuris basin show U-Pb detrital zircon maximum depositional ages of ca. 1490-1450 Ma (Daniel et al., 2013). Sedimentation was followed by basin closure, crustal thickening, and regional aluminosilicate triple-point metamorphism of the metasediments. Lu-Hf garnet ages suggest amphibolite facies metamorphism ca. 1.46 to 1.40 Ga, unique from higher grade metamorphism associated with the ca. 1.7-1.6 Ga deformation of the Yavapai and Mazatzal provinces (Aronoff et al., 2016). Models from Daniel et al. (2013) suggest that the Picuris Orogeny may represent the final accretion of the Mazatzal to Yavapai Provinces in a compressional to transpressional setting. The

Picuris Orogeny provides an essential tectonic link to other widespread geologic activity ca. 1.4 Ga throughout Laurentia.

Mesoproterozoic

Leading up to the Picuris Orogeny, regional Mesoproterozoic activity began with significant sedimentation in the Picuris/Trampas Basin in northern New Mexico, correlative to sedimentation in the Belt-Purcell basin in Montana, Idaho, and British Columbia (Figure 3) (Aronoff et al., 2016; Daniel et al., 2013; Jones et al., 2015; Winston and Link, 1993). The onset of sedimentation in the Picuris/Trampas basin is identified by U-Pb detrital zircon ages suggesting maximum depositional ages of the lower and middle Marqueñas formation ca. 1472 ±18 Ma, the Pilar formation ca. 1488 ±6 Ma, and Piedra Lumbre formation ca. 1475 ±19 Ma (Aronoff et al., 2016; Daniel et al., 2013). This data is supported by models of deposition in marine forearc basins in between the Yavapai and Mazatzal Provinces.

Mesoproterozoic rifting and deposition in the correlative Belt-Purcell Basin is identified by U-Pb zircon ages of rift-related igneous units to be ca. 1.47-1.40 Ga (Anderson and Davis, 1995; Doughty and Chamberlain, 1996; Evans et al., 2000; Jones et al., 2015; Sears et al., 1998), although the timing of earliest sedimentation is unclear. This basin is identified as an intracontinental rift system supported by various models of continental to shallow water deposition in a marine or non-marine environment (Frank et al., 1997; Winston and Link, 1993). While direct tectonic linkage to other deformation in Laurentia is not well documented, broadly correlative sedimentation in the Belt-Purcell basin does support widespread Mesoproterozoic tectonism.

Abundant Mesoproterozoic plutons within the Yavapai and Mazatzal provinces such as the ca. 1.44 Ga Mt. Evans pluton in central Colorado, ca. 1.42 Ga Sandia pluton in central New Mexico, ca. 1.4 Ga Signal pluton in western Arizona are spatially and temporally linked along their margins with nearby deformation features and suggest tectonically assisted emplacement (Figure 2) (Nyman et al., 1994; Nyman and Karlstrom, 1997). Many geologists have argued that the previously mentioned, peraluminous to metaluminous A-type magma was “anorogenic” and not sourced from a compressional orogenic event, largely based on geochemical arguments (Anderson and Bender, 1989; Frost and Frost, 1997, 2013; Silver et al., 1977). Syn-magmatic deformation of these plutons; however, suggests emplacement during regional NW-SE crustal shortening (Aronoff et al., 2016; Daniel et al., 2013; Nyman et al., 1994; Nyman and Karlstrom, 1997; Tweto and Sims, 1963; Whitmeyer and Karlstrom, 2007). Associated regional strain and pluton-enhanced metamorphism suggest emplacement in a regional compressional to transpressional intracontinental event (Nyman et al., 1994; Shaw et al., 2005).

Mesoproterozoic intracontinental shear zone deformation occurred throughout the CMB shear zone system (McCoy et al., 2005) including the Black Canyon, Homestake (HSZ), Slide Lake (SLSZ), Gore Range, Saint Louis Lake, and Idaho Springs-Ralston Shear zones (Figure 2) (Jessup et al., 2005; Lee et al., 2012; Shaw et al., 2001; Tweto and Sims, 1963). Multiple U-Th-Pb monazite crystallization ages demonstrate ca. 1.45-1.38 Ga middle crustal shear zone reactivation of Proterozoic host rocks previously deformed ca. 1.6-1.7 Ga (McCoy et al., 2005; Shaw et al., 2001). Shear zones are oriented with

approximately northeast strikes and subvertical dips, with steeply plunging mineral lineations. Kinematic indicators suggest repeated dip-slip motion involving jostling of blocks, potentially facilitating coeval ca. 1.4 Ga magmatism (McCoy et al., 2005).

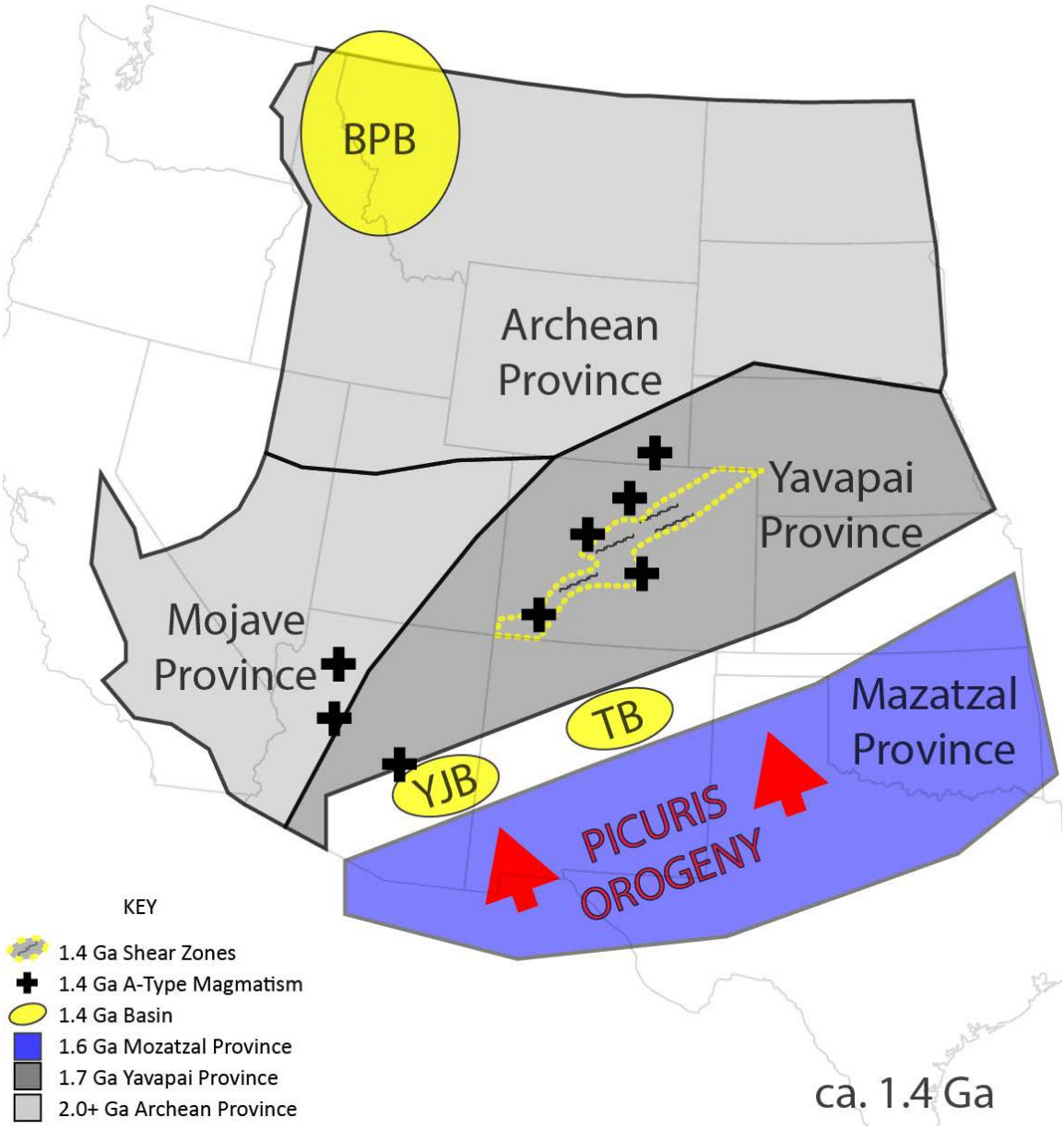

Figure 3. Model 2 tectonics of the Picuris Orogeny ca. 1.4 Ga. Representation of Paleoproterozoic accretion of Archean, Mojave, and Yavapai provinces followed by Mesoproterozoic accretion of Mazatzal terrane; Yankee Joe (YJB), Trampas (TB), and Belt-Purcell (BPB) basin sedimentation, magmatism, and shear zone deformation. Adapted from (Daniel et al., 2013; Jones et al., 2015).

Late Mesoproterozoic to Neoproterozoic

The compressional Grenville Orogeny and intracratonic extension dominated southern Laurentian tectonics in the Late Mesoproterozoic to Neoproterozoic (Dalziel, 1991; Moores, 1991). Evidence of this includes ductile deformation in south to southeastern Laurentia ca. 1.3 Ga (Daly and McLelland, 1991; Gordon and Hempton, 1986), intracratonic basins in Colorado and New Mexico ca. 1.25-1.10 Ga (Whitmeyer and Karlstrom, 2007), the failed Mid Continent Rift ca. 1.1 Ga (Halls and Pesonen, 1982; McWilliams and Dunlop, 1978; Paces and Miller, 1993), followed by the successful rifting on the western and eastern margins of Laurentia ca. 0.7-0.6 Ga (Dalziel, 1991; Karlstrom et al., 1999; Moores, 1991).

Phanerozoic

A broad, generalized tectonic overview of the Phanerozoic is included to identify the geologic context in which middle crustal rocks were exhumed, as well as the economic and social implications of their exposure. Following a significant gap in the geologic record represented by the “Great Unconformity” (Lovering and Goddard, 1950; Powell, 1876), Paleozoic fluvial, eolian, and marine sediments, followed by Mesozoic sediments were deposited on top of the exhumed Proterozoic middle crust (Tweto et al., 1978; Tweto and Sims, 1963). Reactivation of Proterozoic shear zones also occurred in the Cambrian and Ordovician, creating offset and onlap of these Early Paleozoic sediments (Allen, 2004).

The Sevier Orogeny deformed the western North American continent as far east as the Sevier Overthrust Belt (Armstrong, 1968; Heller et al., 1986), and influenced

tectonic subsidence and deposition in the Western Cretaceous Interior Seaway. Overlapping in time with the waning Sevier Orogeny to the west, the intracontinental Laramide Orogeny played major roles in deforming, uplifting, mineralizing, and importantly exposing the much of the bedrock for geologic research in the southern Rocky Mountains (Figure 1) (Dickinson and Snyder, 1978). Mineralization in the CMB approximately follows the trends of Proterozoic CMB shear zone system, suggesting that inherited zones of weakness may have provided conduits for mineralization (McCoy et al., 2005; Pearson et al., 1962; Tweto and Sims, 1963). Basin and Range tectonism subsequently thinned and extended the crust of western North America as far east as the Rio Grande Rift on the eastern side of the Colorado Plateau (Tweto, 1975, 1979). The Arkansas Graben, part of the northern Rio Grande Rift affects the eastern part of the field area (Tweto, 1961). Magmatism of the Rio Grande Rift may have also influenced mineralization ca. 33 Ma in the CMB, particularly in the Climax Molybdenum mine near Leadville, Colorado (Chapin, 2012).

Previous Mapping

Previous mapping in or near the Homestake Reservoir quadrangle emphasizes general geology, mineral resources, and shear zone deformation. Previous USGS quadrangle maps in the area include the “Geology of the Tennessee Pass Area, Eagle and Lake Counties, Colorado” by Tweto (1956), “Geologic map of the Leadville 1 degree by 2 degrees Quadrangle, northwestern Colorado” by Tweto (1974), “The Rio Grande rift system in Colorado: Rio Grande Rift: Tectonics and Magmatism” by Tweto et al. (1978),

Tweto (1979), and “Geologic map of the Holy Cross Wilderness, Eagle, Pitkin, and Lake counties, Colorado” by Wallace et al. (1986). Previous mineral resource maps include Pearson et al. (1962); Wallace et al. (1989). Shear zone deformation maps include Shaw et al. (2001), Shaw and Allen (2007), Lee et al. (2012) and Allen and Shaw (2013).

CHAPTER TWO

METHODS

To investigate the intrusion and deformation of dikes, batholiths, and shear zones, research methods includes a combination of field-based measurements, sample collection, and geologic mapping along with laboratory-based microscope petrography, kinematic analysis, geospatial evaluation of map data, and deformation thermometry. Geologic mapping enables characterization of unique structural domains and provides the geologic framework for kinematic analysis of mafic, ultra-potassic metalamprophyre dikes. Deformation analysis of metalamprophyres evaluates dike orientation, shear sense, relative age, and conditions of deformation with respect to other coeval deformation in the HSZ and SLSZ in the Homestake Reservoir quadrangle.

Field Work

Data Collection and Field Mapping

Geologic mapping and field data collection was conducted during summer 2015 and summer 2016 in and surrounding the Homestake Reservoir quadrangle (Figure 1). Structural measurements of contacts, faults, foliations, lineations, shear sense indicators, and cross cutting relations were recorded and mapped on a 1:24,000 scale, 7.5' topographic basemap of the Homestake Reservoir quadrangle (U.S.G.S., 2016). UTM zone 13N coordinates for each measurement were measured with a Garmin Montana 610 GPS®.

Sample Collection

Field data and mapping was supplemented by collection of oriented rock samples for petrographic, microstructural, and electron microprobe analysis. Following procedures outlined by Passchier and Trouw (2005), samples were oriented in situ by measuring and marking the strike and dip of a smooth surface on the rock itself (Figure 4). This measurement was preferably along a foliation plane for ease of measurement and orientation of thin sections. After strike, dip, and lineations were marked, then the sample was removed from the outcrop. Each sample was numbered and related to its geographic coordinates and other relevant geologic map data.

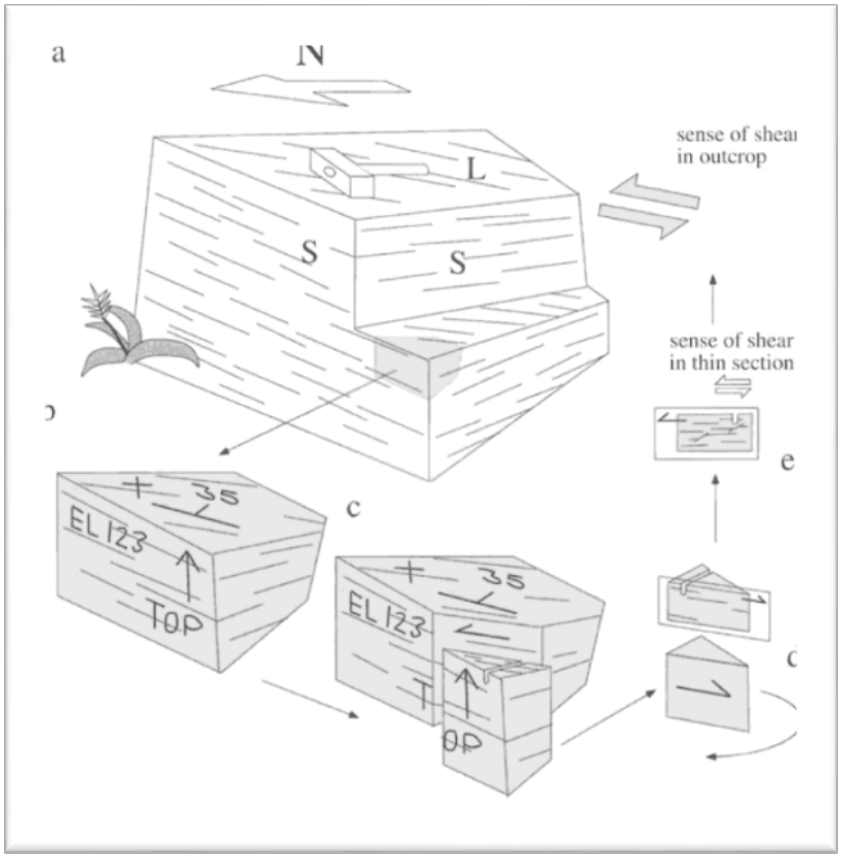

Figure 4. Outcrop and laboratory sample orientations. (a) Orientation of foliations “S” and lineations “L” in outcrop. (b) Collected sample orientation. (c) Billet orientation. (d) Thin section orientation. (e) Sense of shear in thin section. After Passchier and Trouw (2005).

Laboratory Work

Map Digitization

Laboratory work was conducted at Montana State University during academic years 2015-2016 and 2016-2017. Digitization of map data began with entering field measurements into Microsoft Excel® spreadsheets (Appendix B, Appendix C) containing relevant geographic coordinates, structural data, geologic unit or deformation type, and other notes. These spreadsheets were then formatted into database files, imported into

ArcGIS® v. 10.3.1, and then turned into point shapefiles with appropriate map symbology. Map data was then superimposed over a georeferenced 1:24,000 scale, USGS 7.5' quadrangle topographic basemap of the Homestake Reservoir (Plate I) (U.S.G.S., 2016). Geologic units, contacts, and faults from the paper field map were then digitized into polygon and polyline shapefiles onto the map.

When sharp, definitive contacts between metamorphic country rocks and igneous intrusions could not be precisely found in the field, gradational contacts were estimated using geospatial statistical analysis. Non-distinct, gradational and interfingering contacts were mapped as mixed rock based on the map density of a given rock type, and proximity to other units using location and attribute queries in ArcGIS® v. 10.3.1. If within a 300 m sampling radius, neither the metamorphic host nor igneous rock unit made up at least two thirds of the sampled rock population, then it was designated and mapped as mixed rock (Appendix A). If contacts between adjacent units were sharp and definitive in the field, they were digitized as they were originally mapped.

Stereonets

Stereonets were created from digitized map data using Stereonet 9® (Allmendinger et al., 2011; Cardozo and Allmendinger, 2013) for analysis on structural domain maps, cross sections, and kinematics. All stereonets were plotted on equal area, lower hemisphere projections. Metamorphic foliations, contacts, or fault planes were mapped as planes symbolized as black, gray, dashed, and solid great circles. Poles to planes were created and symbolized as gray or black points to show distributions and girdles, and were contoured with red to blue colors or high to low grayscale representing

high to low concentrations. Lineations were plotted as hollow or solid points and were contoured similarly to poles to planes.

Thin Section Preparation

In order to identify and analyze minerals, textural relations, and deformation fabrics, oriented samples were prepared for thin section microscope petrography during fall 2015 and fall 2016. Billets were oriented perpendicular to foliation and parallel to lineation in order to show shear sense (Figure 4, Figure 12). Billets were sent to Spectrum Petrographics, Inc. for thin section preparation during fall 2015 and fall 2016. Billets were mounted on borosilicate glass slides, then cut and ground down to a thickness of 30 μm. Thin sections were finished with a borosilicate glass cover slip or were polished using 18, 6, 3, 1, and 0.5 μm diamond grit.

Microscope Petrography

Microscopic analysis of rocks was used to supplement field identification of mineralogy, foliations, and other deformation fabrics. Shear sense indicators (Figure 5) were characterized based on classification from Passchier and Trouw (2005). Analysis was conducted on a petrographic microscope at the Montana State University Structural Geology Research Lab during academic years 2015-2016 and 2016-2017.

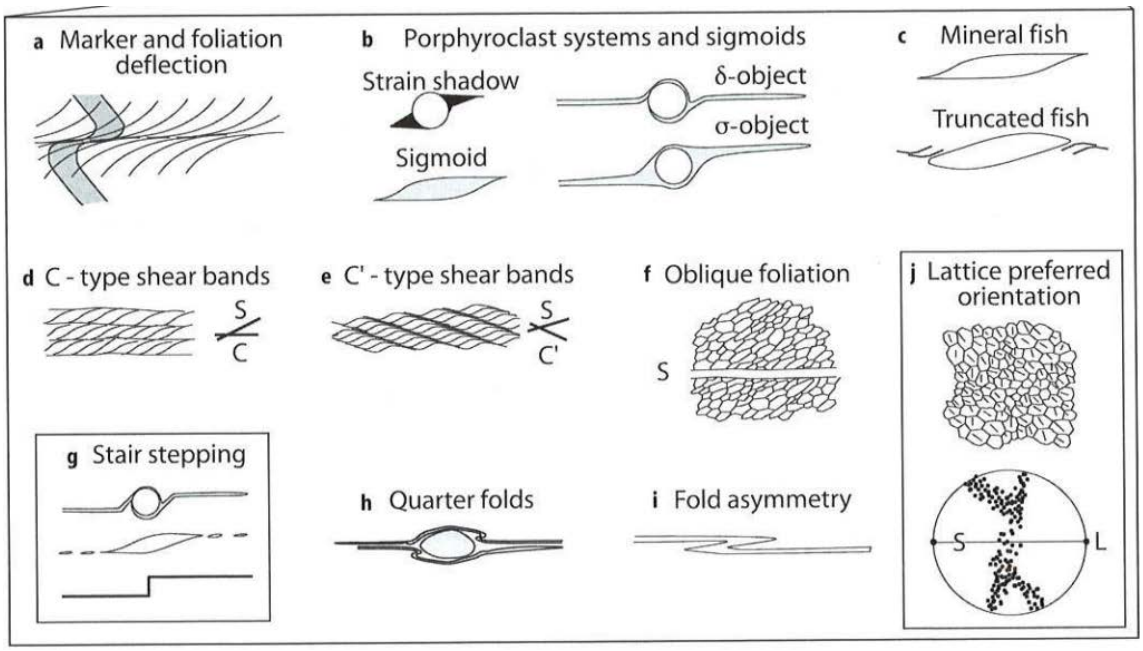

Figure 5. Shear sense indicators. After Passchier and Trouw (2005).

TitaniQ Thermometry

Temperature of metalamprophyre deformation was calculated using the *TitaniQ*, titanium in quartz thermometer from Wark and Watson (2006) using the Microanalytical Laboratory at Concord University in Athens, West Virginia during spring 2017. *TitaniQ* calculates the temperature at which equilibrium is reached for Ti substituting freely for Si in quartz when Ti is available in excess as indicated by the presence of a TiO_2 phase such as rutile (Wark and Watson, 2006). The calculated deformation temperature is a minimum estimate, because deformation temperatures may have been higher than those recorded at equilibrium. Calculations are based on Equation 1 (Wark and Watson, 2006), using weight percent concentrations (ppm) of Ti from electron microprobe analysis.

$$T(^{\circ}\mathrm{C}) = \frac{-3765}{\log\left(X_{Ti}^{qtz}\right) - 5.69} - 273 \qquad (1)$$

Weight percent concentration of Ti was measured using wavelength dispersive spectroscopy (WDS) on an ARL-SEMQ electron microprobe. Analytical uncertainty of the *TitaniQ* thermometer is two sigma (Wark and Watson, 2006). Detection limits of the microprobe were 6 ppm with 68% confidence (one sigma) and 17 ppm with 99% confidence (three sigma). X-ray intensities for Ti were measured simultaneously using 3 WDS spectrometers. One spectrometer contains a pentaerythritol (PET) analyzer crystal and two contain lithium fluoride (LIF) analyzer crystals. Multiple spectrometers were used to simultaneously measure Ti concentrations to obtain *TitaniQ* calculations with higher precision. Mean atomic number (MAN) modeled X-ray backgrounds were also used to enhance precision and lower detection limits (Donovan et al., 2016). The blank correction sample from Donovan et al. (2011) was also used to improve accuracy at low Ti concentrations. Sample points for analysis were chosen at least 50 to 100 µm away from TiO_2 phases, in order to minimize unwanted effects of secondary fluorescence due to Bremsstrahlung radiation (Wark and Watson, 2006). Accelerating voltage was 15 kV, beam current was 100 nA, and analysis time was 400 seconds (7 minutes). Analysis was conducted on polished thin sections that were treated with 250 Å carbon coating, measured by interference coloration on copper (Kerrick et al., 1973).

CHAPTER THREE

ROCK DESCRIPTIONS

Bedrock geology is described based on field observations and laboratory analysis of rocks exposed primarily in the Homestake Reservoir quadrangle, and minor exposures in the northeast corner of the Nast Quadrangle (Figure 1). Lithologic groups are divided into Paleoproterozoic gneiss country rock, Mesoproterozoic igneous rocks intruded into the Paleoproterozoic country rock, and Mesoproterozoic shear zone tectonites deforming Paleoproterozoic country rock as well as Mesoproterozoic igneous rocks. A complete description of map units of the Homestake Reservoir quadrangle is included in Appendix A.

Paleoproterozoic Gneiss

Biotite Gneiss

Biotite gneiss is a gray to brown, foliated, biotite-rich quartzofeldspathic gneiss (Figure 6). Modal mineralogy includes on average 55% quartz, 20% biotite, 10% muscovite, 5% sillimanite, 5% potassium-feldspar, and 5% opaques.

Quartz occurs primarily as anhedral, fine grains with moderately straight grain boundaries and 120° foam structure in leucosomes. Some quartz grains include subgrains that display minor undulose extinction. Biotite occurs as euhedral to subhedral, fine to medium grains that exhibit strong grain shape preferred orientation, defining thin foliations. Biotite is bent in places and exhibits undulose extinction. Muscovite occurs as

euhedral, fine to medium grains that have weak to moderate grain shape preferred orientations and crosscut biotite grains. Muscovite is not deformed. Sillimanite occurs as long, fibrous grains parallel to foliations. Sillimanite fibers are wavy and display undulose extinction. Sillimanite is intergrown with muscovite. Potassium feldspar occurs as subhedral to anhedral, fine grains in leucosomes. Potassium feldspar displays cross-hatch twinning and is slightly perthitic in places. Opaques occur as interstitial, anhedral grains.

Foliations are defined primarily by compositional banding of quartz-rich leucosomes and biotite-rich melanosomes. Grain shape preferred orientations of biotite also contributes strongly to foliations. Felsic leucosomes are on average between 1-10 mm thick, but may be as thick as 1 m. Melanosomes, primarily consisting of aligned biotite selvages, vary from less than 1 mm to 10 cm thick. Foliations are relatively straight in high-strain lenses. Foliations are structurally chaotic and disorganized in low-strain lenses.

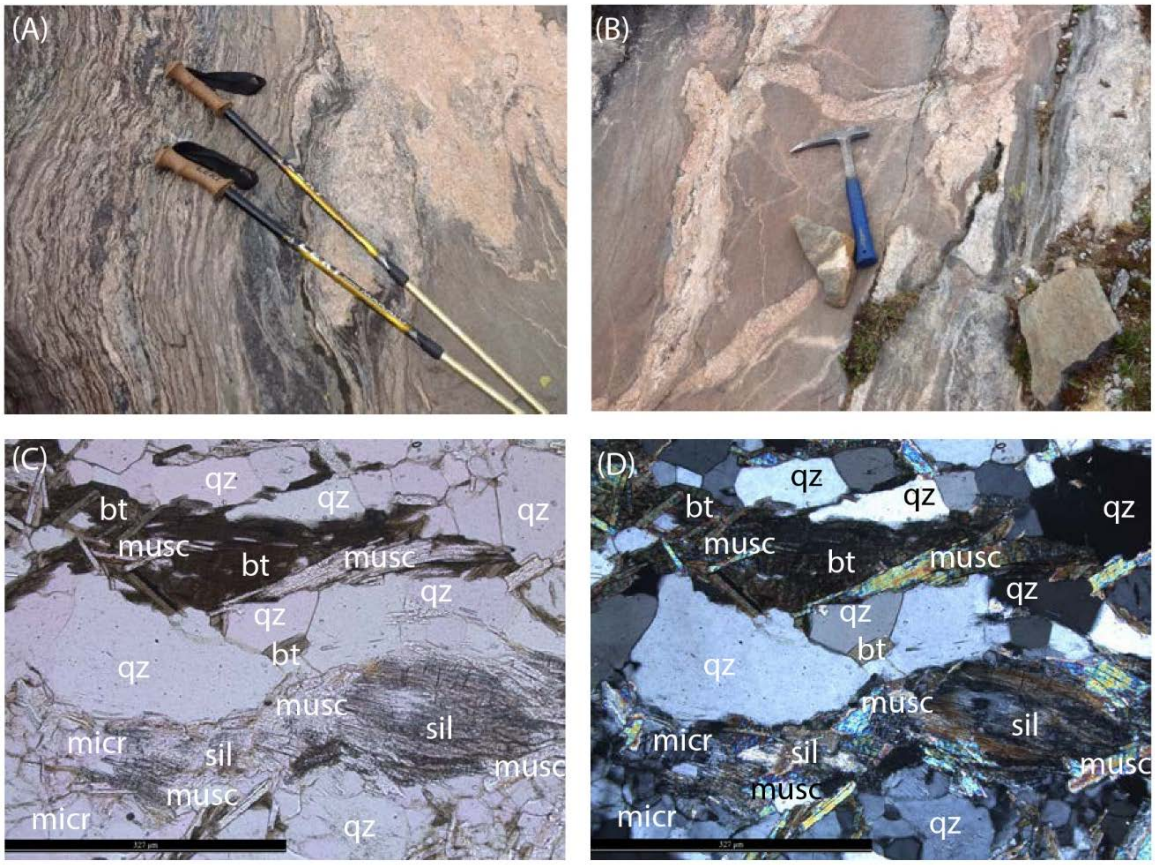

Figure 6. Biotite gneiss. (A,B) Biotite gneiss outcrops with deformed compositional banding and leucosomes near Bench Lakes in northwestern structural domain IV, hiking poles and hammer for scale. Photomicrograph of biotite gneiss showing compositional banding, biotite and muscovite foliations, recrystallized quartz grains, microcline, and sillimanite with 327 µm scale bar, (C) PPL and (D) XPL.

Hornblende Gneiss

Hornblende gneiss is a gray to dark gray, weakly foliated, hornblende and plagioclase-rich gneiss (Figure 7). Modal mineralogy includes on average 60% hornblende, 30% plagioclase, 5% biotite, 5% chlorite, and trace opaques. Minor quartz and microcline may also occur when adjacent to other quartzofeldspathic gneiss.

Hornblende occurs as subhedral to anhedral, medium grains. Few hornblende grains are euhedral with straight boundaries. Hornblende displays weak to moderate grain shape preferred orientation along foliation and moderate granoblastic texture with 120° foam structure. Plagioclase occurs as anhedral, fine grains with moderate granoblastic texture and 120° foam structure. Biotite occurs as euhedral to subhedral, fine grains. Biotite contains moderate grain shape preferred orientations defining weak foliations. Some biotite grains also crosscut foliations. Chlorite occurs as subhedral to anhedral, fine grains replacing biotite and hornblende. Rare opaques occur as anhedral, fine interstitial grains.

Foliations are defined by moderate to strong compositional banding. Weak grain shape preferred orientations also contribute to foliations. Hornblende rich melanosomes vary from 1-100 mm thick. Foliations may be straight in high-strain lenses. Foliations are structurally chaotic and disorganized in low-strain lenses.

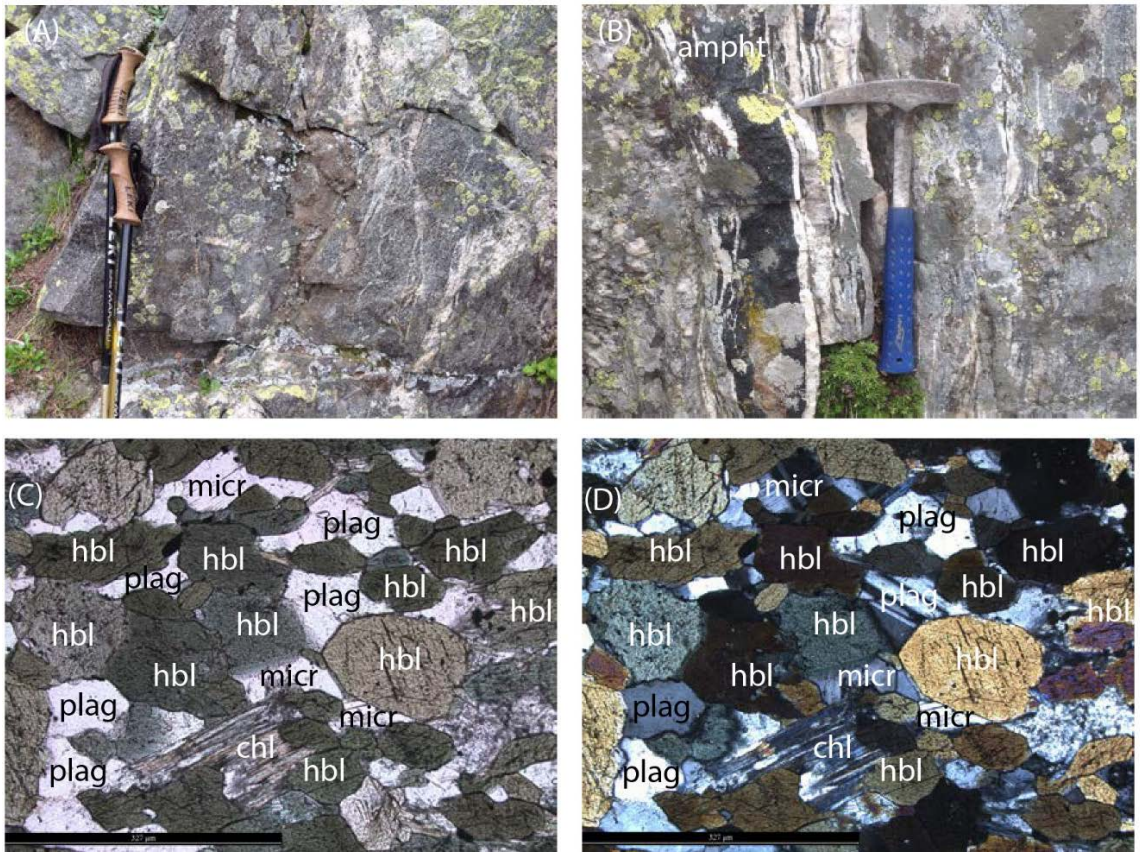

Figure 7. Hornblende gneiss. (A) Hornblende gneiss outcrop looking perpendicular to foliation near East Fork Homestake Creek in structural domain II, hiking poles for scale. (B) Amphibolite (ampht) melanosome, 10 cm wide, and feldspar leucosomes, 1 cm wide, in biotite gneiss, hammer for scale. Photomicrograph of hornblende gneiss showing hornblende, plagioclase, and minor microcline and chlorite in Domain II with 327 µm scale bar, (C) PPL and (D) XPL.

Micaceous Quartzite

Micaceous quartzite varies from a light gray to gray green, nearly pure quartzite (Figure 8), to a moderately gray, biotite-bearing, quartzofeldspathic gneiss. Most occurrences have average modal mineralogy of 45% quartz, 30% potassium feldspar, 20% biotite, and 5% sericite. Rare occurrences have modal mineralogy of nearly 100% quartz.

Quartz occurs as anhedral, fine grains. Some quartz contains moderately straight grain boundaries and 120° foam structure. Other quartz grains contain serrated grain boundaries with subgrain development and undulose extinction. Potassium feldspar occurs primarily as anhedral to subhedral, fine grains. Potassium feldspar displays strong cross-hatch twinning, moderate perthitic texture, and subgrain development. Rare, coarse pods of potassium feldspar occur with sericite alteration and strong perthitic textures. Biotite occurs as euhedral to subhedral, fine to medium grains.

Weak foliations are defined by moderate grain shape preferred orientation of biotite. Biotite foliations, when present, are less than 1 mm thick. Relatively pure quartzite lenses may be up to 10 m thick.

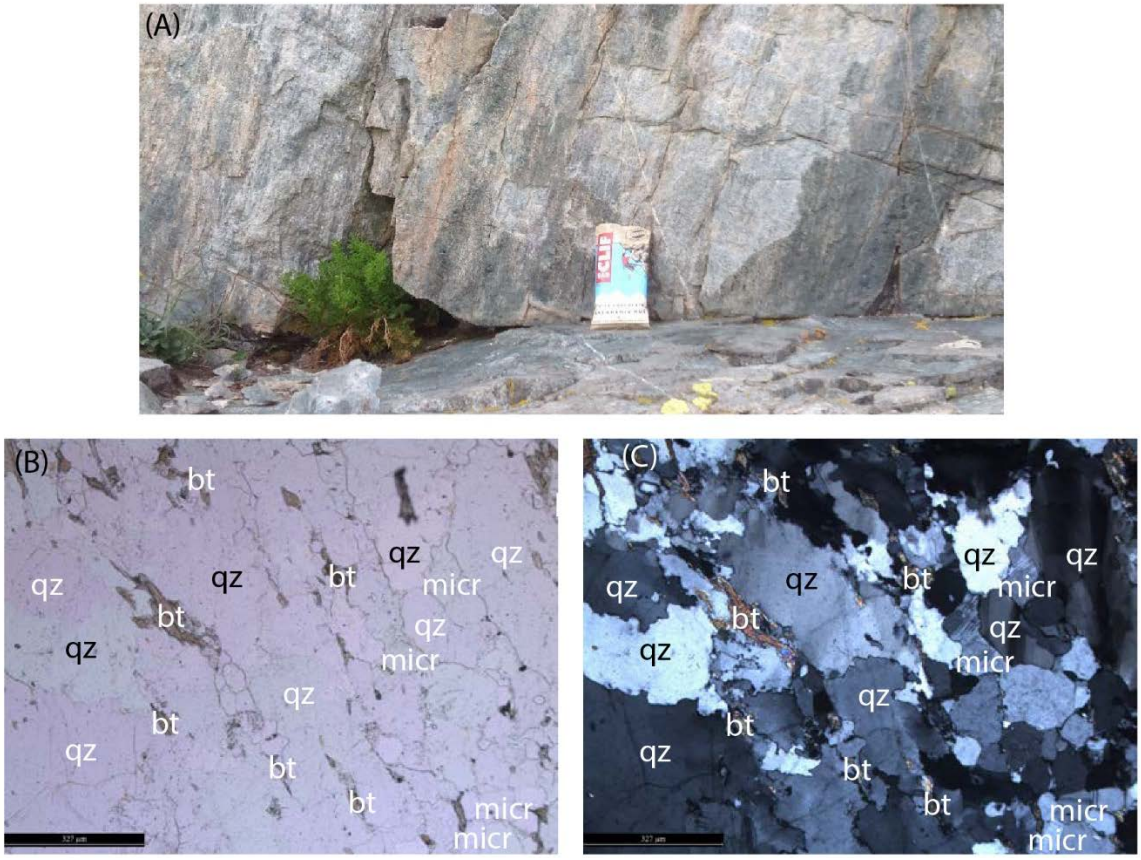

Figure 8. Micaceous quartzite. (A) Micaceous quartzite outcrop near East Fork Homestake Creek in southern structural domain II, candy bar for scale. Photomicrograph of Micaceous quartzite showing undulose extinction in quartz subgrains, irregular quartz grain boundaries due to grain boundary migration recrystallization, and minor biotite and microcline with 327 µm scale bar, (B) PPL and (C) XPL.

Calc-Silicate Gneiss

Calc-silicate gneiss varies from a light to medium gray, weakly foliated calc-silicate gneiss to a nearly pure marble (Figure 9). Modal mineralogy on average includes 45% clinopyroxene, 40% calcite, and 15% microcline.

Clinopyroxene occurs as euhedral to subhedral, fine to coarse grains. Coarse clinopyroxene porphyroblasts often have straight grain boundaries, and are overprinted by fine grained microcline and calcite with irregular grain boundaries. Calcite occurs as euhedral to subhedral, fine to medium grains with moderate 120° foam structure. Calcite also occurs as fine grained inclusions in clinopyroxene with irregular grain boundaries. Thin seams of calcite also occurs between other grains. Calcite displays strong twinning. Microcline occurs as subhedral to anhedral, medium grains with granoblastic textures in places. Microcline also occurs as anhedral, fine grained inclusions in clinopyroxene. Microcline displays weak to moderate tartan twinning.

Foliations are rarely seen in outcrop-scale or thin section scale, unless mixed with other hornblende gneiss or quartzofeldspathic gneiss. Calc-silicate gneiss displays hackly weathering in outcrop.

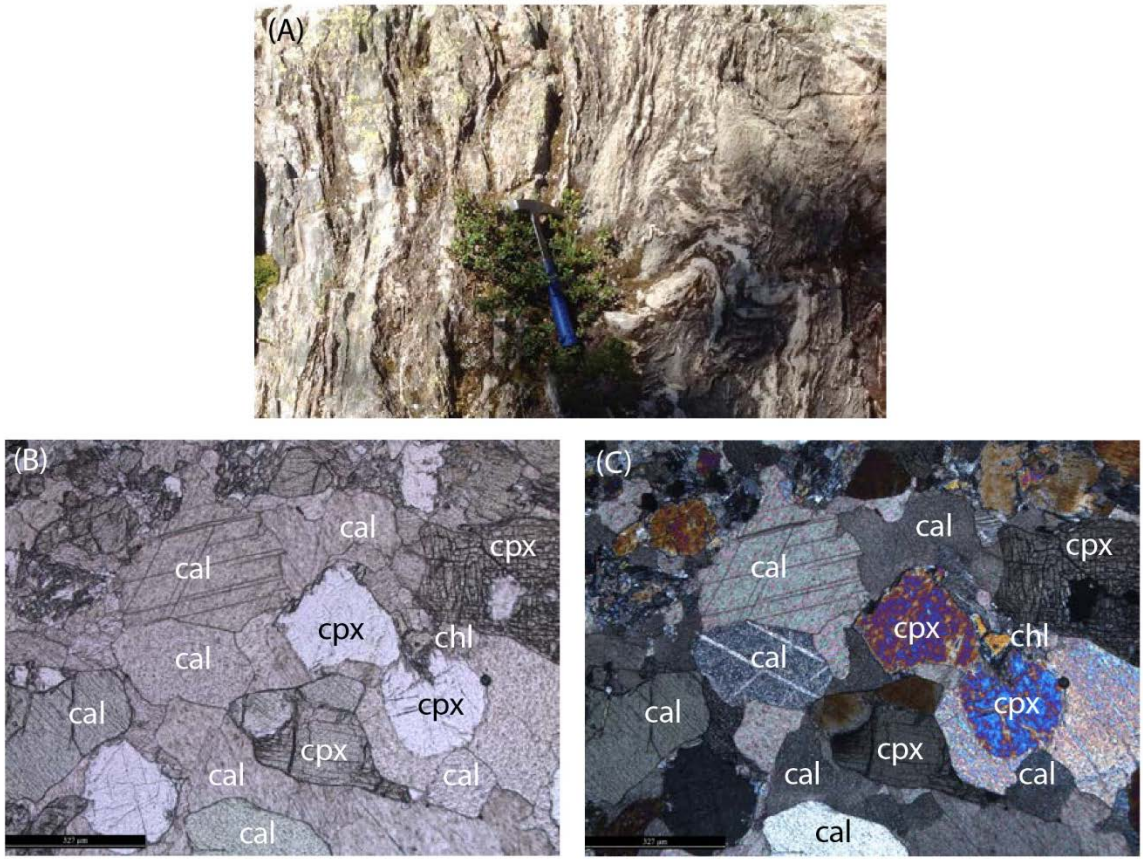

Figure 9. Calc-silicate gneiss. (A) Calc-silicate gneiss showing deformed foliations and hackly weathering, rock hammer for scale. Photomicrograph of calc-silicate gneiss showing twinned calcite plus clinopyroxene and chlorite in structural domain II with 327 µm scale bar, (B) PPL and (C) XPL.

Mesoproterozoic Igneous Rocks

Metalamprophyre

Metalamprophyres occur as dark gray, brown, to gray green, mafic, ultrapotassic, porphyritic dikes (Figure 10). Matrix modal mineralogy includes on average 35% biotite, 30% potassium feldspar, 20% quartz, and 15% hornblende. Porphyroblast modal mineralogy includes on average 60% hornblende and 40% biotite. Whole rock XRF geochemical analysis by Barbery et al. (2013) and Fell et al. (2004) suggest that these metalamprophyres were emplaced as calc-alkaline lamprophyres to lamproitic lamprophyres (Figure 11), based on classification by (Rock, 1987).

The following minerals occur in the matrix. Quartz occurs as anhedral, fine grains. Quartz grains show varied textures from moderate 120° foam structure in places to irregular grains with subgrain development and undulose extinction. Potassium feldspar occurs as anhedral, fine grains. Potassium feldspar displays perthitic texture in places and moderate undulose extinction. Biotite occurs as euhedral to subhedral, fine grains. Biotite is bent in places with undulose extinction. Biotite contains moderate grain shape preferred orientation contributing to foliations.

The following minerals occur in the porphyroblasts. Hornblende occurs as subhedral to anhedral, fine to medium grains with decussate textures. Hornblende is concentrated in the center of porphyroblasts. Biotite in porphyroblasts occur as euhedral to subhedral, fine grains. Biotite in the center of porphyroblasts is randomly oriented and rare. Biotite is more highly concentrated along the edges of porphyroblasts and contains a moderate grain shape preferred orientation, defining foliations.

Metalamprophyres display strong foliations near their margins, and moderate foliations near the center of the dikes. Foliations are defined by compositional banding of feldspar and quartz in felsic lenses, and biotite and hornblende in mafic lenses. Strong grain shape preferred orientations in biotite, and moderate grain shape preferred orientations in hornblende also contribute to foliations. Foliations are less than 1 mm apart near the dike margins. Weak foliations are as much as 1 cm apart near the dike centers. Foliations rotate into parallelism with dike contacts.

Lineations, when present, are defined by elongated porphyroblasts of hornblende and biotite. Porphyroblasts are mostly undeformed near dike centers, and are strongly elongated near dike margins (Figure 12). Undeformed aggregate porphyroblasts near dike centers sometimes display pseudomorphic shapes of hexagonal prismatic end sections (Figure 10).

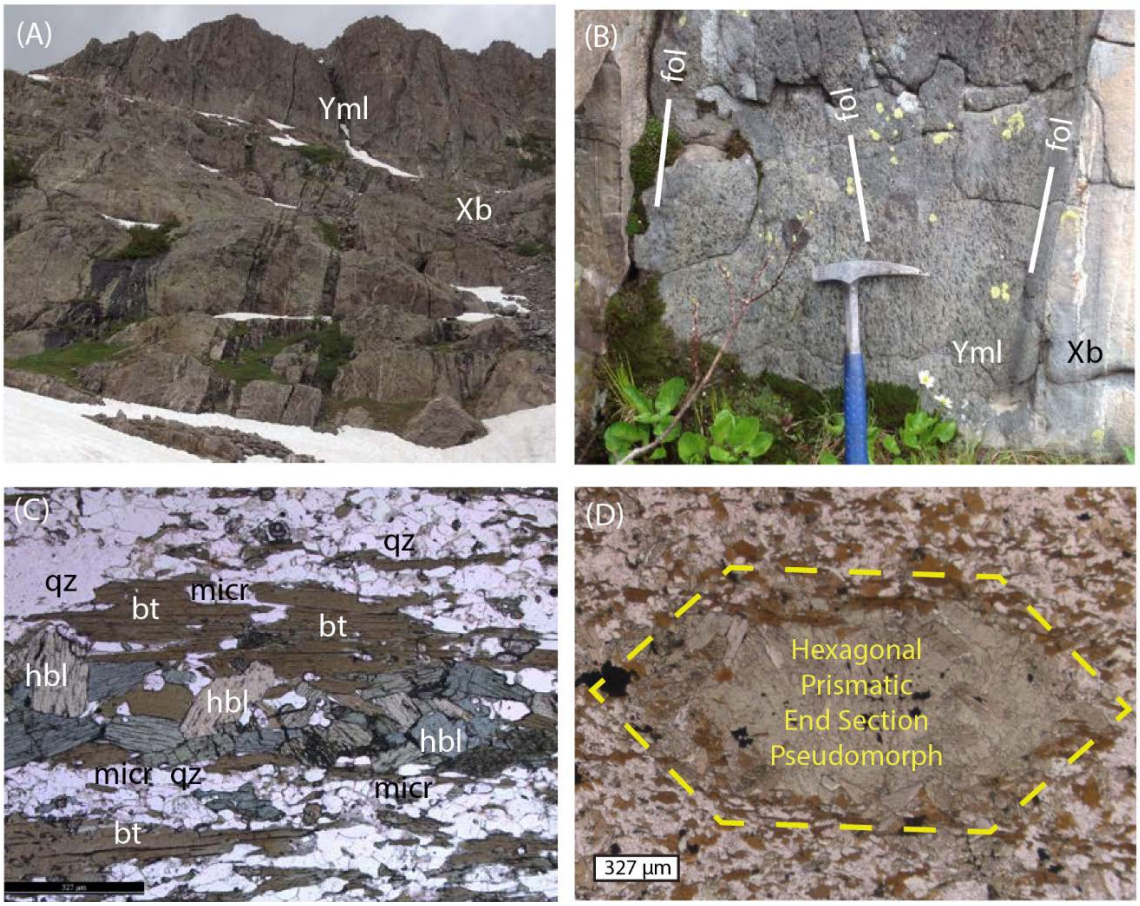

Figure 10. Metalamprophyre dikes. (A) Metalamprophyre dikes (Yml), 1-4 m wide, weathering faster than the biotite gneiss host rock (Xb), looking west near Lake Esther in Domain II. (B) Metalamprophyre dike with varied foliation (fol) orientations, looking west near Lake Esther in Domain II, hammer for scale. (C) Photomicrograph of metalamprophyre showing elongated mineral aggregates of biotite and hornblende in quartz, microcline, and minor plagioclase matrix with 327 µm scale bar in PPL. (D) Photomicrograph showing an undeformed hornblende and biotite porphyroblast as a hexagonal prismatic end section pseudomorph with a 327 µm scale bar in PPL.

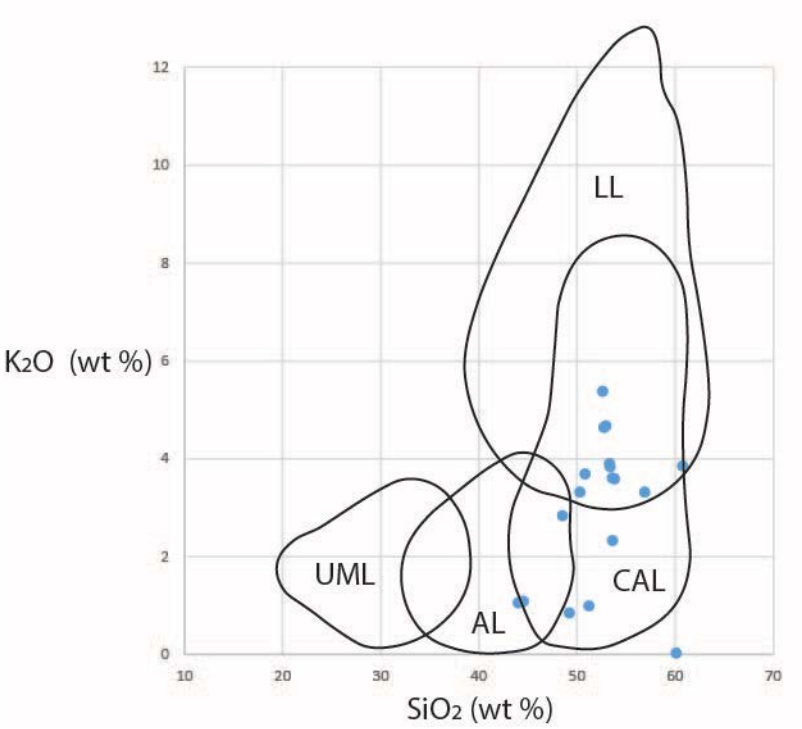

Figure 11. Whole Rock XRF classification of metalamprophyres. SiO2 vs. K2O wt % (blue dots) classification of ultramafic (UML), alkaline (AL), calc-alkaline (CAL), and lamproitic (LL) lamprophyres (Rock, 1987), using data from Barbery et al. (2013) and Fell et al. (2004).

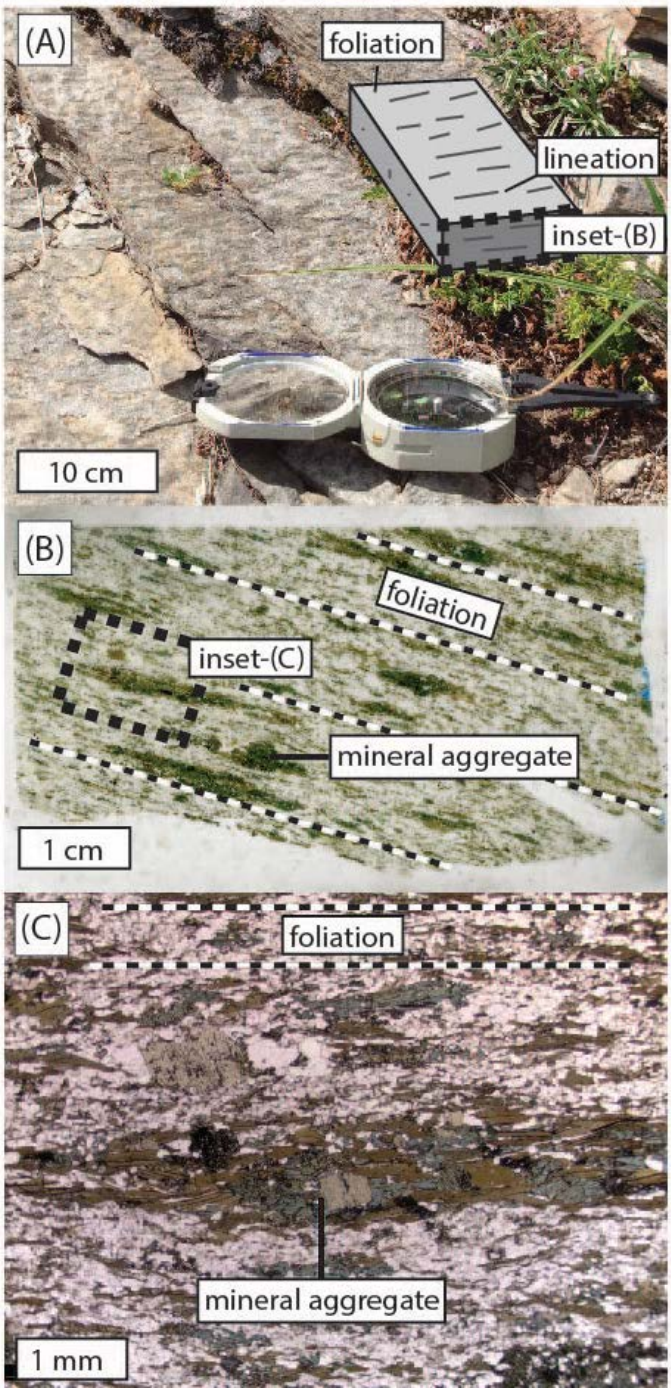

Figure 12. Foliations and mineral aggregate lineations in metalamprophyres. (A) Oblique view of outcrop looking down onto foliation planes that contain lineations. Inset shows orientation of thin section shown in (B) cut perpendicular to foliation and parallel to lineation. (B) Thin section in PPL showing compositional banding foliations, grain preferred orientation foliations, mineral aggregates. Inset shows the location of (C). (C) PPL thin section of hornblende-rich elongated mineral aggregate and foliations.

St. Kevin Granite

The St. Kevin granite is a gray, tan, to pink, medium to coarse-grained, moderately foliated, biotite-muscovite granite to granodiorite (Figure 13). Modal mineralogy on average is 40% quartz, 30% potassium feldspar, 15% muscovite, 10% biotite, and 5% plagioclase. Plagioclase modal percentage increases in other locations throughout the batholith, although this is not described in detail.

Quartz occurs as anhedral, medium grains. Quartz displays bulging grain boundaries, subgrains, and undulose extinction in places. Potassium feldspar occurs as subhedral to euhedral, medium to very coarse grains. Potassium feldspar commonly contains granoblastic textures with 120° foam structures. Potassium feldspar displays strong cross-hatch twinning and moderate carlsbad twinning in places. Potassium feldspar displays perthitic and myrmekite textures in places, and is also commonly altered by sericite. Muscovite occurs as primary, euhedral to anhedral, medium grains. Muscovite is bent and displays undulose extinction in places. Biotite occurs as anhedral to subhedral, fine to medium grains. Secondary biotite may be found in fractures. Plagioclase occurs as subhedral to anhedral, medium to coarse grains and is often highly altered by sericite.

Rare foliations are defined by biotite-rich selvages, and aligned euhedral microcline. Biotite rich selvages are 1-10 cm apart, and are approximately parallel to adjacent Paleoproterozoic gneiss foliations. Euhedral microcline are 1-3 cm long and display strong grain shape preferred orientation, approximately parallel to adjacent Paleoproterozoic gneiss foliations.

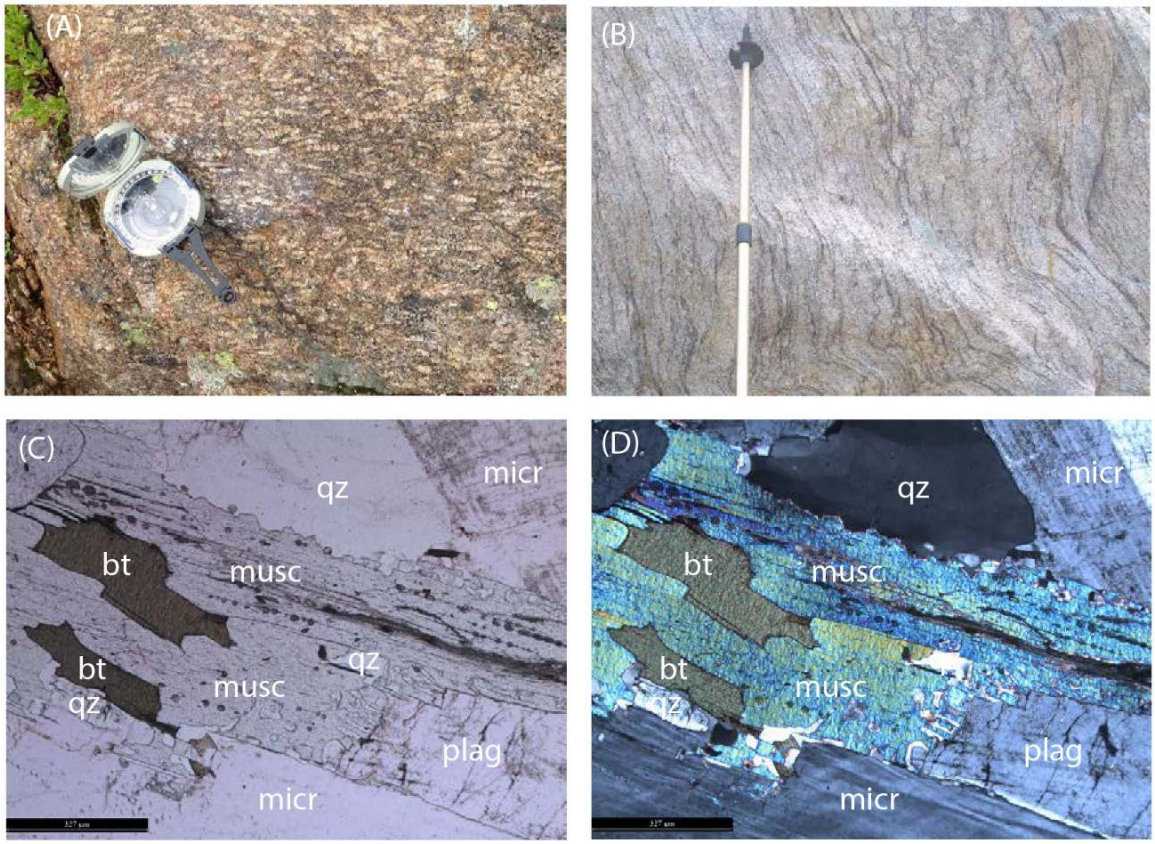

Figure 13. St. Kevin granite. (A) Euhedral microcline mineral foliations near Galena Lake, compass for scale. (B) Biotite-rich foliations looking west on ridge between Homestake Reservoir and East Fork Homestake Creek, hiking pole for scale. Photomicrographs of granite in the St. Kevin batholith containing biotite, muscovite, microcline, plagioclase, and quartz with 327 µm scale bar, (C) PPL and (D) XPL.

Mesoproterozoic Shear Zone Tectonites

Mylonite Shear Tectonites

Mylonitic shear zones contain tectonites defined by fine grained matrices, elongated minerals, and ductilely sheared porphyroclasts (Figure 14). If fully recrystallized, fine grained matrices may contain grains with granoblastic textures and 120° foam structures. Fine grained matrices may also contain deformed grains with bulging grain boundaries, subgrains with undulose extinction, or serrated grain boundaries. Elongated minerals may be single grains stretched out as ribbons, or may be aggregates of grains. Ductilely sheared grains may include recrystallized grain tails in σ-clasts or δ-clasts, or a number of other shear sense indicators (Figure 5) outlined by Passchier and Trouw (2005).

Mylonite foliations are defined by strong compositional banding and grain shape preferred orientation of biotite. Foliations are on average 1-2 mm thick, and are very straight. Very fine grains give mylonite a cherty texture in outcrop.

Mylonitic shear tectonites occur in all Proterozoic gneiss and Mesoproterozoic igneous rocks mentioned previously. Mylonite shear tectonites may be concentrated in shear zones such as the HSZ and SLSZ, along the margins of metalamprophyre dikes, or in other country rocks,

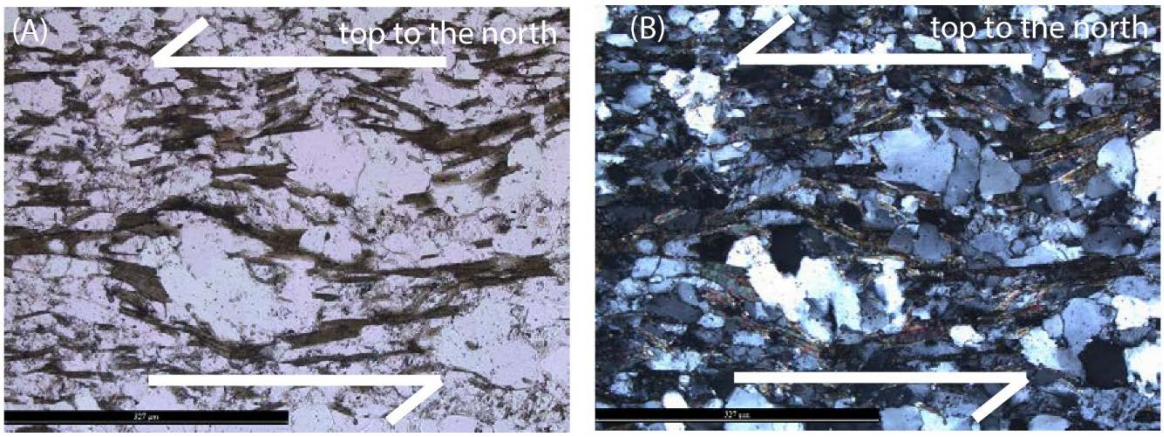

Figure 14. Mylonitic fabric. Top to the north sense of shear of quartz sigma porphyroclasts, undulose extinction across quartz subgrains, and deflected biotite foliations in the Slide Lake Shear Zone with 327 μm scale bar, (A) PPL, (B) XPL.

Pseudotachylyte Shear Tectonites

Pseudotachylyte shear zones contain tectonites defined by dark gray to black, amorphous fault rock with or without brecciated clasts of wall rock (Figure 15). The matrix modal mineralogy is defined by the deformed host rock, although is not easily identifiable in outcrop-scale or in thin section. The matrix may be subsequently recrystallized, although this is not described in detail. Characteristic orientations include planar pseudotachylyte along fault surface, as well as injection veins at an oblique angle to the fault surface.

Pseudotachylyte shear tectonites occur in all Proterozoic gneiss and Mesoproterozoic igneous rocks mentioned previously. Pseudotachylyte shear tectonites may be concentrated in shear zones such as the HSZ and SLSZ, in metalamprophyre dikes, or in other localized occurrences throughout the field area.

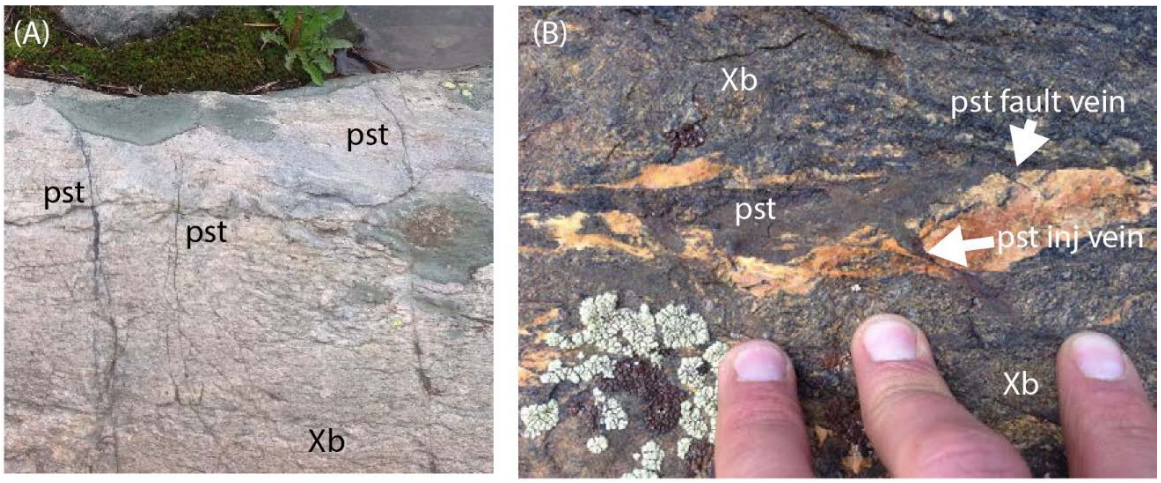

Figure 15. Pseudotachylyte. (A) Recrystallized pseudotachylite (pst) fault veins in biotite gneiss (Xb) host along the East Fork Homestake Creek, width of view is 50 cm. (B) Recrystallized pseudotachylyte fault vein and oblique injection vein in biotite gneiss host in the SLSZ just below Homestake Peak.

CHAPTER FOUR

STRUCTURAL DOMAINS

The research area is subdivided into structural domains I through VI, characterized by orientations of metamorphic foliations, deformation fabrics, rock types, and rock ages (Figure 16). The map extent of structural domain analysis includes the Homestake Reservoir, Mount of the Holy Cross, Pando, and Leadville North USGS 7.5' quadrangles using data from this research and previous work (Allen, 2005; Allen and Shaw, 2013; Lee et al., 2012; Shaw and Allen, 2007; Shaw et al., 2005; Shaw et al., 2001; Tweto, 1974). Structural domain boundaries in Figure 16 closely follow generalized geologic features in Figure 1.

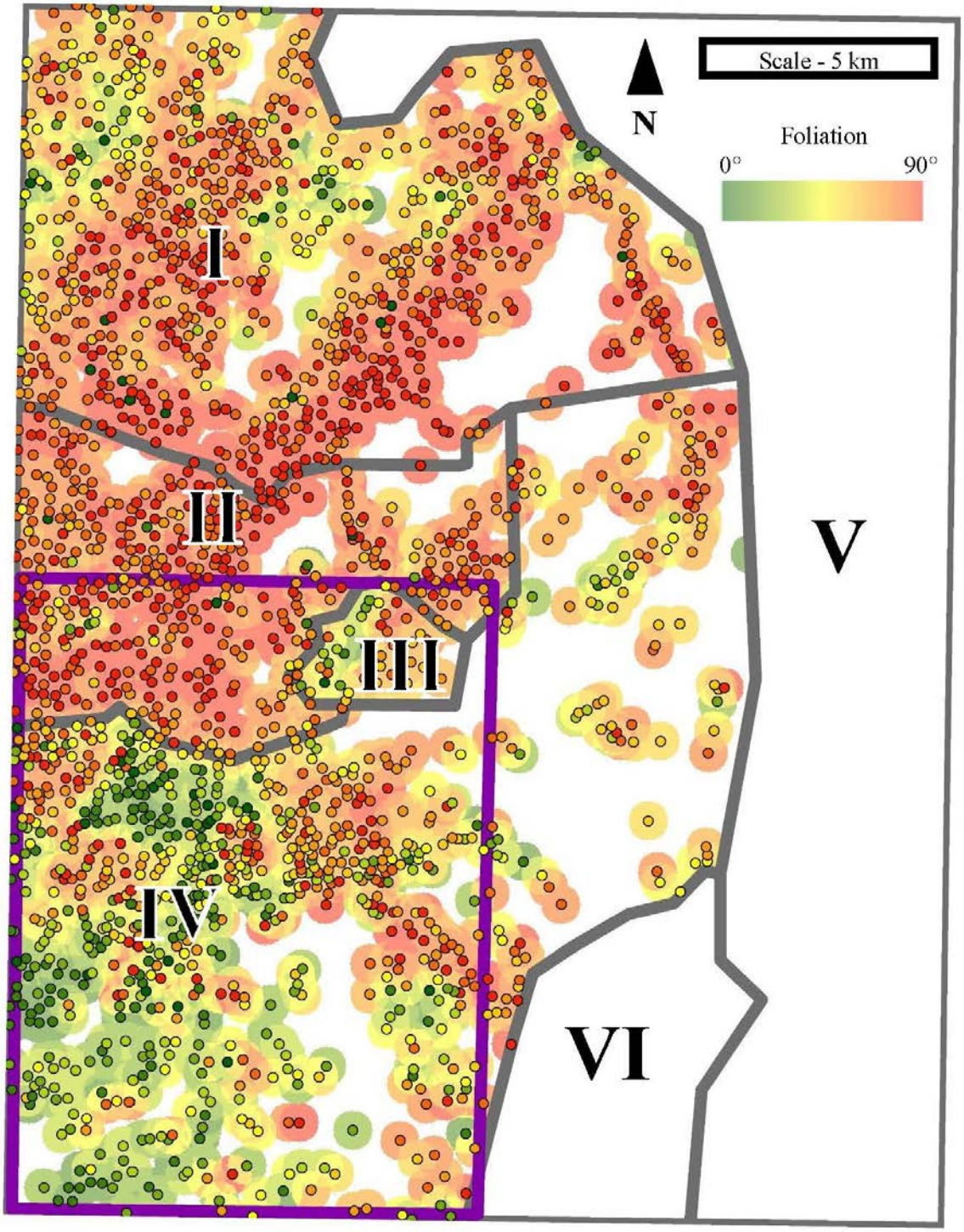

Figure 16. Structural domain map and dip of metamorphic foliations. Domains are marked by roman numerals and bounded by thick gray polygons. Small red circles represent near-vertical dip. Small green circles represent near-horizontal dip. Mount of the Holy Cross 15' quadrangle is outlined in gray rectangle (Tweto, 1974). Homestake Reservoir 7.5' quadrangle is outlined in purple rectangle.

Structural Domain I — Homestake Shear Zone

Structural domain I is characterized by northeast striking, steeply dipping axial planar foliations in Proterozoic gneiss, locally overprinted by the HSZ (Figure 16, Figure 17). Structural domain I is located in the Mount of the Holy Cross quadrangle (Tweto, 1974), north of the Homestake Reservoir mapping area. Mylonite, ultramylonite, and pseudotachylyte in the HSZ on average strike northeast and dip subvertically to the southeast, with lineations plunging steeply to the southeast (Allen, 2005; Shaw et al., 2001).

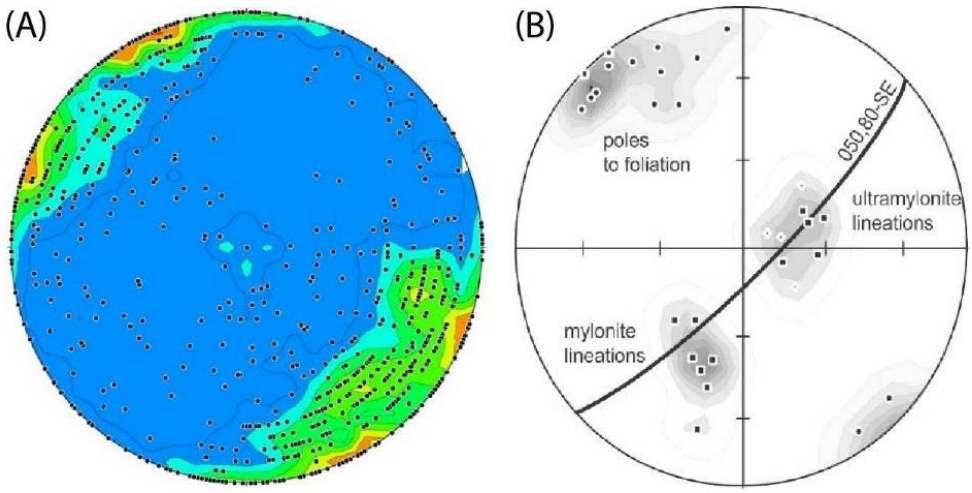

Figure 17. Structural domain I. (A) Contoured poles to planes of metamorphic foliations in structural domain I. (B) Foliations and lineations of HSZ mylonite and ultramylonite near the Hornsilver Campground of the White River National Forest in structural domain I. After Shaw and Allen (2007).

Structural Domain II — Hornblende Gneiss, Calc-Silicate Gneiss, and Metalamprophyres

Structural domain II is characterized by east striking, steeply dipping axial planar foliations in Paleoproterozoic gneiss, pervasively intruded by metalamprophyre dikes (Figure 16, Figure 18). Structural domain II is located in the northwest corner of the Homestake Reservoir quadrangle, and overlaps into the southwest corner of the Mount of the Holy Cross quadrangle. A distinct, east-west trending, 1-2 km thick swath of hornblende gneiss and calc-silicate gneiss is located along the southern domain boundary. The highest concentrations of metalamprophyre dikes are located in structural domain II.

Axial planar foliations demonstrate a distinct change in orientation from northeast striking in structural domain I to east striking in structural domain II. Characteristic steep foliations of structural domain II are represented in the cross section (Plate I) from point A in the northwest traversing southward to halfway between the first and second bend in section (BIS).

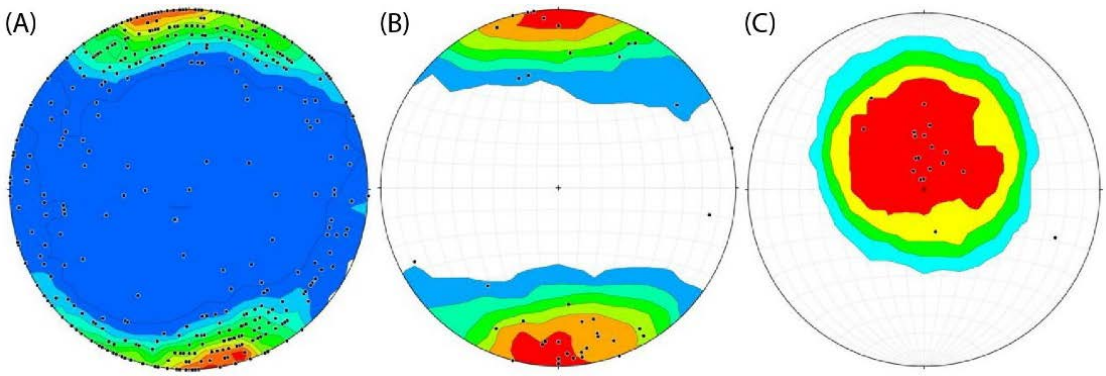

Figure 18. Structural domain II. (A) Contoured poles to planes of metamorphic foliations in structural domain II. (B) Contoured poles to planes of metalamprophyre orientations in structural domain II. (C) Contoured lineations in deformed metalamprophyres in structural domain II.

Structural Domain III — Slide Lake Shear Zone

Structural domain III is characterized by northeast to east striking, subhorizontal to moderately dipping axial planar foliations in Paleoproterozoic gneiss, overprinted in places by SLSZ deformation (Figure 16, Figure 19) (Lee et al., 2012). Structural domain III is located in the northeast portion of the Homestake Reservoir quadrangle and continues slightly north into the Mount of the Holy Cross Quadrangle. It is bound to the west by northeast and southeast trending ridges containing mylonite and pseudotachylyte of the SLSZ. Mylonite, ultramylonite, pseudotachylyte, and recrystallized pseudotachylyte in the SLSZ overprints moderately to shallowly dipping axial planar foliations in Paleoproterozoic gneiss (Allen and Shaw, 2013; Lee et al., 2012; Tweto, 1974).

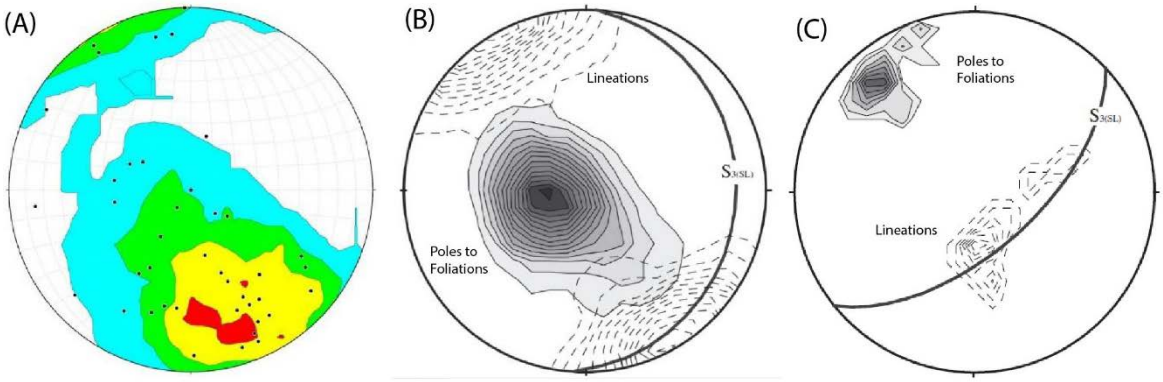

Figure 19. Structural domain III. (A) Contoured poles to planes of metamorphic foliations in structural domain III. (B) Foliations and lineations of SLSZ mylonite and ultramylonite along the Homestake Ridge segment in structural domain III. (C) Foliations and lineations of SLSZ mylonite and ultramylonite along the Bennet Ridge segment in Domain III. After Lee et al. (2012).

Structural Domain IV — St. Kevin Batholith

Structural domain IV is characterized by shallow and subhorizontal axial planar foliations in Paleoproterozoic gneiss, overprinted by locally foliated granite to granodiorite of the St. Kevin batholith (Figure 16, Figure 20). Structural domain IV is located in the southern half of the Homestake Reservoir quadrangle.

A distinct shift in foliation orientations occurs from steep foliations in structural domain II towards shallow and subhorizontal foliations in Domain IV. This characteristic shallowing of foliations is evident in the cross section (Plate I) from halfway between the first and second bend in section (BIS) traversing south and eastward to the end of the cross section at point A'.

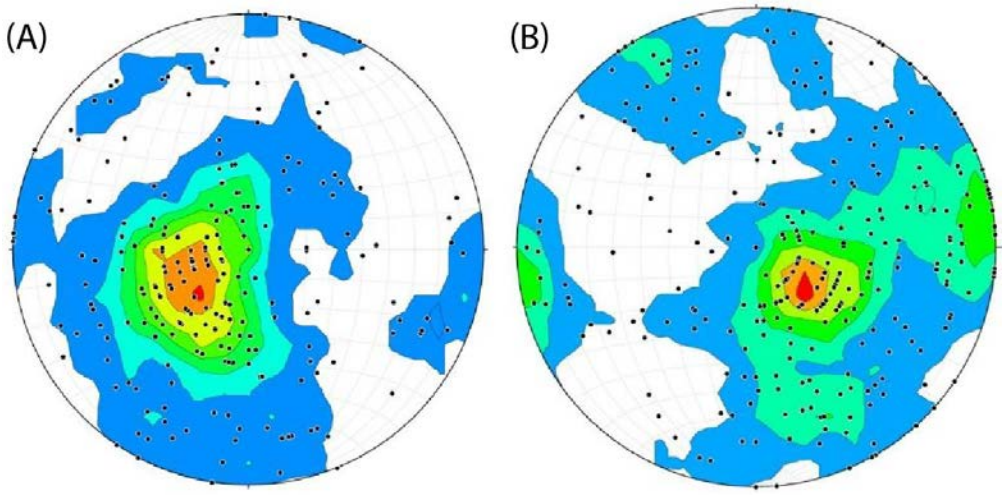

Figure 20. Structural domain IV. (A) Contoured poles to planes of metamorphic foliations in structural domain IV. (B) Contoured poles to planes of foliations in St. Kevin granite and other mixed lithologies in structural domain IV.

Structural Domain V — Paleozoic Sedimentary Cover

Structural domain V is characterized by gently east-dipping Paleozoic bedrock (Figure 16). This is exposed northeast and east of the Homestake Reservoir quadrangle, in the Pando and Leadville North quadrangles.

Structural Domain VI — Upper Arkansas Basin

Structural domain VI is characterized by the Arkansas River Valley and the near northernmost extent of the Rio Grande Rift (Figure 16) (Chapin and Cather, 1994). Little bedrock is exposed here, but the western and eastern flanks of the Rift basin show extensional faults accommodating subsidence of the graben (Tweto, 1979).

Summary

Structural domain analysis identifies distinct shallowing of foliations from north to south across the quadrangle (Plate I). Structural domains I through IV primarily include Proterozoic igneous and metamorphic rocks, with minor Phanerozoic igneous rocks. Steep axial planar foliations of Paleoproterozoic gneiss in structural domains I and II are approximately parallel to orientations of metalamprophyres and the HSZ (Allen et al., 2002; Shaw et al., 2001). A major splay of the SLSZ marks the boundary between steep axial planar foliations in hornblende gneiss and calc-silicate gneiss to the west in structural domain II and more shallow axial planar foliations in biotite-rich quartzofeldspathic gneiss to the east in structural domain III (Lee et al., 2012). Characteristic shallow foliations in structural domain IV are shared by Paleoproterozoic

gneiss, as well as localized foliations in the St. Kevin granite to granodiorite. Structural domains V and VI are not included in mapping of the Homestake Reservoir quadrangle, nor are they a major part of this Proterozoic research. Structural domains I through IV are presumed to continue into the subsurface below basin fill in structural domain V and Paleozoic sediments in structural domain VI based on field relations and previous mapping by Tweto (1974) using subsurface mining data.

CHAPTER FIVE

KEY FIELD RELATIONS

Key field relations are based on location, orientation, and age of various rocks, contacts, and deformation fabrics throughout the research area. These are classified by field observations, supported by laboratory-based microstructural analysis, and supplemented by previous literature. Field relations provide the evidence for kinematic links between country rock, dikes, batholiths, and shear zones, and the framework from which structural domains (Figure 16) in the previous chapter are characterized.

Paleoproterozoic Gneiss

Location

Paleoproterozoic gneiss encompasses all major basement country rock located throughout the field area in the Homestake Reservoir quadrangle, as well as in the adjacent Nast, Mount Jackson, and Mount of the Holy Cross quadrangles (Figure 1). Paleoproterozoic gneiss is intruded by igneous rocks, deformed by shear zones, covered by Paleozoic strata, and obscured by more recent sediments. A localized concentration of Paleoproterozoic hornblende gneiss and other calc-silicate gneiss occurs in a unique, 1-2 km wide, east-west trending band across the northern half of the Homestake Reservoir quadrangle (Figure 1).

Orientation

Orientations of axial planar foliations in Paleoproterozoic gneiss are classified into structural domains I-IV (Figure 16) in order to characterize the structural framework of the Homestake Reservoir quadrangle. The shallow structural domains III and IV are characterized by subhorizontal and shallow dipping axial planar foliations of recumbent, nappe-style folds concentrated in the southern half and northeastern corner of the Homestake Reservoir quadrangle. The steep structural domains I and II are characterized by average northeast to east striking, subvertical axial planar foliations of upright, isoclinal folds concentrated in the northern half of the Homestake Reservoir quadrangle.

Age

Relative ages of deformation in Paleoproterozoic gneiss are characterized in previous field work by Tweto (1974) and Shaw (2001), and absolute ages are characterized by previous analytical work by Shaw et al. (2001). Folds and axial planar foliations are attributed to the accretion and deformation of the Yavapai Terrane ca. 1.7 Ga (Figure 2) (Hoffman, 1988; Karlstrom and Bowring, 1988; Whitmeyer and Karlstrom, 2007). Structural analysis by (Shaw, 2001) identifies recumbent, nappe style folds, characteristic of structural domains III and IV, transposed into upright, isoclinal folds, characteristic of structural domains I and II (Figure 30). Electron microprobe U-Th-Pb dating of monazite crystallization associated with metamorphic fabric growth suggests that these deformation events occurred between 1710-1630 Ma (Shaw et al., 2001).

Mesoproterozoic Metalamprophyres

Location

Metalamprophyres occur throughout the field area, with the highest concentrations in the steep structural domain II near the east-west trending band of hornblende gneiss and calc-silicate gneiss in the northern Homestake Reservoir quadrangle (Figure 1). Metalamprophyres intrude all subdivisions of the Paleoproterozoic gneiss.

Orientation

Metalamprophyre dikes occur in various orientations throughout the research area, and are clustered into three main groups (Figure 21A). The first group of dikes are east striking and subvertically dipping. The second group of dikes are approximately east striking and moderately to shallowly south dipping. The third group of dikes are approximately west to north striking, and moderately to shallowly north to east dipping. In map scale, metalamprophyre dikes are oriented parallel to preexisting axial planar foliations in Paleoproterozoic gneiss, although dikes truncate preexisting foliations in outcrop scale.

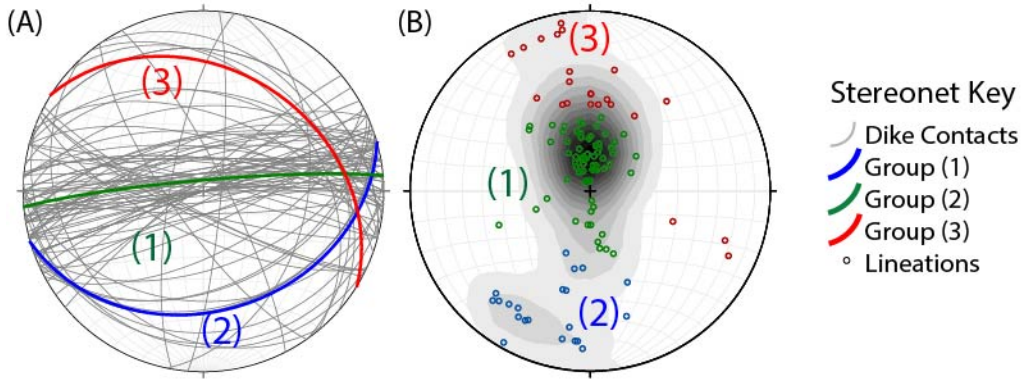

Figure 21. Metalamprophyre dike contacts and lineations. (A) Dike contact orientations and groups. (B) Dike lineations colored by group and contoured by concentration.

Mineral aggregate lineations in dikes also occur in various orientations, clustered into three main groups (Figure 21B). The first group of lineations are on average steeply plunging to the north. The second group of lineations are on average shallowly plunging to the southwest. The third group of lineations are shallowly plunging to the north to northeast. Weak metamorphic lineations in the center of metalamprophyre dikes have varied orientations, independent of dike contact orientations. Strong lineations near dike margins progressively rotate into near parallel orientations with the dike contacts (Figure 22).

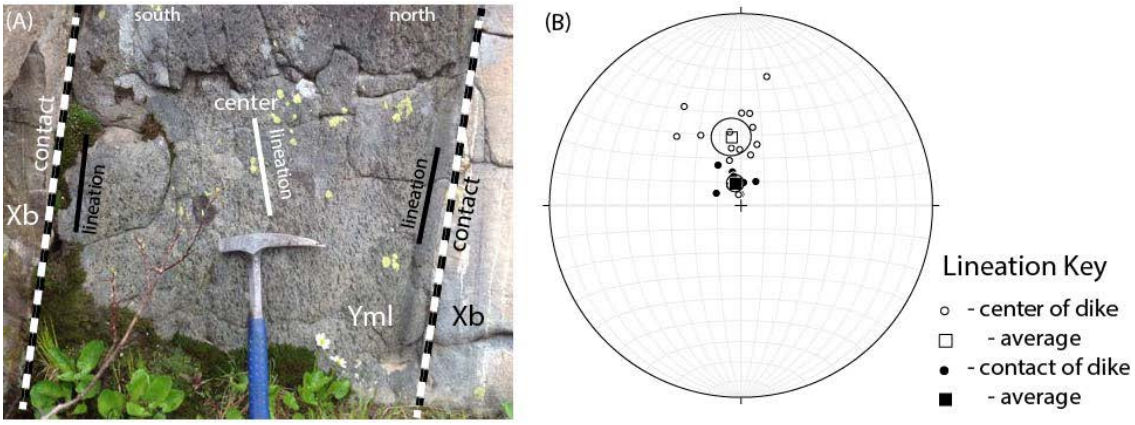

Figure 22. Multiple lineations in metalamprophyre dikes. (A) Metalamprophyre dike with multiple lineation orientations, hosted by biotite gneiss. View looking west at a plane oriented perpendicular to foliations and dike contacts and parallel to lineations, hammer for scale. (B) Metalamprophyre lineations near dike contacts plunging steeply to the north, and lineations near dike centers plunging more shallowly to the north.

Age

Metalamprophyre dikes sharply truncate preexisting axial planar foliations in Paleoproterozoic gneiss. Linear metalamprophyre dikes are discontinuous and truncated abruptly at the contacts with the St. Kevin batholith (Figure 23). Metalamprophyre dikes are crosscut by thin felsic intrusions with consistent composition to the St. Kevin batholith (Figure 23B). Metalamprophyre dikes within the St. Kevin batholith often contain thin slivers of original Paleoproterozoic host rock contacts in between the dike and granite (Figure 23C). Contacts of metalamprophyre dikes are offset while surrounded by the St. Kevin batholith (Figure 23B,D).

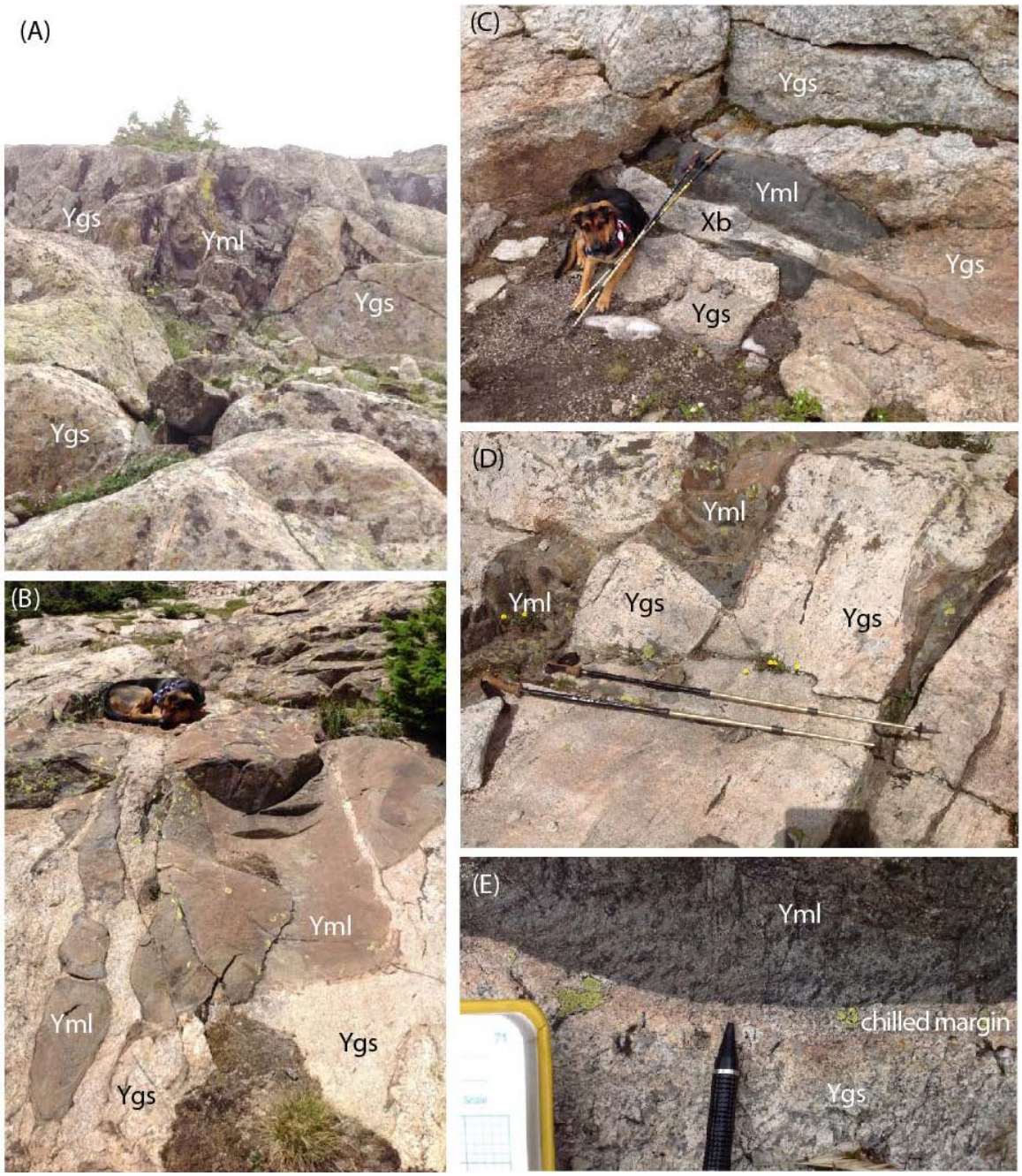

Figure 23. Field relations of metalamprophyre dikes and St. Kevin granite. (A) Black metalamprophyre dike (Yml, 2 m wide) truncated by St. Kevin granite (Ygs). (B) Metalamprophyre intruded by St. Kevin granite, dog for scale. (C) Black metalamprophyre with slivers of original host biotite gneiss (Xb) pendants within St. Kevin granite, dog for scale. (D) Black metalamprophyre dike offset by St. Kevin granite intrusion, hiking poles for scale. (E) St. Kevin granite contact with chilled margins against metalamprophyre with truncated foliations, pencil for scale.

Mesoproterozoic St. Kevin Granite

Location

The St. Kevin granite occurs throughout the field area, with the highest concentrations in the shallow structural domain IV in the southern half of the Homestake Reservoir quadrangle. The St. Kevin granite intrudes into all subdivisions of Paleoproterozoic gneiss, and intrudes into metalamprophyres.

Orientation

In map scale, small lenses of St. Kevin granite are oriented approximately parallel to preexisting axial planar foliations in adjacent Paleoproterozoic gneiss. In outcrop to thin section-scale, the St. Kevin granite sharply truncates preexisting axial planar foliations in Paleoproterozoic gneiss. Moderate to weak foliations in the St. Kevin granite are defined by biotite-rich selvages and aligned coarse euhedral microcline grains (Figure 13).

Age

The St. Kevin granite sharply truncates preexisting Paleoproterozoic gneiss axial planar foliations. St. Kevin granite truncates, intrudes into, and contains chilled margins against the Metalamprophyre dikes (Figure 23). In few locations, the St. Kevin granite entirely surrounds pendants of older metalamprophyres and Paleoproterozoic gneiss. U-Pb zircon dating suggests that the St. Kevin granite crystallized ca. 1425 ±12 Ma (Moscati, personal communication).

Mesoproterozoic Shear Deformation

Location

Concentrated shear deformation in Paleoproterozoic gneiss is located in the HSZ in the Mount of the Holy Cross quadrangle and the SLSZ in the southeastern Mount of the Holy Cross and northeastern Homestake Reservoir quadrangles (Figure 1). Localized shear deformation also is located along the margins of metalamprophyre dikes and in the St. Kevin granite in the northern Homestake Reservoir quadrangle.

Orientation

Shear deformation is generally oriented parallel to preexisting axial planar foliations in Paleoproterozoic gneiss (Figure 17) (Shaw et al., 2001). Shear deformation is also oriented parallel to metalamprophyre dike contacts (Figure 22). In rare occurrences, localized shear deformation is orthogonal to preexisting foliations or dike margins (Figure 15).

Shear Sense Indicators

Shear sense indicators in the HSZ, SLSZ, metalamprophyres, and St. Kevin granite include sigma and delta rotated clasts with grain tails, mica fish and bent micas, c and c’-type shear bands, shear band fragmented porphyroblasts, asymmetric folds, quarter mats, offset markers, boudins, and deflected markers. Shear sense indicators are identified in oriented thin sections (Figure 24) or in outcrops (Figure 25) along reference planes oriented perpendicular to foliations and parallel to lineation. Metalamprophyre

dikes display weak shear sense indicators near their centers, and stronger indicators near the more highly deformed margins (Figure 26).

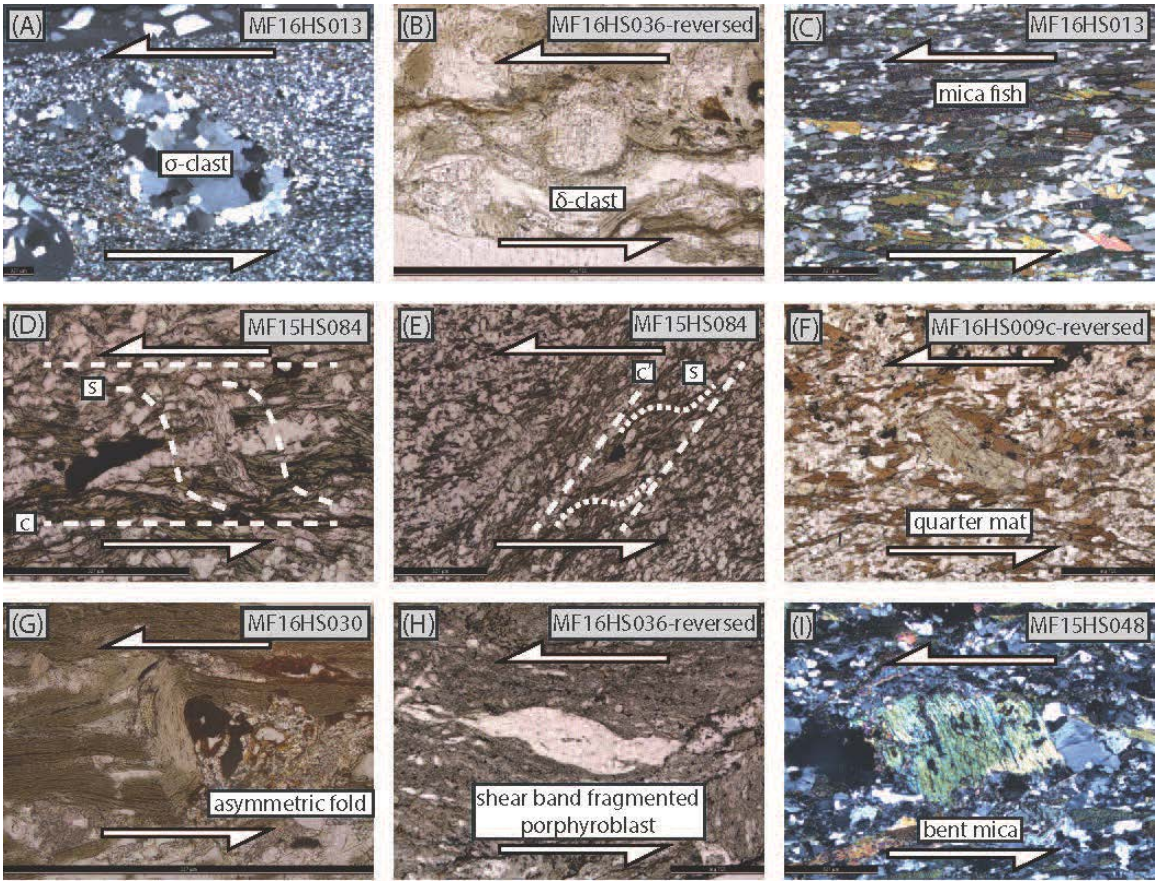

Figure 24. Shear sense indicators. (A) sigma clast in XPL, (B) delta clast in PPL, (C) mica fish in XPL, (D) C-type shear bands in PPL, (E) C'-type shear bands in PPL, (F) quarter mat in PPL, (G) asymmetric fold in PPL, (H) shear band fragmented porphyroblast in PPL, and (I) bent mica in XPL. Scale bars are 327 μm and all thin sections show top to the left shear sense.

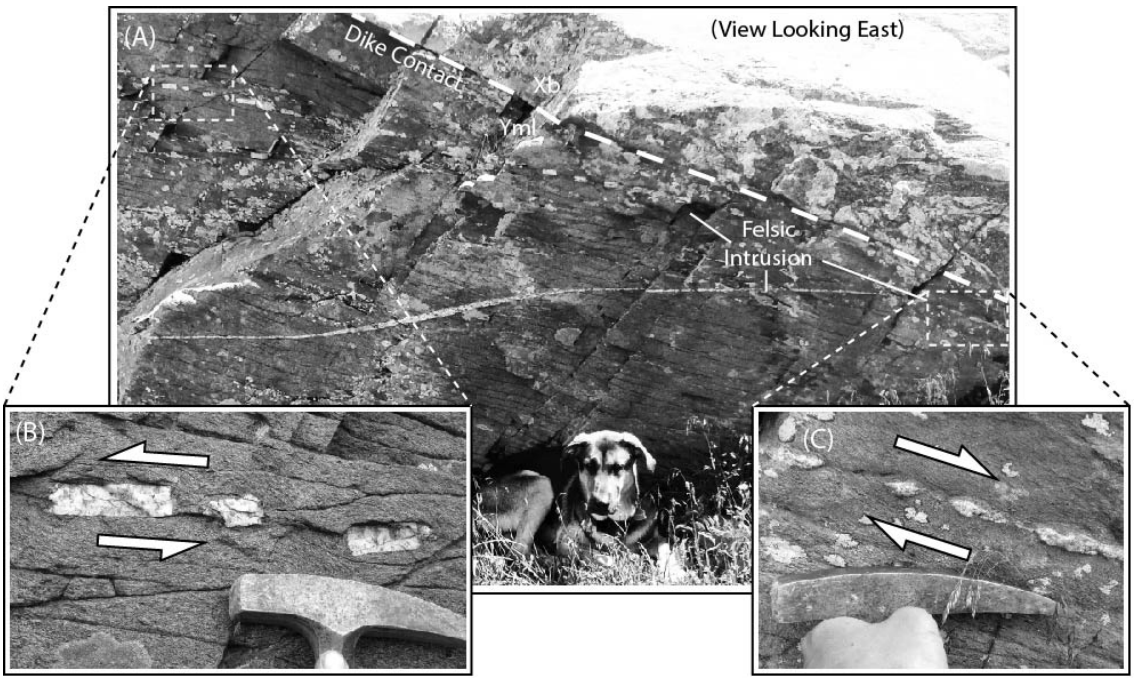

Figure 25. Metalamprophyre dike and boudinage of felsic intrusions. (A) Metalamprophyre (Yml) dike containing deformed felsic intrusions, hosted by biotite gneiss and schist (Xb) country rock. Outcrop photo looking east, dog for scale. (B) Domino boudins with minor porphyroclast tails showing top to the north shear sense and north south extension along foliation planes. Hammer for scale. (C) Shearband boudins near dike contact showing top to the south shear sense. Hammer for scale.

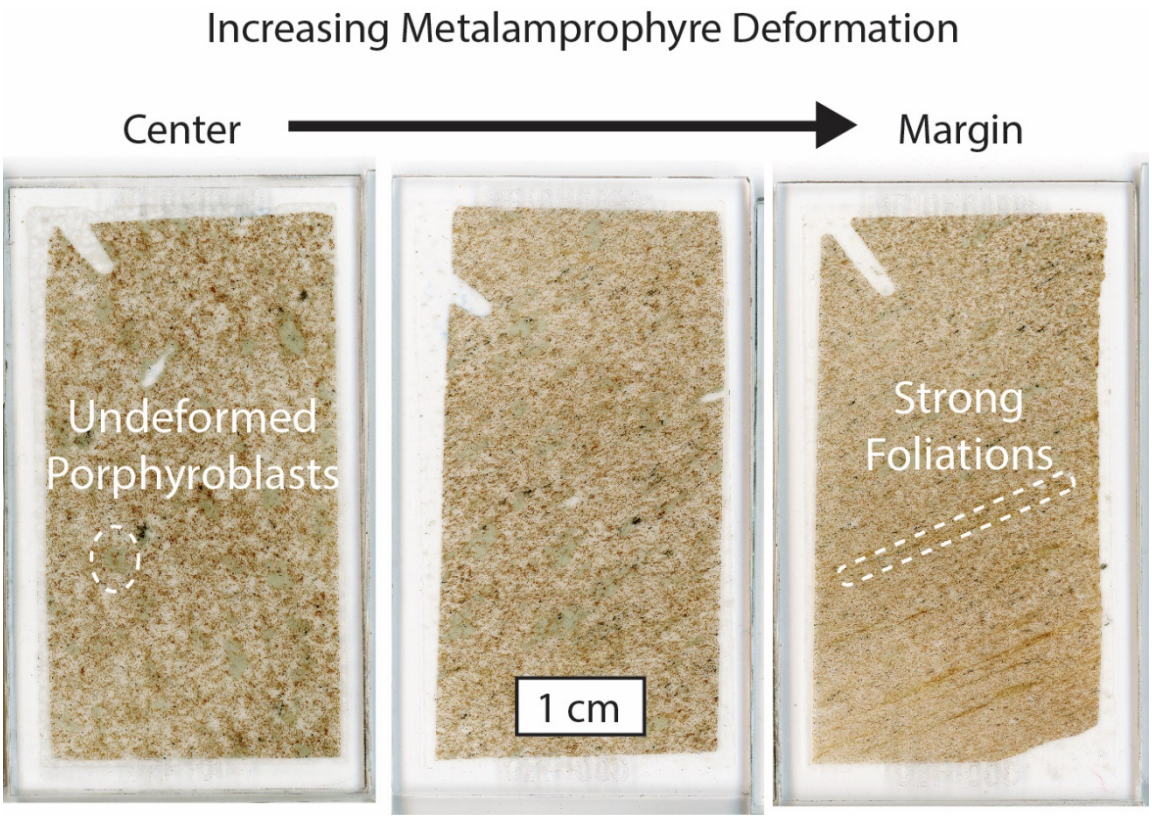

Figure 26. Increasing metalamprophyre deformation near margins. PPL thin section scan on the left is 30 cm from the dike margin and scan on the right is 1 cm from the dike margin.

Age

Shearing deforms Paleoproterozoic gneiss, metalamprophyres, and the St. Kevin granite. In few locations, mylonite shear deformation in the HSZ is truncated by the St. Kevin granite (Shaw, 2001). Early shear deformation in metalamprophyres is also truncated by the St. Kevin granite (Figure 23).

Electron microprobe U-Th-Pb dating of monazite crystallization associated with shear fabric growth suggests that shear deformation in the HSZ occurred between 1420-1380 Ma (Shaw et al., 2001). Relative dating from this research reveals that the earliest

deformation was hosted by metalamprophyres and occurred prior to the ca. 1425 ± 12 Ma (Moscati, personal communication) crystallization of the St. Kevin batholith.

CHAPTER SIX

TEMPERATURE OF DEFORMATION

Temperature of deformation of metalamprophyre dikes and St. Kevin granite boudins is calculated to constrain and compare shear deformation conditions in and around the Homestake Reservoir quadrangle research area, with respect to regional thermal metamorphism. Thermometry is conducted on sample MF16HS029 (Figure 25,Figure 27) which contains a metalamprophyre dike hosting deformed felsic intrusion related to the St. Kevin granite. Analysis includes characterization of temperature-related quartz deformation textures in thin section, as well as titanium in quartz deformation thermometry (Wark and Watson, 2006) using an electron microprobe.

Metalamprophyres and St. Kevin Granite

Deformation Textures

Recrystallized tails of sheared, domino boudins from Figure 25 display temperature-dependent deformation textures in quartz. Recrystallized quartz grains display undulose extinction (Figure 27), representing subgrain rotation (SGR) formed between approximately 400-500 °C (Stipp et al., 2002). Recrystallized quartz grains also display serrated grain boundaries (Figure 27), representing grain boundary migration (GBR) formed between approximately 500-600 °C (Stipp et al., 2002). Additionally, there is relative little SGR and GBM in deformed feldspar which would require sustained temperatures above 450 ºC for an extended period of time (Tullis and Yund, 1991).

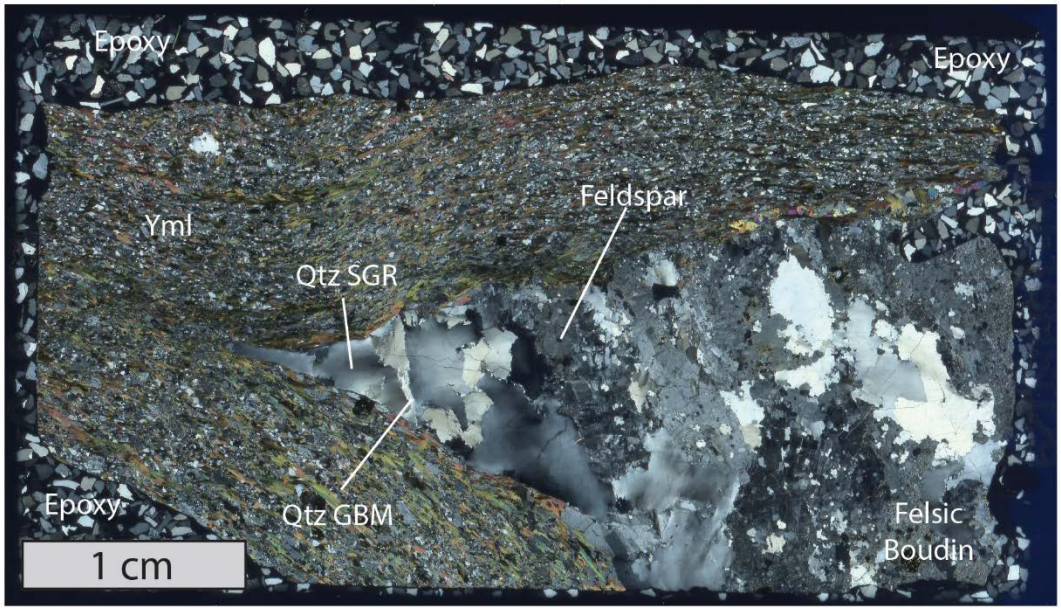

Figure 27. Temperature-dependent deformation textures in quartz. Whole thin section scan (XPL) of sample MF16HS029 of metalamprophyre (Yml) hosting felsic boudin, displaying undulose extinction in quartz representing subgrain rotation (SGR), serrated grain boundaries in quartz representing grain boundary migration (GBM), and relatively undeformed feldspar grains.

TitaniQ

Titanium in quartz thermometry supplements characterization of temperature-dependent deformation textures in quartz. Using the *TitaniQ* thermometer by Wark and Watson (2006), deformation of recrystallized tails of felsic boudins in sample MF16HS029 (Figure 27) records the temperature at which titanium re-equilibrated in quartz during ductile shearing of the metalamprophyre dike. WDS electron microprobe calculation of weight percent concentration of titanium was conducted on 12 quartz grains in the presence of rutile (Figure 28). Analysis is plotted on Table 1, excluding sample points that are less than 100 µm away from rutile, contributing to unwanted secondary fluorescence. An average deformation temperature was calculated at 564 ±45 °C, based on an average 16.5 ppm of titanium.

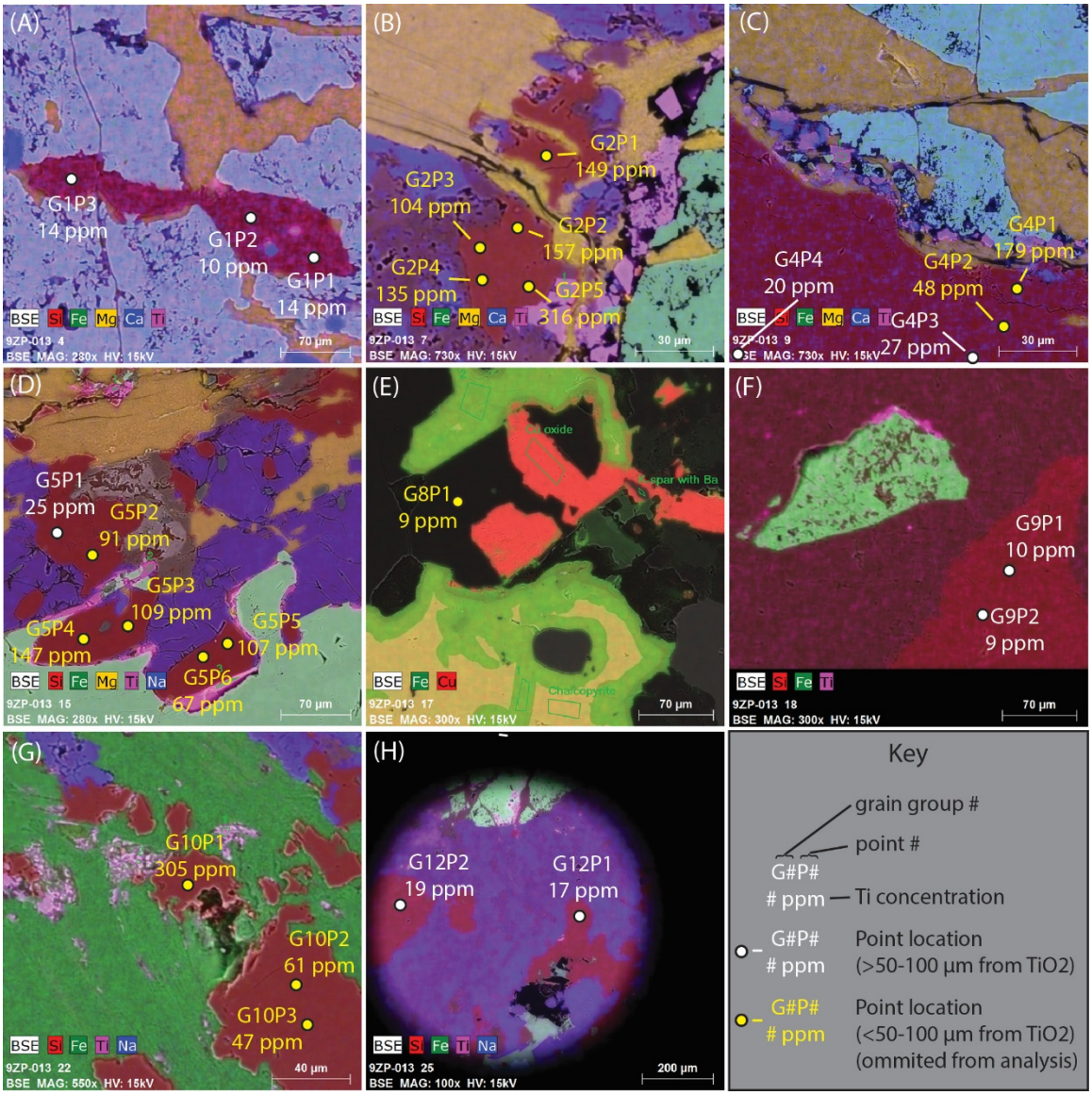

Figure 28. Back Scattered Electron (BSE) images of sampling locations. False colored images of (A) grain group 1, (B) grain group 2, (C) grain group 4, (D) grain group 5, (E) grain group 8, (F) grain group 9, (G) grain group 10, (H) grain group 12. White sampling points were used for analysis, yellow sampling points were omitted from analysis.

Sample	Ti (ppm)	T (°C)
G1P1	14	556
G1P2	10	530
G1P3	14	556
G4P3	27	611
G4P4	20	585
G5P1	25	604
G9P1	10	530
G9P2	9	522
G12P1	17	571
G12P2	19	581
stddv	6.0	30
mean	**16.5**	**564**

Table 1. Titanium concentration and deformation temperatures.

Regional Deformation

Various temperatures of deformation are recorded in other locations outside of the high concentrations of metalamprophyres in the Homestake Reservoir quadrangle. In the HSZ, mylonite deformation reached approximately 300 to 500 ºC (Figure 32) and ultramylonite deformation reached approximately 250 to 350 ºC based on quartz and feldspar deformation microstructures (Hirth and Tullis, 1994; Shaw et al., 2001). The HSZ in structural domain I is located to the north of the high concentration of metalamprophyres in structural domain II (Figure 1). In the SLSZ, mylonite deformation temperatures reached approximately 280 to 600 ºC (Figure 32) based on Electron Backscatter Diffraction (EBSD) analysis of lattice preferred orientations of deformed quartz slip mechanisms (Lee et al., 2012; Stipp et al., 2002). The SLSZ in structural domain III is located immediately to the east of the high concentration of metalamprophyres in structural domain II, and immediately northeast of the abundant granite in structural domain IV (Figure 1). Regional thermal metamorphism, broadly coeval to metalamprophyre deformation occurred at approximately 300 to 500 ºC (Figure

32), based on regional $^{40}Ar/^{39}Ar$ thermochronologic data and bracketed mineral closure temperatures (Shaw et al., 2005). Regional temperatures include samples throughout Colorado and New Mexico, with highly varied proximity to the metalamprophyres in the Homestake Reservoir quadrangle.

CHAPTER SEVEN

DISCUSSION

This study highlights metalamprophyres as crucial components in a kinematically-linked deformation system consisting of dikes, batholiths, and shear zones. Metalamprophyre emplacement and deformation demonstrates the role of inherited structural controls and advective heating influencing Mesoproterozoic middle crustal deformation in the Northern Sawatch Range. Specifically, this research emphasizes the favorable orientations of preexisting fabrics, locally increased temperatures affecting rheology, and the distinct progression events manifesting a multi-faceted deformation system, supporting significant intracontinental tectonism in southwestern Laurentia in the Mesoproterozoic.

Timeline of Geologic Events

This research identifies a timeline of geologic events occurring in the Homestake Reservoir and surrounding quadrangles, focusing on Proterozoic magmatism, metamorphism, and deformation (Figure 29). These geologic events are also outlined in a series of cartoon cross sections of the research area (Figure 30). The timeline begins with metamorphism and deformation of Paleoproterozoic gneiss ca. 1710-1630 Ma (Shaw et al., 2001), creating the characteristic axial planar foliations that define structural domains I-IV (Figure 16). Lamprophyre dikes then intrude into the Paleoproterozoic country rock along preexisting axial planar foliations. Metalamprophyres are metamorphosed in the

upper amphibolite facies, and are deformed by the earliest stages of shear deformation in the research area. Following the early deformation hosted by metalamprophyre dikes, the St. Kevin granite is emplaced ca. 1425 ±12 Ma (Moscati, personal communication). During and after the St. Kevin granite was emplaced, concentrated shear zone deformation occurs ca. 1420-1380 Ma in the HSZ (Shaw et al., 2001), as well as the nearby SLSZ (Lee et al., 2012).

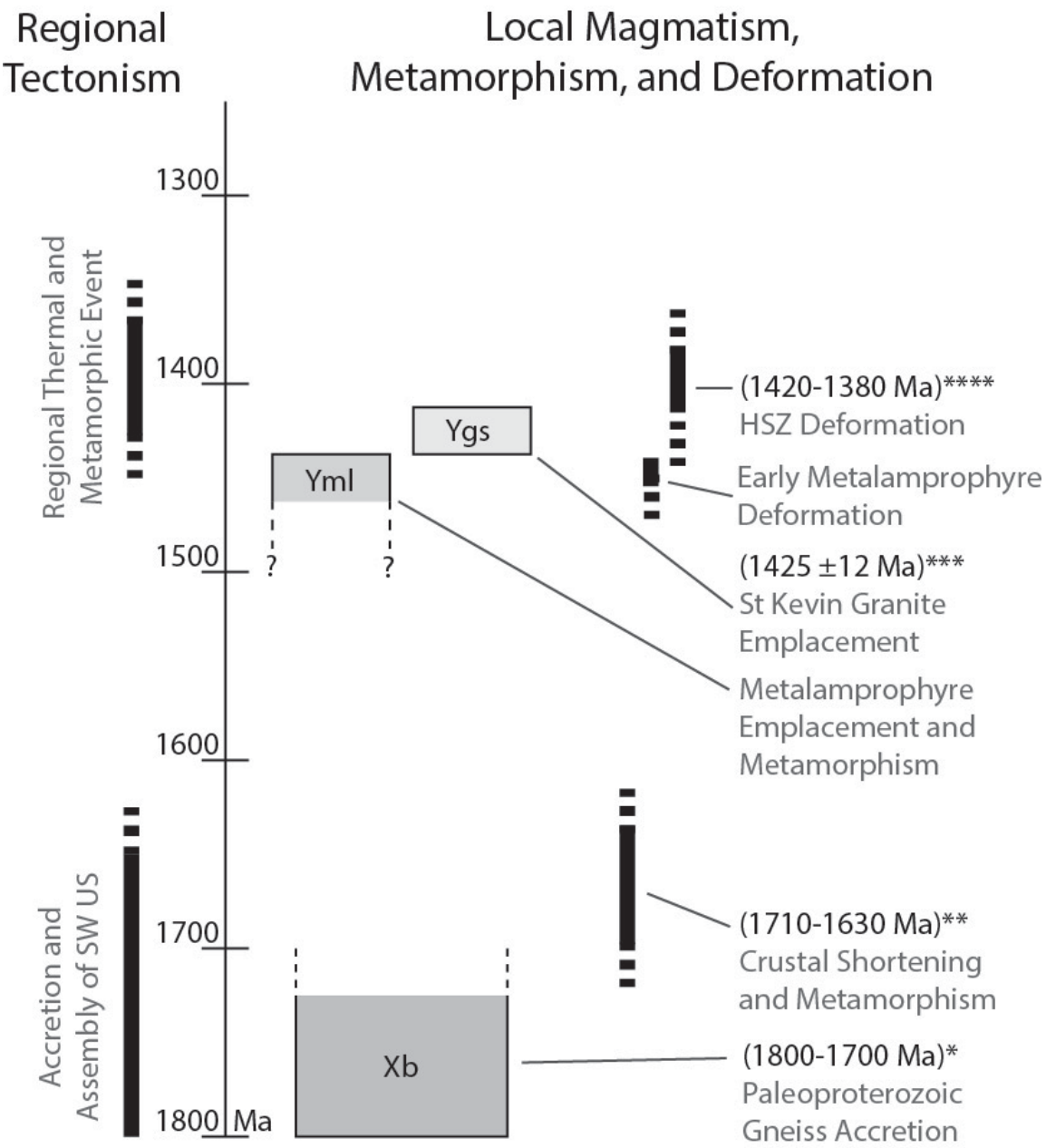

Figure 29. Timeline of Proterozoic tectonic events. Regional (left side) versus Local (right side) tectonic events in the Homestake Reservoir and adjacent quadrangles with oldest events at the bottom and youngest events at the top. Rectangles represent first occurrence of rocks; biotite gneiss (Xb), metalamprophyres (Yml), and St. Kevin granite (Ygs). Black bars represent approximate timing and duration of events, and are dashed when questionable. Absolute dating is from (*) (Whitmeyer and Karlstrom, 2007), (**) (Shaw et al., 2001), (***) (Moscati, personal communication), and (****) (Shaw et al., 2001).

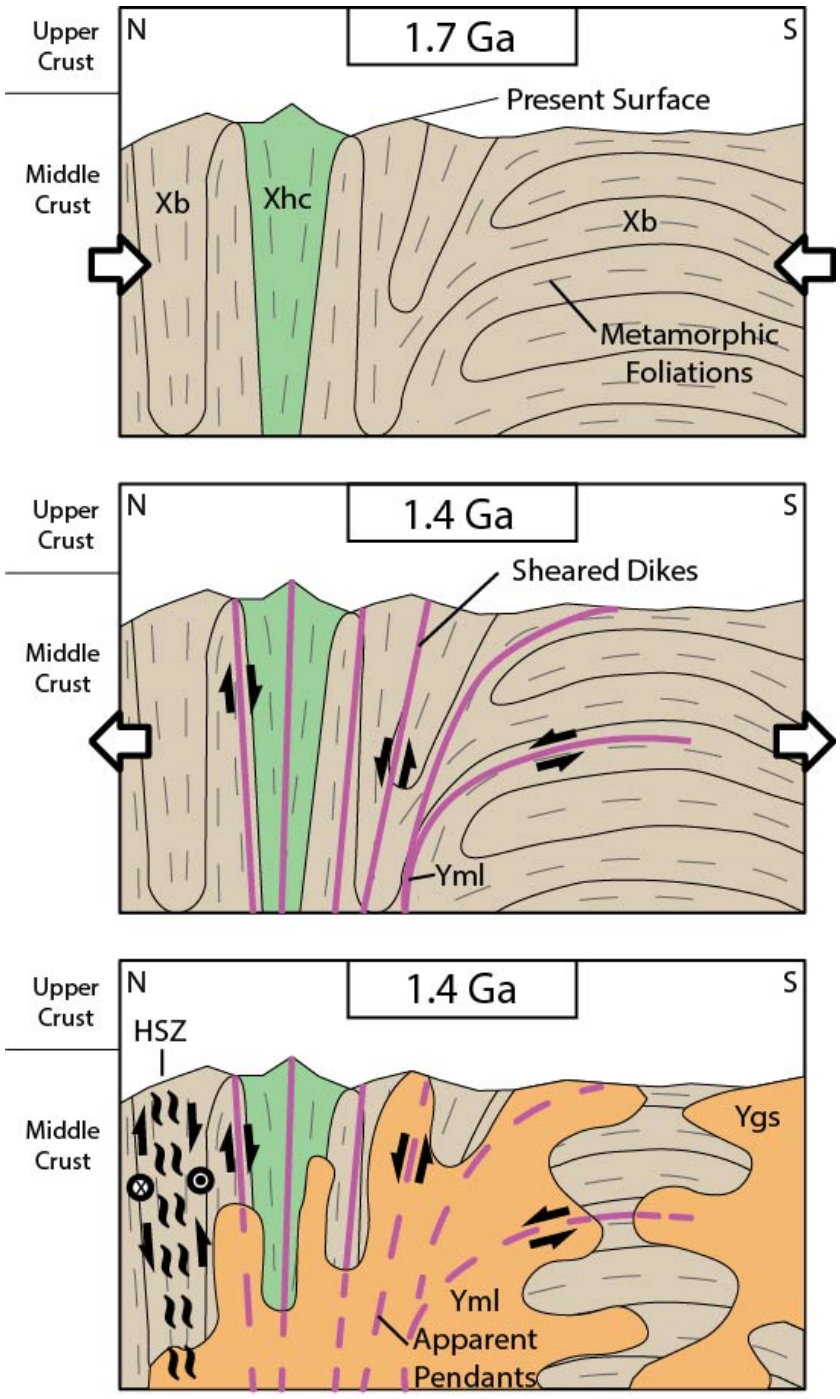

Figure 30. Deformation history cartoon. (A) Vertical foliations in Paleoproterozoic gneiss (Xb, Xhc) and horizontal foliations due to north south shortening ca. 1.7 Ga. (B) Metalamprophyre dikes (Yml) intruding and shearing along preexisting foliations, within localized north-south extension ca. 1.4 Ga. (C) Granite (Ygs) intruding along preexisting foliations and surrounding Yml apparent pendants, continued shearing along Yml dikes, and dextral to oblique shearing in the Homestake Shear Zone (HSZ) to the north ca. 1.4 Ga.

Inherited Structural Control

Igneous intrusion and shear zone deformation in the Homestake Reservoir quadrangle are oriented approximately parallel to preexisting metamorphic fabrics, exhibiting an inherent structural control along preexisting fabrics. Metalamprophyre dikes intrude mostly along west striking, subvertical foliations in Paleoproterozoic gneiss in structural domain II. This orientation suggests a component of localized north-south extension, facilitating the majority of dike emplacement along favorably oriented axial planar foliations in Paleoproterozoic gneiss. Outside of the east striking steep foliations in structural domain II, dikes are still oriented parallel to host foliations, but their concentration significantly diminishes (Plate I), suggesting that orientation of preexisting fabrics was considerably less favorable for extension and accommodation of dikes.

Thin lenses of granite along the margins of the St. Kevin batholith are also parallel to preexisting axial planar foliations in adjacent Paleoproterozoic gneiss. Undeformed, aligned microcline phenocrysts and biotite selvages in granite are also aligned parallel to preexisting foliations. These foliations in granite (Figure 13), lacking signs of solid-state deformation (Vernon, 2000), are suggestive of magmatic flow and inherited structures due to similar emplacement along foliations.

Deformation fabrics in multiple rock types are also oriented parallel to axial planar foliations in adjacent Paleoproterozoic gneiss, suggesting structural controls on deformation as well as magmatism. Shear zone fabrics in the HSZ, SLSZ, along margins of metalamprophyre dikes, and other localized outcrops contain a variety of shear fabrics, but they are consistently parallel to surrounding, preexisting foliations. Figure 22

demonstrates multiple orientations of dike contacts and lineations, but the deformation fabrics are always oriented parallel to the foliations of the host gneiss. Shear deformation partitioned along the margins of the metalamprophyre dike in Figure 31 highlights how the rigid contact with host gneiss partitions strain within the dike along its margins.

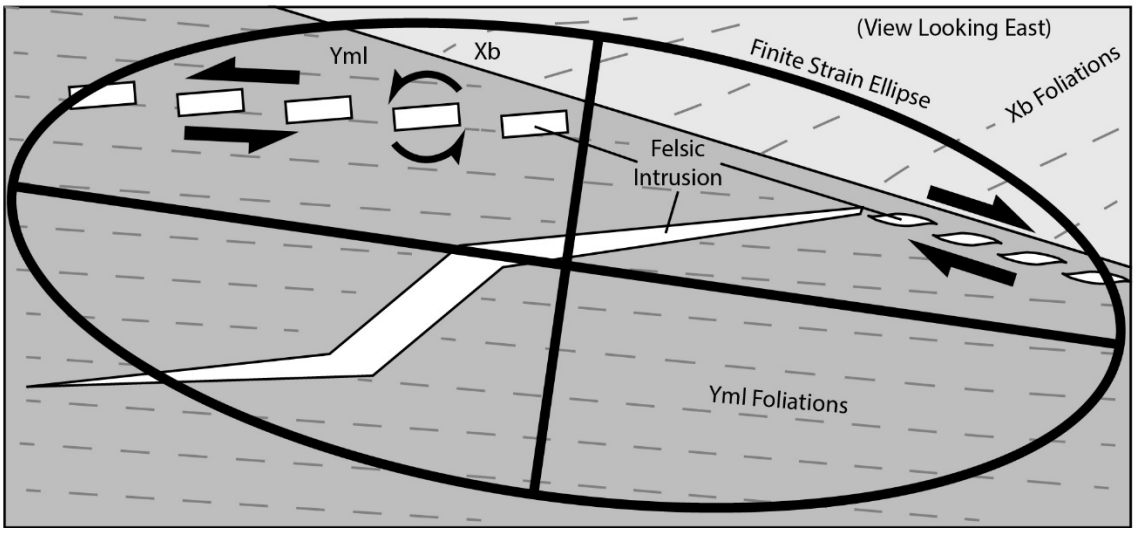

Figure 31. Strain partitioning along dike contacts. Cartoon of Figure 25 demonstrating opposite sense of shear in relation to orientation of dike (Yml) contact with host gneiss (Xb). Shear sense arrows and finite strain ellipse are in black.

Temperature of Deformation

The minimum temperature of metalamprophyre and boudin deformation in sample MF16HS029 is calculated at 564 ±45 °C using titanium in quartz thermometry (Wark and Watson, 2006), and is confirmed by serrated grain boundary quartz deformation textures (Figure 27) indicative of GBM at 500-600 °C (Stipp et al., 2002). Localized deformation temperatures in this sample are higher than coeval deformation temperatures (Figure 32) in the HSZ (280-500 ºC) (Lee et al., 2012; Shaw et al., 2001) and regional thermal metamorphism (300-500 ºC) (Shaw et al., 2005). Locally increased

temperatures of deformation may be due to advective heating, brought up by the dike itself. This locally elevated temperature may have enhanced rheologic contrasts across the dike contact with Paleoproterozoic gneiss, and allowed strain to be focused only within the thin margins of the dike. The advective heating of localized magmatism supports higher temperatures of deformation in metalamprophyres and the adjacent SLSZ, in comparison to the more distal HSZ and regional thermal metamorphism (Shaw et al., 2005) across Colorado and New Mexico.

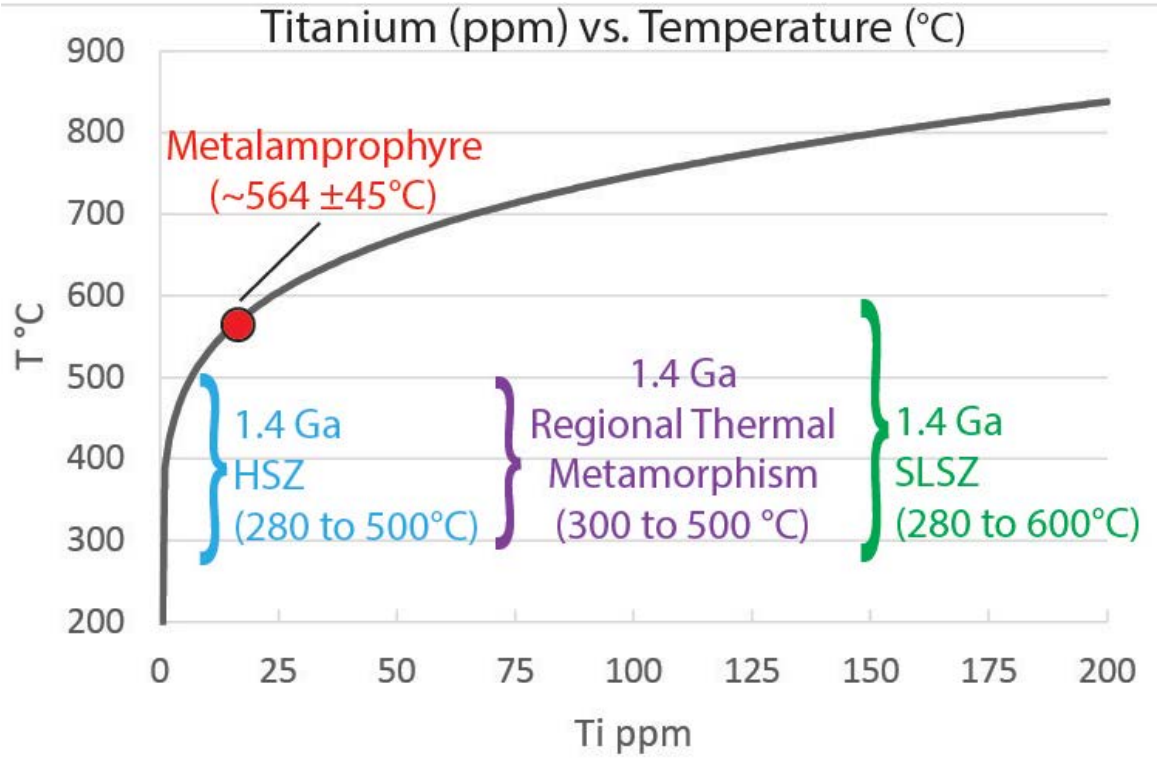

Figure 32. TitaniQ deformation temperature. Graph showing temperature of deformation (ºC) versus titanium in quartz weight percent concentration (ppm) for metalamprophyre sample MF16HS029 (red) in relation to deformation temperatures of the nearby HSZ (blue) (Shaw et al., 2001) and SLSZ (green) (Lee et al., 2012).

Continuum of Deformation

Kinematic analysis and age relations demonstrate that a continuum of metalamprophyre deformation occurred over an extended period of time, bracketing the St. Kevin granite intrusion. Figure 33A demonstrates that foliated metalamprophyres are truncated abruptly by the intruding St. Kevin granite. Additionally, Figure 33C demonstrates that shear deformation in metalamprophyres also occurs following the St. Kevin granite intrusion. This series of cross cutting relations brackets metalamprophyre deformation as occurring before and after the St. Kevin granite intrusion (Figure 29).

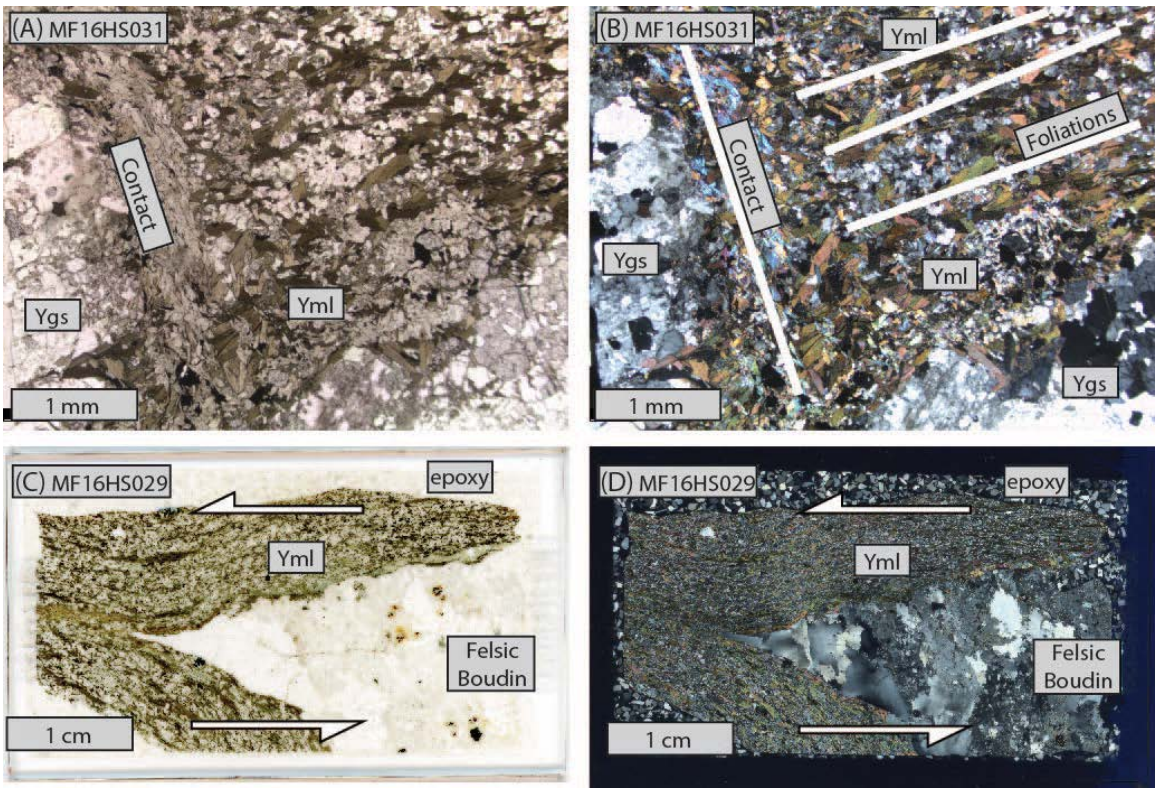

Figure 33. Continuum of deformation. (A) PPL and (B) XPL photomicrograph of granite (Ygs) intruding into and truncating preexisting foliations of metalamprophyre dike (Yml). (C) PPL and (D) XPL thin section scan of felsic boudin within metalamprophyre (Yml), both showing top to the left (north) shear.

Lineations in metalamprophyre dikes have different orientations from the dike center to the dike margin (Figure 22, Figure 26). A bimodal population of lineations suggest that orientations of strain may have changed throughout the course of metalamprophyre deformation. Also, the folded biotite grain in Figure 24H, previously in line with foliations, demonstrates overprinting deformation events. Overprinting deformation could represent two unique deformation events, or a continuum of deformation over a period of time.

This research suggests a continuum of deformation, in support of a prolonged shear zone deformation system. A single, finite strain ellipse in Figure 25 demonstrates how one deformation event may partition strain with different shear senses in the same outcrop. This supports the model that varied timing and orientations of deformation could record a relatively uniform progression of continued deformation through time.

Metalamprophyre foliations that predate the St. Kevin granite emplacement provide evidence for the primary stages of shear zone deformation in the Homestake Reservoir quadrangle and surrounding research area. This emphasizes that the early intrusion of lamprophyre dikes, and the localized heat they provide are critical to understanding the relation between dikes, batholiths and shear zones in a middle crustal deformation system.

Intracontinental Deformation and the Picuris Orogeny

Igneous intrusion and concentrated shear zone deformation in the Homestake Reservoir quadrangle, far from known coeval plate boundaries, suggest tectonic activity

related to intracontinental deformation ca. 1.4 Ga (Allen et al., 2002; Lee et al., 2012; Nyman et al., 1994; Shaw et al., 2001). Dike intrusion, batholith intrusion, and shear zone deformation temporally and spatially related, and support a model for kinematically-linked deformation in the middle continental crust. The recently identified Picuris Orogeny in northern New Mexico (Figure 3) (Daniel et al., 2013) includes evidence for shear zone deformation and aluminosilicate triple-point metamorphism (Aronoff et al., 2016; Daniel et al., 2016) and may provide a tectonic link to intracontinental deformation in the Homestake Reservoir quadrangle.

The ca. 1.4 Ga northwest-southeast convergence documented in the Picuris Orogeny (Daniel et al., 2013) is a possible driver for deformation hundreds of kilometers away into the Homestake Reservoir quadrangle (Shaw and Allen, 2007). In this model, favorable orientations of preexisting weaknesses may have helped localize strain around localized thermal anomalies associated with lamprophyre dikes in addition to in mylonite, ultramylonite, and pseudotachylyte in the HSZ and SLSZ (Allen and Shaw, 2013; Lee et al., 2012; Tweto and Sims, 1963). The interaction between dike intrusion, batholith emplacement, and shear zone deformation in the Homestake Reservoir quadrangle offers a unique view into a multi-faceted, kinematically linked system of deformation, critical to understanding middle continental crustal effects of intracontinental deformation.

Summary

Metalamprophyre dikes in the Homestake Reservoir quadrangle provide evidence for concentrated solid state deformation ca. 1.4 Ga within the margins of individual dikes.

Dike deformation is correlated temporally and spatially to the HSZ and SLSZ, but is not constrained within the strictly defined and mapped shear zones (Plate I) (Allen and Shaw, 2013; Lee et al., 2012). Dike emplacement and kinematics of deformation follow closely to preexisting fabrics defining structural domains (Figure 18, Plate I). Concentration of shear deformation in dikes is influenced both by elevated temperatures from igneous intrusion, as well as the contrasting rheology between the dikes and their host rock contacts, focusing deformation along the dike margins. Structurally influenced dike emplacement and subsequent deformation supports the role in preexisting fabrics controlling orientations of 1.4 Ga deformation in and around the Homestake Reservoir quadrangle.

Deformation in metalamprophyre dike marks the furthest southwestern extent of deformation associated with the HSZ and SLSZ. Mesoproterozoic shear zone deformation occurs not only along preexisting fabrics in the HSZ and SLSZ (Allen and Shaw, 2013; Shaw et al., 2001; Tweto and Sims, 1963), but also along metalamprophyre dike margins. This is the first comprehensive analysis of deformation concentrated in metalamprophyre dikes in the Homestake Reservoir quadrangle, identifying the spatial and temporal relation of dike deformation to other igneous intrusion and shear zone deformation in the Northern Sawatch Range.

CHAPTER SEVEN

FUTURE WORK

Future work on geochronology, kinematic analysis, and geologic mapping will better constrain the temporal, spatial, and conditional relations of dikes, batholiths, and shear zone deformation in the Homestake Reservoir and surrounding quadrangles (Figure 1). This work includes laboratory analysis of oriented samples that are already collected, in addition to significant field work and sample collection for continued research.

Isotope Geochronology

Future work on timing and conditions of deformation in the Homestake Reservoir and surrounding quadrangles will contribute to identifying kinematic links between igneous intrusions and shear zone deformation ca. 1.4 Ga. Isotope geochronology may provide absolute dating to complement relative dating of lamprophyre intrusion from this study. Geologic mapping and thin section petrography suggest that lamprophyres intruded prior to the 1425 ± 12 Ma crystallization of St. Kevin batholith (Moscati, personal communication). Additional dating will clarify the age of dike intrusion and could reveal the earliest onset of localized deformation in the Homestake Reservoir quadrangle.

Electron Backscatter Diffraction

Electron Backscatter Diffraction (EBSD) analysis may identify styles and temperatures of deformation in dikes and small localized splays of the HSZ and SLSZ adjacent to the dikes. Lattice preferred orientation of quartz analysis should include multiple samples near both the center and contact of individual dikes, in addition to samples along dikes of various orientations. This will identify how dike orientation affects deformation, and how progressive deformation within a single dike may have changed through time. Sampling of shear fabrics outside of the dikes may also demonstrate contrasting deformation across rheologic or temperature variations in the host rock.

Anisotropy of Magnetic Susceptibility

Anisotropy of Magnetic Susceptibility (AMS) analysis may identify pervasive versus localized deformation across the St. Kevin batholith in relation to other deformation fabrics in the Homestake Reservoir quadrangle. Current evidence for deformation in the St. Kevin batholith is limited to boudinage of related felsic intrusions and localized mylonite fabric and pseudotachylyte intrusion (Shaw, personal communication), and lacks representative data of the whole batholith. A wide suite of sampling will identify how deformation and rotation of magnetically aligned minerals occurred throughout the batholith, as well as how deformation may vary in proximity to dikes, shear zones, batholith boundaries, variations in igneous facies, or variations in preexisting fabrics.

Geologic Mapping of the Nast Quadrangle

Further geologic mapping may incorporate additional isotope geochronology, EBSD, and AMS analysis into a cohesive geologic framework demonstrating the interplay of igneous intrusions and shear zone deformation. The Nast quadrangle is directly to the west of the Homestake Reservoir quadrangle, and is due for a 7.5', 1:24,000-scale geologic map. Previous geologic mapping in this quadrangle is limited to an insufficient, 1 by 2º, 1:250,000 map by Tweto et al. (1978). This quadrangle contains the intersection between dike intrusion, St. Kevin batholith emplacement, and shear zone deformation, as seen in Figure 25. The Geologic Map of the Nast quadrangle will be essential to understanding the geospatial, kinematic links between multiple elements of Mesoproterozoic deformation in the Northern Sawatch Range, and its relation to intracontinental deformation across Laurentia.

CHAPTER EIGHT

CONCLUSION

Through geologic mapping and kinematic analysis, this study identifies how intrusion and deformation of dikes, batholiths, and shear zones record Mesoproterozoic middle continental crustal deformation in the Homestake Reservoir quadrangle near Leadville, Colorado. Favorable orientations of preexisting fabrics, and localized advection of heat due to magmatism allow metalamprophyre dikes to deform along their margins in kinematically-linked shear deformation. Axial planar foliations in Paleoproterozoic gneiss controlled parallel orientations of subsequent igneous intrusions and deformation. Locally increased deformation temperatures (500-600 °C), relative to the coeval HSZ and regional thermal metamorphism allowed metalamprophyre dikes to partition strain in the earliest pulse of shear zone deformation, and perhaps influence a progressive continuum of deformation.

Research on a this multi-faceted system of deformation in the Homestake Reservoir quadrangle illustrates a unique view of middle crustal effects of preexisting weaknesses and advective heating localizing Proterozoic intracontinental deformation. With correlations of Proterozoic to modern tectonism, this research provides insight to conditions of modern intracontinental mountain building such as the Tien Shan, in which the middle crust may be actively deforming today, yet still remains deeply buried and unavailable to research geologists for perhaps another billion years.

REFERENCES CITED

Allen, J. L., 2004, Timing, style, and significance of Cambrian through Laramide brittle reactivation along the Proterozoic Homestake shear zone, Colorado mineral belt: Rocky Mountain Geology, v. 39, no. 2, p. 65-84.

Allen, J. L., 2005, A multi-kilometer pseudotachylyte system as an exhumed record of earthquake rupture geometry at hypocentral depths (Colorado, USA): Tectonophysics, v. 402, no. 1, p. 37-54.

Allen, J. L., O'Hara, K. D., and Moecher, D. P., 2002, Structural geometry and thermal history of pseudotachylyte from the Homestake shear zone, Sawatch Range, Colorado: Field Guides, v. 3, p. 17-32.

Allen, J. L., and Shaw, C. A., 2013, Seismogenic fault-zone processes and heterogeneity recorded by pseudotachylyte: New insights from the Homestake shear zone, Colorado: Field Guides, v. 33, p. 165-183.

Allmendinger, R. W., Cardozo, N., and Fisher, D. M., 2011, Structural geology algorithms: Vectors and tensors, Cambridge University Press.

Anderson, H. E., and Davis, D. W., 1995, U–Pb geochronology of the Moyie sills, Purcell Supergroup, southeastern British Columbia: implications for the Mesoproterozoic geological history of the Purcell (Belt) basin: Canadian Journal of Earth Sciences, v. 32, no. 8, p. 1180-1193.

Anderson, J. L., and Bender, E. E., 1989, Nature and origin of Proterozoic A-type granitic magmatism in the southwestern United States of America: Lithos, v. 23, no. 1-2, p. 19-52.

Armstrong, R. L., 1968, Sevier orogenic belt in Nevada and Utah: Geological Society of America Bulletin, v. 79, no. 4, p. 429-458.

Aronoff, R. F., Andronicos, C. L., Vervoort, J. D., and Hunter, R. A., 2016, Redefining the metamorphic history of the oldest rocks in the southern Rocky Mountains: Geological Society of America Bulletin, v. 128, no. 7-8, p. 1207-1227.

Aronoff, R. F., Vervoort, J., Andronicos, C., and Hunter, R., Evidence for a circa 1.4 Ga metamorphic event from Lu-Hf garnet geochronology in the Tusas and Picuris Mountains, northern New Mexico, USA, *in* Proceedings Geological Society of America Abstracts with Programs2012, Volume 44, p. 9.

Barbery, A., Facemyer, C., Allen, J., and Kuehn, S., Petrography and geochemistry of mafic-intermediate dikes from the northern Sawatch Range, Colorado, *in* Proceedings Geological Society of America Abstracts with Programs, 2013, Volume 45, p. 583.

Bennett, V. C., and DePaolo, D. J., 1987, Proterozoic crustal history of the western United States as determined by neodymium isotopic mapping: Geological Society of America Bulletin, v. 99, no. 5, p. 674-685.

Bickford, M. E., and Van Schmus, W. R., 1985, Discovery of Two Proterozoic Granite-Rhyolite Terranes in the Buried Midcontinent Basement: The Case for Shallow Drill Holes, *in* Raleigh, C. B., ed., Observation of the Continental Crust through Drilling I: Proceedings of the International Symposium held in Tarrytown, May 20–25, 1984: Berlin, Heidelberg, Springer Berlin Heidelberg, p. 355-364.

Cardozo, N., and Allmendinger, R. W., 2013, Spherical projections with OSXStereonet: Computers & Geosciences, v. 51, p. 193-205.

Chapin, C. E., 2012, Origin of the Colorado mineral belt: Geosphere, v. 8, no. 1, p. 28-43.

Chapin, C. E., and Cather, S. M., 1994, Tectonic setting of the axial basins of the northern and central Rio Grande rift: Geological Society of America Special Papers, v. 291, p. 5-26.

Condie, K. C., 1980, The Tijeras Greenstone: Evidence for depleted upper mantle beneath New Mexico during the Proterozoic: The Journal of Geology, v. 88, no. 5, p. 603-609.

Daly, J., and McLelland, J., 1991, Juvenile middle Proterozoic crust in the Adirondack highlands, Grenville province, northeastern North America: Geology, v. 19, no. 2, p. 119-122.

Dalziel, I. W., 1991, Pacific margins of Laurentia and East Antarctica-Australia as a conjugate rift pair: Evidence and implications for an Eocambrian supercontinent: Geology, v. 19, no. 6, p. 598-601.

Daniel, C. G., Andronicos, C. L., and Aronoff, R. F., 2016, Regional Al2SiO5 triple-point metamorphic rocks of northern New Mexico: A field trip to honor the career contributions of Lincoln Hollister to petrology and tectonics: Field Guides, v. 44, p. 201-229.

Daniel, C. G., Pfeifer, L. S., Jones, J. V., and McFarlane, C. M., 2013, Detrital zircon evidence for non-Laurentian provenance, Mesoproterozoic (ca. 1490–1450 Ma) deposition and orogenesis in a reconstructed orogenic belt, northern New Mexico, USA: Defining the Picuris orogeny: Geological Society of America Bulletin, v. 125, no. 9-10, p. 1423-1441.

Dickinson, W. R., and Snyder, W. S., 1978, Plate tectonics of the Laramide orogeny: Geological Society of America Memoirs, v. 151, p. 355-366.

Donovan, J. J., Lowers, H. A., and Rusk, B. G., 2011, Improved electron probe microanalysis of trace elements in quartz: American Mineralogist, v. 96, no. 2-3, p. 274-282.

Donovan, J. J., Singer, J. W., and Armstrong, J. T., 2016, A new EPMA method for fast trace element analysis in simple matrices: American Mineralogist, v. 101, no. 8, p. 1839-1853.

Doughty, P. T., and Chamberlain, K. R., 1996, Salmon River Arch revisited: new evidence for 1370 Ma rifting near the end of deposition in the Middle Proterozoic Belt basin: Canadian Journal of Earth Sciences, v. 33, no. 7, p. 1037-1052.

Evans, K. V., Aleinikoff, J. N., Obradovich, J. D., and Fanning, C. M., 2000, SHRIMP U-Pb geochronology of volcanic rocks, Belt Supergroup, western Montana: evidence for rapid deposition of sedimentary strata: Canadian Journal of Earth Sciences, v. 37, no. 9, p. 1287-1300.

Fell, C., Formolo, S., Pace-Graczyk, K., and Shaw, C. A., Ancestry and Reactivation of the Homestake Shear Zone, *in* Proceedings Rocky Mountain GSA, Boise, ID, 2004.

Frank, T. D., Lyons, T. W., and Lohmann, K. C., 1997, Isotopic evidence for the paleoenvironmental evolution of the Mesoproterozoic Helena Formation, Belt Supergroup, Montana, USA: Geochimica et Cosmochimica Acta, v. 61, no. 23, p. 5023-5041.

Frost, C. D., and Frost, B. R., 1997, Reduced rapakivi-type granites: the tholeiite connection: Geology, v. 25, no. 7, p. 647-650.

Frost, C. D., and Frost, B. R., 2013, Proterozoic ferroan feldspathic magmatism: Precambrian Research, v. 228, p. 151-163.

Gordon, M. B., and Hempton, M. R., 1986, Collision-induced rifting: the Grenville Orogeny and the Keweenawan rift of North America: Tectonophysics, v. 127, no. 1-2, p. 1-25.

Gower, C., Ryan, A., and Rivers, T., 1990, Mid-Proterozoic Laurentia–Baltica: an overview of its geological evolution and a summary of the contributions made by this volume: Mid-Proterozoic Laurentia-Baltica, v. 38, p. 1-20.

Halls, H., and Pesonen, L., 1982, 9: Paleomagnetism of Keweenawan rocks: Geological Society of America Memoirs, v. 156, p. 173-202.

Heller, P., Bowdler, S., Chambers, H., Coogan, J., Hagen, E., Shuster, M., Winslow, N., and Lawton, T., 1986, Time of initial thrusting in the Sevier orogenic belt, Idaho-Wyoming and Utah: Geology, v. 14, no. 5, p. 388-391.

Hirth, G., and Tullis, J., 1994, The brittle-plastic transition in experimentally deformed quartz aggregates: Journal of Geophysical Research: Solid Earth, v. 99, no. B6, p. 11731-11747.

Hoffman, P. F., 1988, United plates of America, the birth of a craton: Early Proterozoic assembly and growth of Laurentia: Annual Review of Earth and Planetary Sciences, v. 16, no. 1, p. 543-603.

Jessup, M. J., Kalstrom, K. E., Connelly, J., Williams, M., Livaccari, R., Tyson, A., and Rogers, S. A., 2005, Complex Proterozoic crustal assembly of southwestern North America in an arcuate subduction system: The Black Canyon of the Gunnison, southwestern Colorado: The Rocky Mountain Region: An Evolving Lithosphere Tectonics, Geochemistry, and Geophysics, p. 21-38.

Jones, J. V., Daniel, C. G., and Doe, M. F., 2015, Tectonic and sedimentary linkages between the Belt-Purcell basin and southwestern Laurentia during the Mesoproterozoic, ca. 1.60–1.40 Ga: Lithosphere, v. 7, no. 4, p. 465-472.

Karlstrom, K., and Bowring, S. A., 1993, Proterozoic orogenic history of Arizona: Precambrian: Conterminous US: Boulder, Colorado, Geological Society of America, Geology of North America, v. 2, p. 188-211.

Karlstrom, K. E., and Bowring, S. A., 1988, Early Proterozoic assembly of tectonostratigraphic terranes in southwestern North America: The Journal of Geology, v. 96, no. 5, p. 561-576.

Karlstrom, K. E., and Humphreys, E. D., 1998, Persistent influence of Proterozoic accretionary boundaries in the tectonic evolution of southwestern North America: Rocky Mountain Geology, v. 33, no. 2, p. 161-179.

Karlstrom, K. E., Williams, M. L., McLelland, J., Geissman, J. W., and Ahall, K., 1999, Refining Rodinia: geologic evidence for the Australia-Western US connection in the Proterozoic, publisher not identified.

Kerrick, D. M., Eminhizer, L. B., and Villaume, J. F., 1973, The Role of Garbon Film Thickness in Electron Microprobe Analysis: American Mineralogist, v. 58, p. 920-925.

Lee, P. E., Jessup, M. J., Shaw, C. A., Hicks, G. L., and Allen, J. L., 2012, Strain partitioning in the mid-crust of a transpressional shear zone system: Insights from the Homestake and Slide Lake shear zones, central Colorado: Journal of Structural Geology, v. 39, p. 237-252.

Lidiak, E. G., Marvin, R. F., Tnomas, H. H., and Bass, M. N., 1966, Geochronology of the midcontinent region, United States: 4. Eastern area: Journal of Geophysical Research, v. 71, no. 22, p. 5427-5438.

Lovering, T. S., and Goddard, E. N., 1950, Geology and ore deposits of the Front Range, Colorado, 2330-7102.

McCoy, A. M., Karlstrom, K. E., Shaw, C. A., and Williams, M. L., 2005, The Proterozoic ancestry of the Colorado Mineral Belt: 1.4 Ga shear zone system in central Colorado: The Rocky Mountain Region: An Evolving Lithosphere Tectonics, Geochemistry, and Geophysics, p. 71-90.

McWilliams, M., and Dunlop, D., 1978, Grenville paleomagnetism and tectonics: Canadian Journal of Earth Sciences, v. 15, no. 5, p. 687-695.

Moores, E., 1991, Southwest US-East Antarctic (SWEAT) connection: a hypothesis: Geology, v. 19, no. 5, p. 425-428.

Moscati, personal communication.

Nyman, M., Karlstrom, K., Kirby, E., and Graubard, C., 1994, Mesoproterozoic contractional orogeny in western North America: Evidence from ca. 1.4 Ga plutons: Geology, v. 22, no. 10, p. 901-904.

Nyman, M. W., and Karlstrom, K. E., 1997, Pluton emplacement processes and tectonic setting of the 1.42 Ga Signal batholith, SW USA: important role of crustal anisotropy during regional shortening: Precambrian Research, v. 82, no. 3-4, p. 237-263.

Paces, J. B., and Miller, J. D., 1993, Precise U-Pb ages of Duluth complex and related mafic intrusions, northeastern Minnesota: Geochronological insights to physical, petrogenetic, paleomagnetic, and tectonomagmatic processes associated with the 1.1 Ga midcontinent rift system: Journal of Geophysical Research: Solid Earth, v. 98, no. B8, p. 13997-14013.

Passchier, C., and Trouw, R., 2005, Microtectonics. 2nd: Berlin, Sopringer–Verlag.

Pearson, R. C., Hedge, C., Thomas, H., and Stern, T., 1966, Geochronology of the St. Kevin granite and neighboring Precambrian rocks, northern Sawatch Range, Colorado: Geological Society of America Bulletin, v. 77, no. 10, p. 1109-1120.

Pearson, R. C., Tweto, O., Stern, T. W., and Thomas, H. H., 1962, Age of Laramide porphyries near Leadville, Colorado: Short papers in geology and hydrology: US Geol. Survey Prof. Paper, v. 450-C.

Powell, J., 1876, Exploration of the Colorado River of the west: Washington, DC: Smithsonian Institution.

Rivers, T., 1997, Lithotectonic elements of the Grenville Province: review and tectonic implications: Precambrian Research, v. 86, no. 3-4, p. 117-154.

Rock, N. M., 1987, The nature and origin of lamprophyres: an overview: Geological Society, London, Special Publications, v. 30, no. 1, p. 191-226.

Ruleman, C. A., and Frothingham, M. G., in progress, Geologic Map of the Homestake Reservoir Quadrangle, CO.

Sears, J., Chamberlain, K., and Buckley, S., 1998, Structural and U-Pb geochronological evidence for 1.47 Ga rifting in the Belt basin, western Montana: Canadian Journal of Earth Sciences, v. 35, no. 4, p. 467-475.

Shaw, C. A., 2001, Genesis and evolution of Proterozoic crustal boundaries in the southern Rocky Mountains.

Shaw, C. A., personal communication.

Shaw, C. A., and Allen, J. L., 2007, Field rheology and structural evolution of the Homestake shear zone, Colorado: Rocky Mountain Geology, v. 42, no. 1, p. 31-56.

Shaw, C. A., Heizler, M. T., and Karlstrom, K. E., 2005, 40Ar/39Ar thermochronologic record of 1.45–1.35 Ga intracontinental tectonism in the southern Rocky Mountains: Interplay of conductive and advective heating with intracontinental deformation: The Rocky Mountain Region: An Evolving Lithosphere Tectonics, Geochemistry, and Geophysics, p. 163-184.

Shaw, C. A., Karlstrom, K. E., Williams, M. L., Jercinovic, M. J., and McCoy, A. M., 2001, Electron-microprobe monazite dating of ca. 1.71–1.63 Ga and ca. 1.45–1.38 Ga deformation in the Homestake shear zone, Colorado: Origin and early evolution of a persistent intracontinental tectonic zone: Geology, v. 29, no. 8, p. 739-742.

Silver, L., Bickford, M., Van Schmus, W., Anderson, J., Anderson, T., and Medaris Jr, L., The 1.4–1.5 by transcontinental anorogenic plutonic perforation of North America, *in* Proceedings Geological Society of America Abstracts with Programs1977, Volume 9, p. 1176-1177.

Stipp, M., Stünitz, H., Heilbronner, R., and Schmid, S. M., 2002, Dynamic recrystallization of quartz: correlation between natural and experimental conditions: Geological Society, London, Special Publications, v. 200, no. 1, p. 171-190.

Tullis, J., and Yund, R. A., 1991, Diffusion creep in feldspar aggregates: experimental evidence: Journal of Structural Geology, v. 13, no. 9, p. 987-1000.

Tweto, O., 1956, Geology of the Tennessee Pass Area, Eagle and Lake Counties, Colorado: Mineral Investigation Map MF, v. 34.

Tweto, O., 1961, Late Cenozoic events of the Leadville district and upper Arkansas Valley, Colorado: US Geological Survey Professional Paper, p. B133-B135.

Tweto, O., 1974, Geologic map and sections of the Holy Cross quadrangle, Eagle, Lake, Pitkin, and Summit counties, Colorado, US Geological Survey.

Tweto, O., 1975, Laramide (late Cretaceous-early Tertiary) orogeny in the southern Rocky Mountains: Geological Society of America Memoirs, v. 144, p. 1-44.

Tweto, O., 1979, The Rio Grande rift system in Colorado: Rio Grande Rift: Tectonics and Magmatism, p. 33-56.

Tweto, O., Moench, R., and Reed Jr, J., 1978, Geologic map of the Leadville 1 degree by 2 degrees Quadrangle, northwestern Colorado.

Tweto, O., and Sims, P., 1963, Precambrian ancestry of the Colorado mineral belt: Geological Society of America Bulletin, v. 74, no. 8, p. 991-1014.

U.S.G.S., 2016, USGS US Topo 7.5-minute map for Homestake Reservoir, CO.

Van Schmus, W., Schneider, D., Holm, D., Dodson, S., and Nelson, B., 2007, New insights into the southern margin of the Archean–Proterozoic boundary in the north-central United States based on U–Pb, Sm–Nd, and Ar–Ar geochronology: Precambrian Research, v. 157, no. 1, p. 80-105.

Vernon, R. H., 2000, Review of Microstructural Evidence of Magmatic and Solid-State Flow: Visual Geosciences, v. 5, no. 2, p. 1-23.

Wallace, A., Blaskowski, M., and Pearson, R., 1986, Geologic map of the Holy Cross Wilderness, Eagle, Pitkin, and Lake counties, Colorado.

Wallace, A. R., Lee, G. K., Campbell, D. L., Lundby, W., and Brown, S. D., 1989, Mineral resources of the Holy Cross Wilderness Area, Eagle, Pitkin, and Lake counties, Colorado, 1879.

Wark, D. A., and Watson, E. B., 2006, TitaniQ: a titanium-in-quartz geothermometer: Contributions to Mineralogy and Petrology, v. 152, no. 6, p. 743-754.

Whitmeyer, S. J., and Karlstrom, K. E., 2007, Tectonic model for the Proterozoic growth of North America: Geosphere, v. 3, no. 4, p. 220-259.

Winston, D., and Link, P., 1993, Middle Proterozoic rocks of Montana, Idaho and eastern Washington: The Belt Supergroup: Precambrian: Conterminous US, v. 100, p. 487-517.

APPENDICES

APPENDIX A

GEOLOGIC UNITS IN THE HOMESTAKE RESERVOIR QUADRANGLE

GEOLOGIC UNITS IN THE HOMESTAKE RESERVOIR QUADRANGLE

Bedrock geologic units are described by field observations and laboratory analysis from this study as well as from previous mapping and research (Allen et al., 2002; Lee et al., 2012; Shaw et al., 2001; Tweto, 1974). Each geologic unit represents the majority of its constituent lithologies outcropping in the Homestake Reservoir quadrangle, and are subdivided when possible (ex. *Xhc Group*). Geologic contacts between Proterozoic units are approximated, due to their highly mixed nature. Quaternary deposits are left blank for this study, and will be included in further mapping by (Ruleman and Frothingham, in progress).

Description of Map Units

Tlb — Latite Breccia (Oligocene)

The latite breccia unit consists of highly altered latite and quartz latite porphyries containing brecciated Proterozoic host rock. Latite breccia occurs in a single small body hosted with sharp contacts within biotite gneiss and schist, St. Kevin batholith, and mixed rock by Timberline Lake in the southwest part of the quadrangle in structural domain IV (Figure 16) (Tweto, 1974).

Tl — Lincoln Porphyry (Paleocene)

The lincoln porphyry unit is a light gray to light bluish-gray quartz monzonite porphyry. Lincoln porphyry occurs in a single, small body with sharp contacts within St. Kevin batholith, north of Turquoise lake in structural domain IV (Figure 16) (Tweto, 1974).

Kg — Granodiorite (Upper Cretaceous)

The granodiorite unit is a fine to medium-grained gray biotite hornblende granodiorite. Granodiorite intrudes biotite gneiss and schist, impure quartzite, and St. Kevin batholith with sharp contacts. Granodiorite is distinguished from St. Kevin batholith by the relative lack of muscovite. Granodiorite occurs in a small stock at West Tennessee Lakes in the center of the quadrangle at the boundaries between structural domains I, II, and III (Figure 16).

Ypst — Pseudotachylyte Shear Zone (Mesoproterozoic)

Pseudotachylyte shear zones contain black to dark gray veins of amorphous fault rock (Figure 34). Pseudotachylyte contains rapidly quenched disequilibrium melt and hosts clasts of wall rock. Pseudotachylyte occurs mainly as veins parallel to the fault plane and as minor injection veins at an oblique angle to the fault plane (Allen et al., 2002). Pseudotachylyte is hosted by biotite gneiss and schist, impure quartzite, and St. Kevin batholith. Pseudotachylyte is formed during brittle, high-temperature, and high strain rate seismic slip (Allen et al., 2002).

Pseudotachylyte both crosscuts and is crosscut in places by ultramylonite, suggesting coeval deformation (Allen and Shaw, 2013; Shaw and Allen, 2007). Electron microprobe U-Th-Pb monazite recrystallization ages on approximately coeval ultramylonite suggests deformation ca. 1380 Ma (Shaw et al., 2001). Exposed in the SLSZ in structural domain III, St. Kevin batholith east of Homestake Reservoir in structural domain II, and north of the Homestake Reservoir quadrangle in the HSZ in structural domain I (Figure 16).

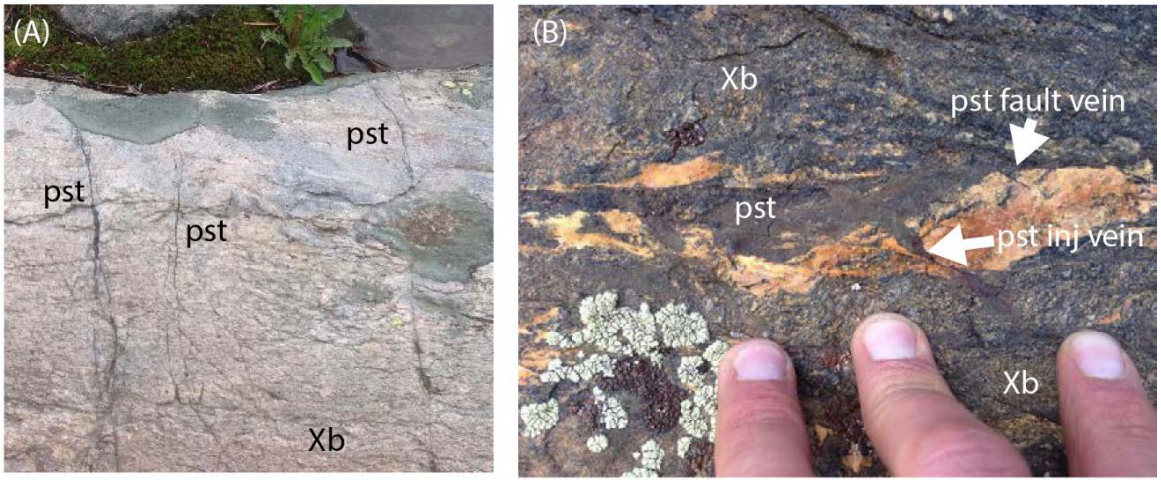

Figure 34. Pseudotachylyte. (A) Recrystallized pseudotachylite (pst) fault veins in biotite gneiss and schist host along the East Fork Homestake Creek in structural domain II, width of view is 50 cm. (B) Recrystallized pseudotachylyte fault vein and oblique injection vein in biotite gneiss and schist host in the SLSZ just below Homestake Peak in structural domain III.

Ymyl — Mylonite Shear Zone (Mesoproterozoic)

Fine-grained tectonite characterized by a strongly foliated and lineated fabric with fine-grained matrix and sheared porphyroclasts occurring in discrete shear zones (Figure 35). Mylonitic fabrics show evidence for grain size reduction, porphyroblast and

porphyroclast rotation, and mineral or aggregate elongation. Mylonitic foliations often trend subparallel to host rock foliations.

Mylonite is hosted by biotite gneiss and schist, hornblende gneiss, impure quartzite, and along margins of metalamprophyre dikes in places.Mylonite both crosscuts and is crosscut in places by pseudotachylyte and ultramylonite. Electron microprobe U-Th-Pb monazite recrystallization ages of shear fabrics suggests deformation ca. 1420-1380 ma (Shaw et al., 2001). Mylonite is exposed in the SLSZ in structural domain III, north of the Homestake Reservoir quadrangle in the HSZ in structural domain I, and in rare unmapped local occurrences in structural domain II (Figure 16).

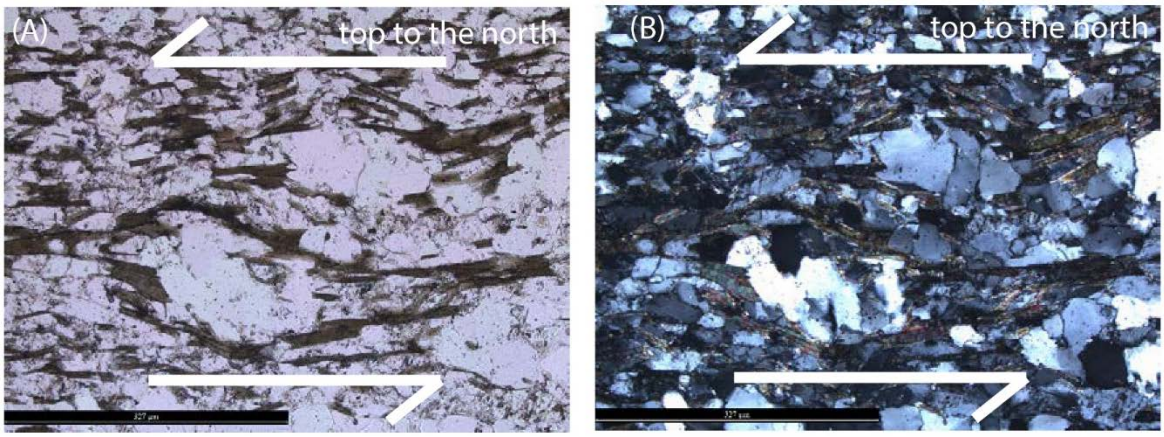

Figure 35. Mylonitic fabric. Top to the north sense of shear of quartz sigma porphyroclasts, undulose extinction across quartz subgrains, and deflected biotite foliations in the Slide Lake Shear Zone in structural domain III with 327 µm scale bar, (A) PPL, (B) XPL.

Ygs — St Kevin Batholith (Mesoproterozoic)

The St. Kevin batholith consists of gray to light pink, biotite muscovite granite to granodiorite with lesser amounts of quartz monzonite (Figure 36). Granite to granodiorite is fine to coarse-grained with euhedral microcline up to 3 cm long in places. Euhedral

mineral alignment and relict foliations are subparallel to preexisting foliations in host rocks.

Outcrop-scale contacts show sharp truncations of preexisting foliations. Map-scale contacts interfinger with host rock and pendants, leading to highly mixed border and contact zones. Pendants and xenoliths of Paleoproterozoic country rocks and Mesoproterozoic metalamprophyres are hosted within the batholith.

Quartz grains in granite to granodiorite often show subgrains with undulose extinction. Feldspar grains show minor subgrain development in places. Granite to granodiorite is deformed by pseudotachylyte on the ridge east of Homestake Reservoir. 1-10 cm thick granitic dike intruding into metalamprophyres show ductile deformation related to HSZ and SLSZ. U-Pb zircon ages suggest emplacement ca. 1425 ±12 Ma (Moscati, personal communication).

Strikes and dips on map reflect magmatic foliations of the batholith itself or metamorphic foliations in pendants of host rock. Granite to granodiorite occurs throughout quadrangle, predominantly in structural domain IV (Figure 16).

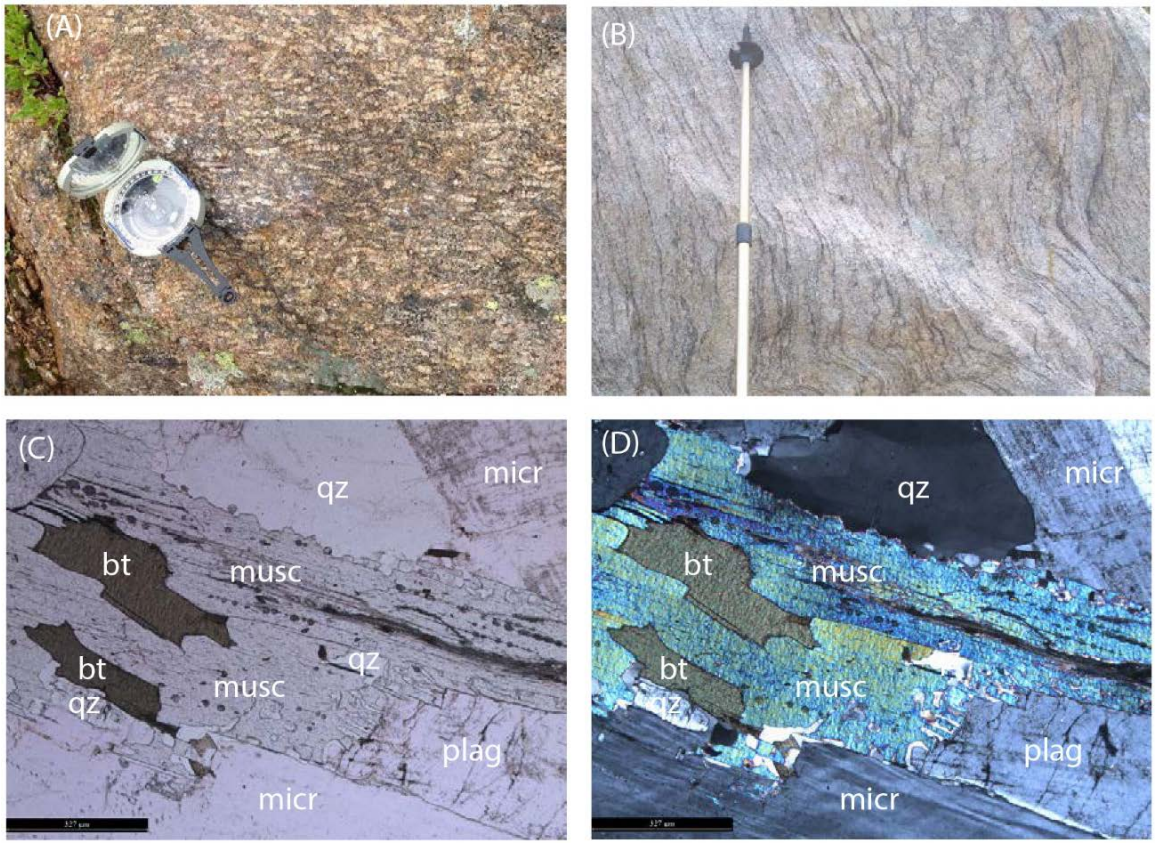

Figure 36. St Kevin batholith. (A) Euhedral microcline mineral foliations near Galena Lake in structural domain IV, compass for scale. (B) Biotite-rich foliations looking west on ridge between Homestake Reservoir and East Fork Homestake Creek in northern structural domain IV, hiking pole for scale. Photomicrographs of granite in the St. Kevin batholith containing biotite, muscovite, microcline, plagioclase, and undulose extinction in quartz with 327 µm scale bar, (C) PPL and (D) XPL.

Yml — Metalamprophyre (Mesoproterozoic)

Metalamprophyres are dark gray, black, to green, fine to medium-grained, porphyritic biotite hornblende dikes (Figure 37). Phenocrysts include biotite and hornblende aggregates. Groundmass includes k-feldspar, plagioclase, biotite, hornblende, quartz, and opaques in places.

Metalamprophyres are foliated and lineated in places. Foliations are defined by biotite grain preferred orientation and mineral segregation. Foliations near contacts are

closely spaced, less than 1 mm apart, and are parallel to contacts. Foliations in center of dikes are moderately spaced between 1-5 mm apart and show oblique orientations to foliations near contacts. Lineations are defined by elongated minerals or aggregates of biotite and hornblende. Lineation vary throughout quadrangle, but are subparallel to mylonite lineations when proximal.

Metalamprophyres exclusively intrude into Paleoproterozoic country rock. Metalamprophyres are truncated by and hosted as pendants within the younger St. Kevin batholith. Sheared foliations suggest ductile deformation post emplacement related to HSZ and SLSZ. Xenoliths of Paleoproterozoic host rocks and 1-10 cm thick granitic intrusions related to the St. Kevin granite are also deformed with the dike.

Whole-rock biotite K-Ar ages calculate emplacement ca. 1320 ± 66 ma (Pearson et al., 1966), although field relations suggest emplacement prior to the St. Kevin batholith ca. 1425 ±12 Ma (Moscati, personal communication).

10 cm to 5 m-thick dikes are generally vertical and trend east to west, approximately following Proterozoic host foliations. Dikes occur throughout the quadrangle, predominantly in structural domain II (Figure 16). Metalamprophyres are mapped as solid lines where in situ as original intrusion and as dashed lines where encapsulated as pendants in younger St. Kevin batholith and mixed rock.

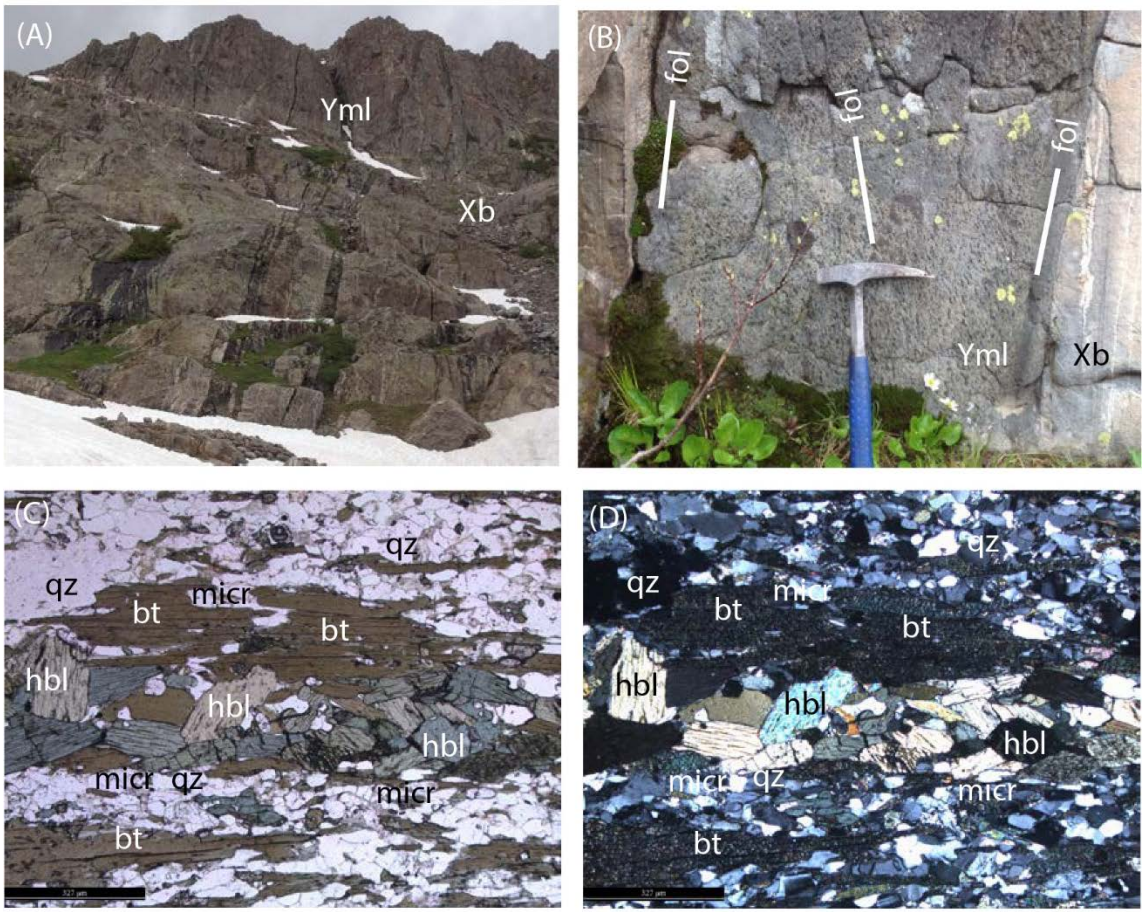

Figure 37. Metalamprophyre dikes. (A) Metalamprophyre dikes (Yml), 1-4 m wide, weathering faster than the biotite gneiss and schist host rock (Xb), looking west near Lake Esther in Domain II. (B) Metalamprophyre dike with varied foliation orientations, looking west near Lake Esther in Domain II, hammer for scale. (C) Photomicrographs of metalamprophyre showing elongated mineral aggregates of biotite and hornblende in quartz, microcline, and minor plagioclase matrix with 327 µm scale bar, (C) PPL and (D) XPL.

Yhd — Hornblende Diorite (Mesoproterozoic)

The hornblende diorite unit consists of gray, dark gray, to green, medium-grained hornblende diorite (Figure 38). Hornblende diorite is distinguishable from metalamprophyres by lighter color, more abundant and coarser plagioclase, and lack of strong foliations or lineations.

Hornblende diorite truncates Paleoproterozoic host rock foliations. Hornblende diorite is intruded by metalamprophyres and St. Kevin batholith in places. Hornblende diorite occurs in elongate pod on the East Fork of Homestake Creek and in scattered dikes by Homestake Reservoir in structural domain II, Upper Homestake Lake in structural domain IV, and Slide Lake in structural domain III (Figure 16). Hornblende diorite dike are mapped as solid lines where in situ as original intrusion and as dashed lines where hosted as pendants in younger St. Kevin batholith and mixed rock.

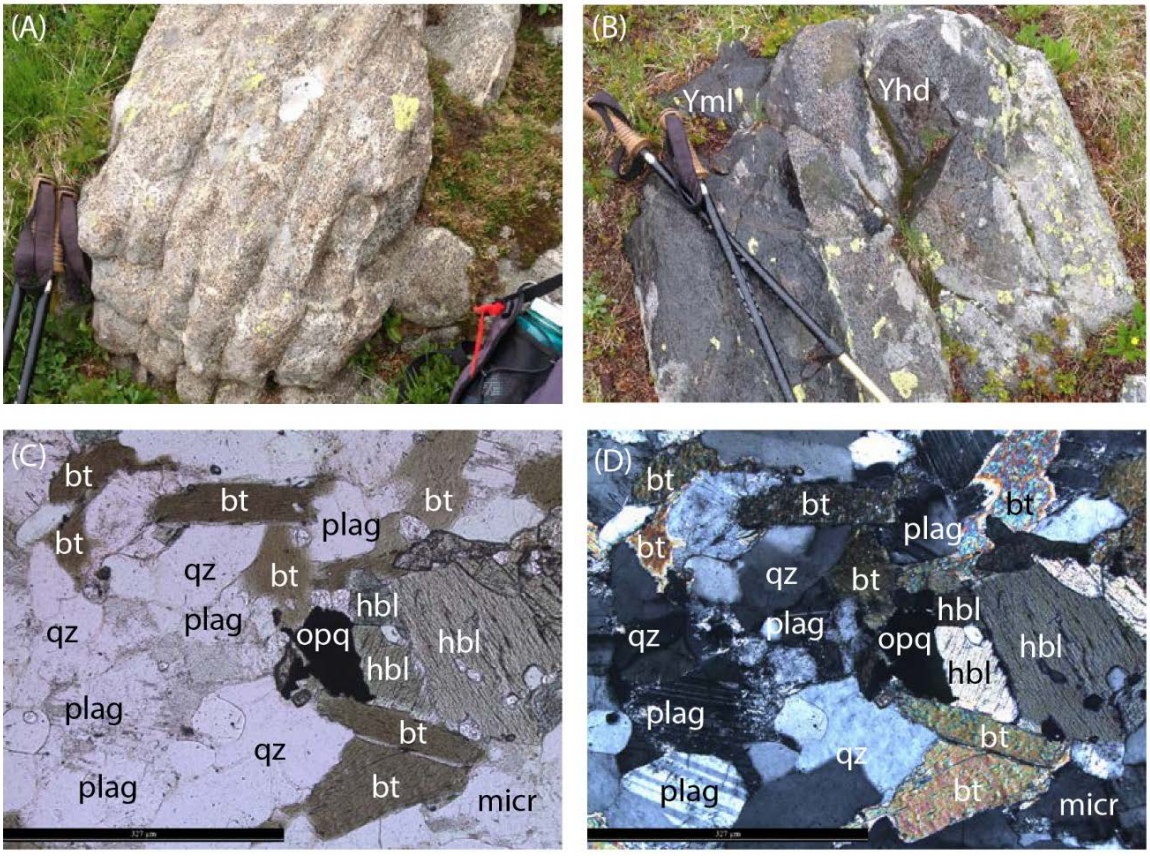

Figure 38. Hornblende diorite. (A) Hornblende diorite with preferred weathering along minor foliation planes, near Upper Homestake Lake in structural domain IV, hiking poles for scale. (B) Contact between older hornblende diorite and younger metalamprophyre near Glacier Creek in southwest structural domain IV, hiking poles for scale. Photomicrographs of hornblende diorite showing hornblende, biotite, plagioclase, quartz, and minor microcline with 327 µm scale bar, (C) PPL and (D) XPL.

XYp — Pegmatite (Paleoproterozoic to Mesoproterozoic)

The pegmatite unit consists of white to pink, coarse to very coarse-grained pegmatite as well as minor, white to pink, medium to coarse-grained aplite (Figure 39).

Deformed Paleoproterozoic occurrences intrude Paleoproterozoic gneiss and schist, contribute to migmatitic textures, and are associated with the Cross Creek Granite found immediately north of the Homestake Reservoir quadrangle (Shaw et al., 2001). Less deformed Mesoproterozoic occurrences contribute to structurally chaotic, mixed rock in center of the Homestake Reservoir quadrangle, and are associated with the St. Kevin batholith (Tweto, 1974; Tweto and Sims, 1963). Pegmatite and aplite are deformed within the HSZ and SLSZ (Allen et al., 2002; Lee et al., 2012; Shaw et al., 2001). Pegmatite and aplite occur throughout quadrangle as multiple generations of intrusion in structural domains I, II, III, and IV (Figure 16).

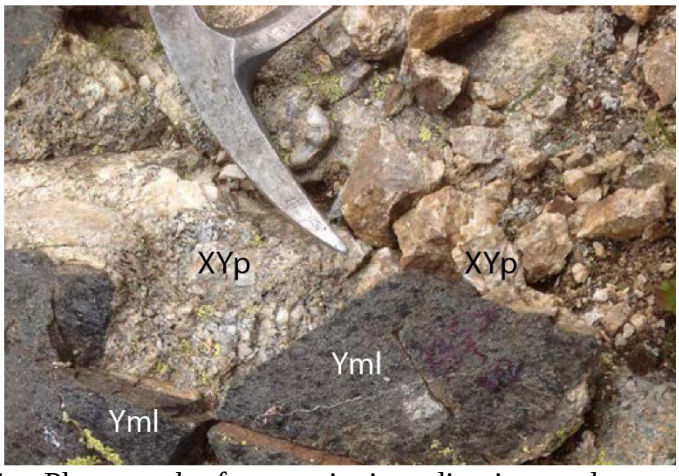

Figure 39. Pegmatite. Photograph of pegmatite intruding into and truncating a metalamprophyre dike, hammer for scale.

XYmr — Mixed Rock (Paleoproterozoic and Mesoproterozoic)

Mixed rock is a generalized map unit where Paleoproterozoic country rock of biotite gneiss and schist, hornblende gneiss, impure quartzite, and impure marble are profusely intruded by Mesoproterozoic St. Kevin batholith, Pegmatite, and other related intrusions. Mixed rock igneous intrusions crosscut preexisting metamorphic foliations, contributing to agmatitic textures.

Mixed rock occurs throughout the quadrangle along the structurally chaotic boundaries between Paleoproterozoic host rocks and Mesoproterozoic intrusives. Mixed rock is classified and mapped by geospatial statistics where there is a high degree of mixing between host rock and intrusives and where contacts on outcrop-scale and map-scale are mixed and gradational.

Xg — Unclassified Granite (Paleoproterozoic)

Unclassified granite is a pink to gray, medium-grained, biotite granite (Figure 40). Granite contains quartz with subgrain development, microcline, plagioclase, biotite, and minor opaques. Unclassified granite lacks primary muscovite, distinguishing it from St. Kevin granite.

Unclassified granite is intruded by metalamprophyres. Unclassified granite occurs in small body west of Homestake Reservoir along the northern boundary of biotite gneiss and schist and hornblende gneiss in structural domain II (Figure 16).

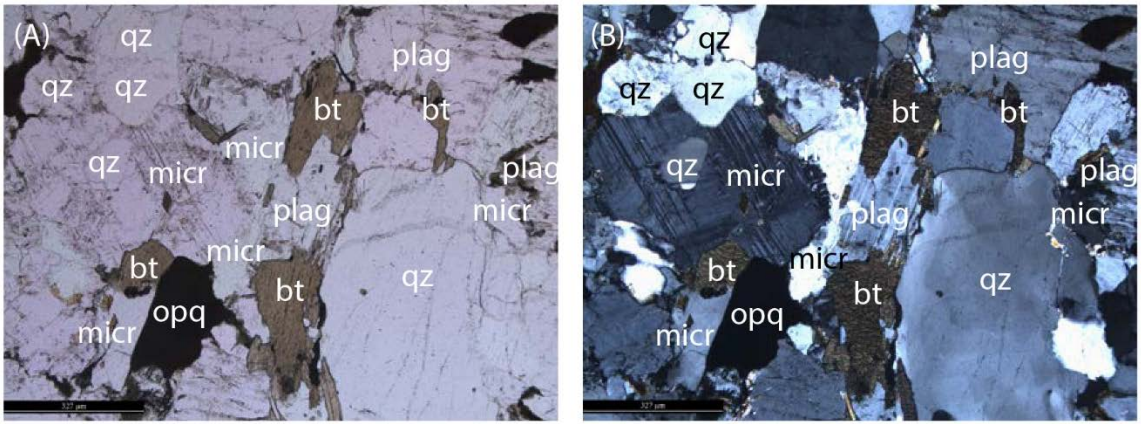

Figure 40. Unclassified Granite. Photomicrograph of Unclassified Granite showing quartz, biotite, microcline, plagioclase, opaques, and rare muscovite (not shown) near Lake Esther in structural domain II with 327 µm scale bar, (C) PPL and (D) XPL.

Xb — Biotite Gneiss and Schist (Paleoproterozoic)

Biotite gneiss and schist consist of gray to dark gray, biotite-rich quartzofeldspathic gneiss (Figure 41). Fabrics vary from less than 1 mm schistose foliations with aligned biotite grains in biotite schist to 1-10 cm gneissic foliations with mineral segregation in biotite gneiss. Gneissic foliations between leucosomes and melanosomes show 1-10 mm-thick biotite selvages in places. Foliations include low angle, recumbent nappe-style folds and upright, isoclinal folds (Shaw et al., 2001).

Quartz grains contain serrated grain boundaries in places, indicative of high-temperature grain boundary migration >500 ºC (Stipp et al., 2002). 1-5 cm felsic augens are present along foliation planes in places. Sillimanite is commonly present throughout the gneiss and schist, while garnet and cordierite are present in rare, isolated occurrences (Shaw et al., 2001; Tweto, 1974; Tweto and Sims, 1963). Biotite gneiss and schist is intruded by metalamprophyres and St. Kevin batholith, and deformed by HSZ and SLSZ along preexisting foliations (Allen and Shaw, 2013; Lee et al., 2012). U-Th-Pb monazite

recrystallization ages suggest two stages of deformation ca. 1710-1630 Ma and ca. 1420-1380 Ma (Shaw et al., 2001).

Biotite gneiss and schist is interlayered with hornblende gneiss, impure quartzite, and impure marble. Biotite gneiss and schist is included as mixed rock host constituent. Biotite gneiss and schist occur throughout the Homestake Reservoir quadrangle, predominantly in structural domains I, II, and III (Figure 16).

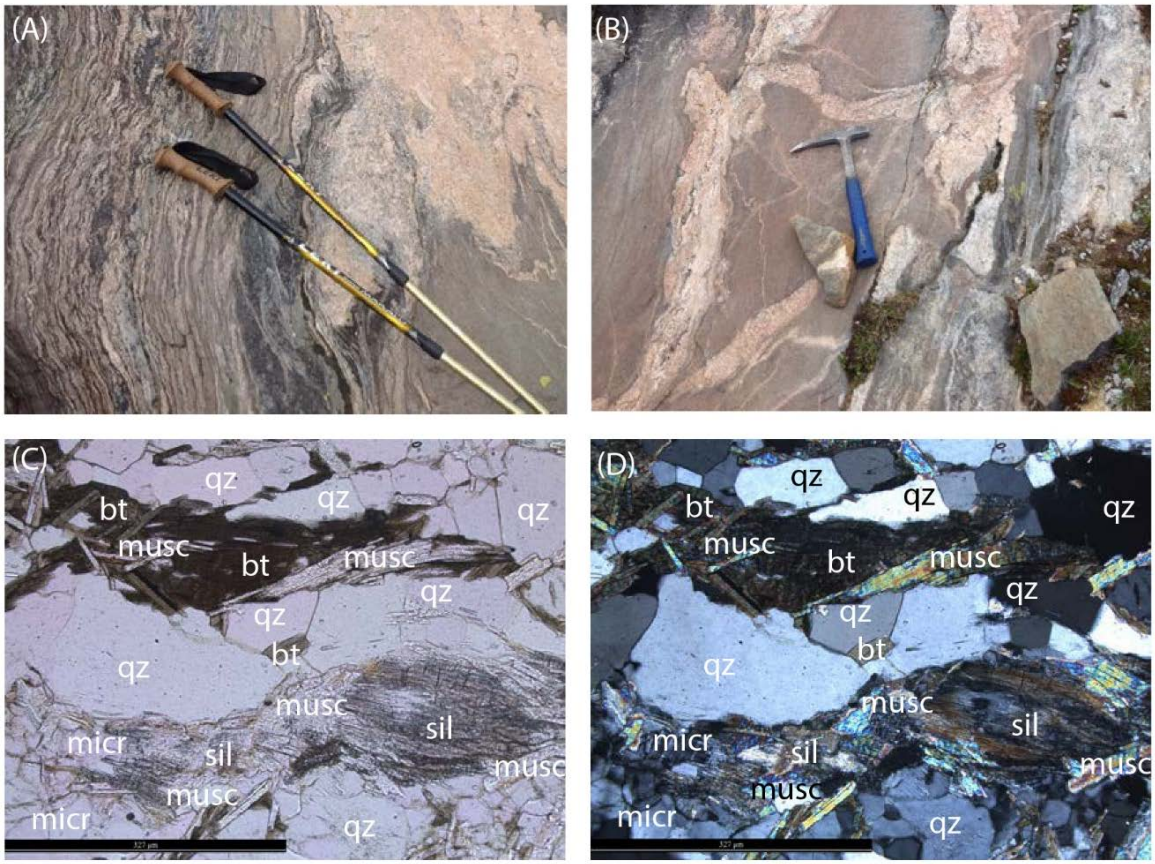

Figure 41. Biotite gneiss and schist. (A,B) Biotite gneiss and schist outcrop with deformed compositional banding and leucosomes near Bench Lakes in northwestern structural domain IV, hiking poles and hammer for scale. Photomicrograph of biotite gneiss and schist showing compositional banding, biotite and muscovite foliations, recrystallized quartz grains, microcline, and sillimanite in structural domain II with 327 µm scale bar, (C) PPL and (D) XPL.

Xhc Group — Hornblende and Calc-
Silicate Gneiss Group (Paleoproterozoic)

Includes many varieties of interlayered calc-silicate and biotite-poor rocks; impure quartzite, hornblende gneiss, impure marble, and minor amphibolite. Highly interlayered with biotite gneiss and schist (Tweto, 1974; Tweto and Sims, 1963). Contains equivalent recumbent and upright isoclinal folds as biotite gneiss and schist described above. Highly intruded by St. Kevin batholith and included as host rock constituent in mixed rock. Deformed locally by shear zone splays related to the HSZ and SLSZ. Occurs as east/west and northeast/southwest trending zone across northern part of quadrangle in structural domain II and in isolated mapped and unmapped pods (Figure 16). Subdivided into the map units described below, reflecting the locally dominant constituent among the highly interlayered units.

Xhcq — Impure Quartzite (Paleoproterozoic). The impure quartzite unit consists of gray to green, fine to medium-grained quartz-rich gneiss (Figure 42). Quartz-rich gneiss is a nearly pure quartzite in places, but often contains biotite, feldspar, and hornblende, contributing to compositional foliations. Relatively pure quartzite pods in places vary in thickness from 10 cm to 10 m.

Quartz grains often display undulose extinction and serrated grain boundaries. Quartz-rich gneiss contains mylonite and pseudotachylyte tectonites in places associated with HSZ and SLSZ in structural domain II (Figure 16). Quartz-rich gneiss is the most common unit of the Xhc group.

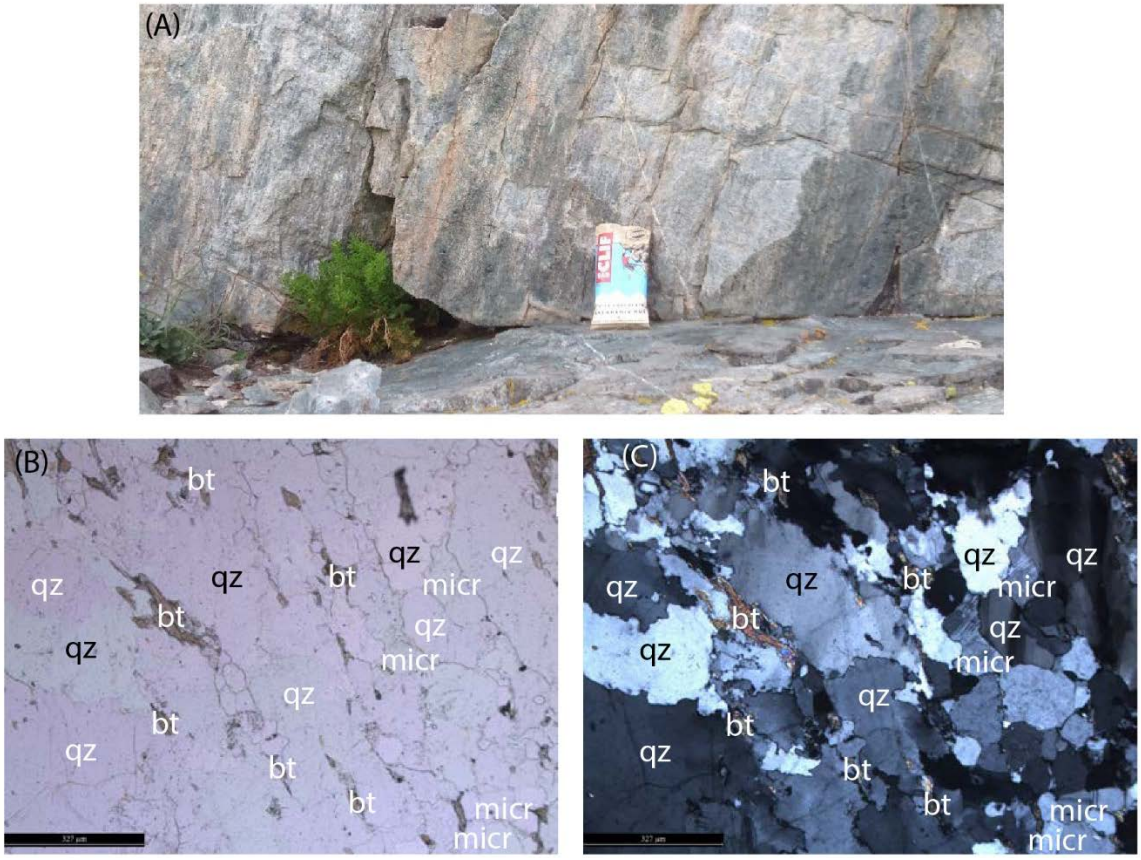

Figure 42. Impure quartzite. (A) Impure quartzite outcrop near East Fork Homestake Creek in southern structural domain II, candy bar for scale. Photomicrograph of impure quartzite showing undulose extinction in quartz subgrains, irregular quartz grain boundaries due to grain boundary migration recrystallization, and biotite and microcline impurities with 327 µm scale bar, (B) PPL and (C) XPL.

Xhch — Hornblende Gneiss (Paleoproterozoic). Hornblende gneiss is a dark gray to black hornblende-rich quartzofeldspathic gneiss (Figure 43). Foliations are usually less than 1 cm apart and are represented by approximately 75% hornblende-rich melanosomes, and 25% leucosomes with quartz, plagioclase, and minor microcline. Isolated lenses 10 cm to 1 m thick contain dense concentrations of hornblende and clinopyroxene (not shown in photomicrographs).

Hornblende gneiss layers are rarely more than 1 to 2 m thick without abundant interlayers of biotite gneiss and schist or other Xhc group. Distinct compositional layers with a lesser abundance of biotite distinguish hornblende gneiss from biotite gneiss and biotite schist. Hornblende gneiss is deformed by mylonite fabrics and pseudotachylyte in places associated with HSZ and SLSZ in structural domain II (Figure 16).

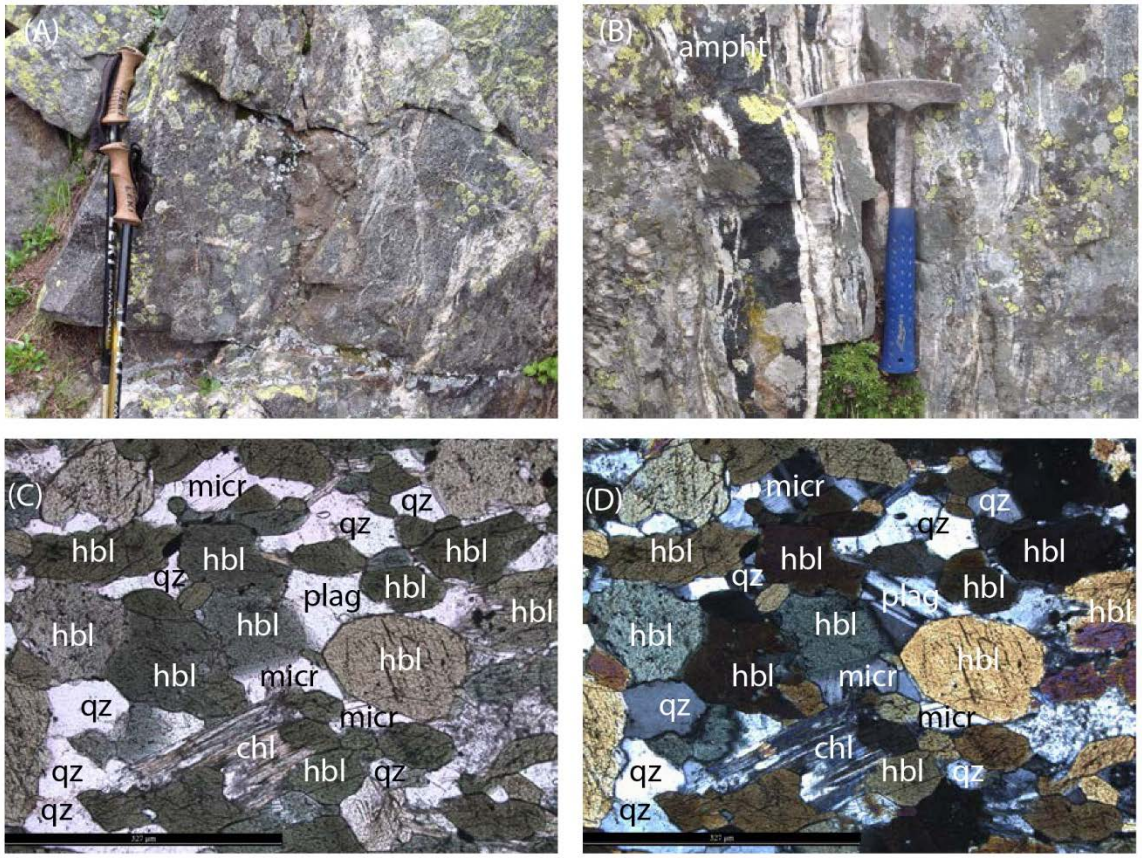

Figure 43. Hornblende gneiss. (A) Hornblende gneiss outcrop looking perpendicular to foliation near East Fork Homestake Creek in structural domain II, hiking poles for scale. (B) Amphibolite melanosome, 10 cm wide, and feldspar leucosomes, 1 cm wide, in biotite gneiss and schist, hammer for scale. Photomicrograph of hornblende gneiss showing hornblende, quartz, plagioclase, microcline, and chlorite in Domain II with 327 µm scale bar, (C) PPL and (D) XPL.

Xhcm — Impure Marble (Paleoproterozoic). The impure marble consists of gray, white, to blue-green, calc-silicate gneiss (Figure 44). Calc-silicate gneiss is nearly pure marble in places, but often includes biotite, quartz, feldspar, hornblende, clinopyroxene, and chlorite. Calc-silicate gneiss is distinguished in the field by high degree of hackly weathering and moderate effervescence with HCL. Calc-silicate gneiss lenses are rarely more than 1 m thick without abundant interlayers of biotite gneiss and schist or other Xhc group. Calc-silicate gneiss occurs as small, isolated pods in structural domain II and poor exposure prevents accurately mapping lateral continuity of Calc-silicate gneiss (Figure 16).

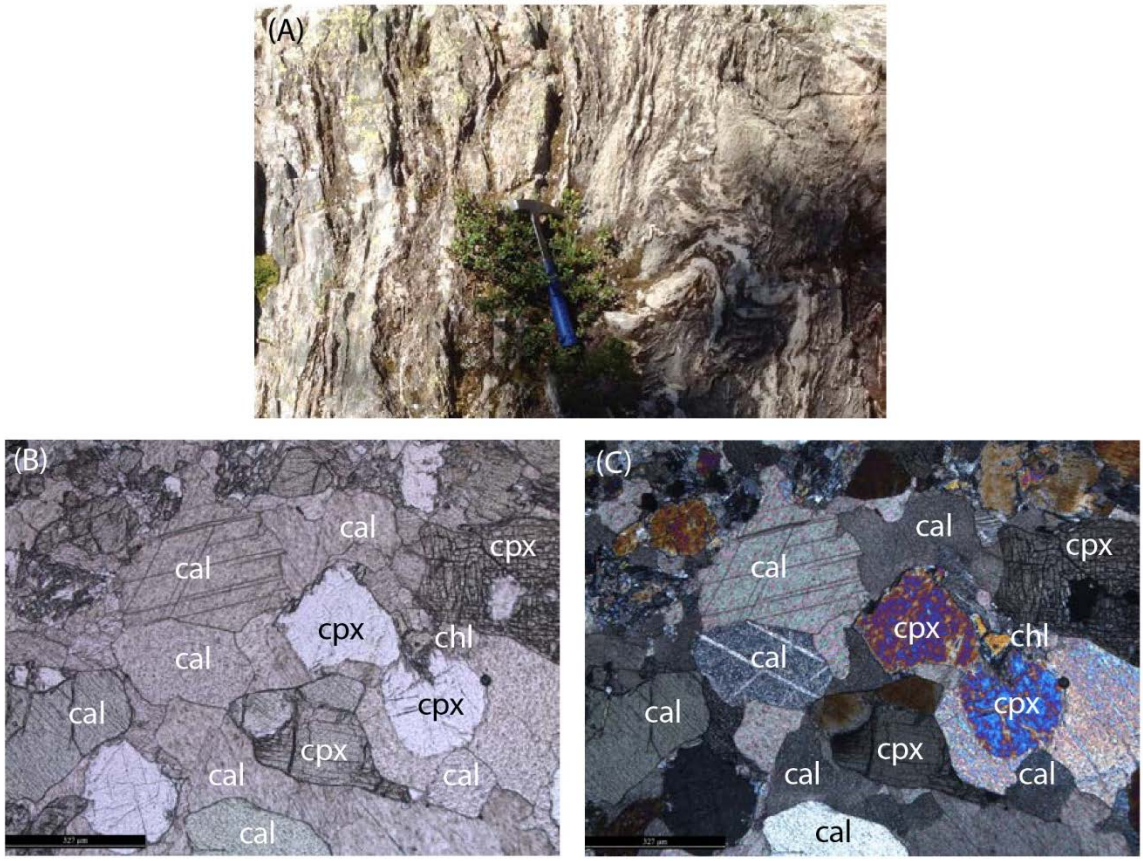

Figure 44. Impure marble. (A) Impure marble showing deformed foliations and hackly weathering, rock hammer for scale. Photomicrograph of impure marble showing twinned calcite plus clinopyroxene and chlorite in structural domain II with 327 µm scale bar, (B) PPL and (C) XPL.

APPENDIX B

FOLIATIONS

ID	Easting	Northing	Strike	Dip	Rock Type
272601201	371019	4355137	226	65	Xb
272601204	370919	4355175	123	55	Xb
272601205	370891	4355184	100	50	Xb
272601206	370781	4355264	136	25	Xb
272601207	371261	4356212	260	50	Xb
272601208	371262	4356265	220	75	Xb
272601213	373054	4356002	95	75	Xb
280101304	377976	4358833	15	80	Xb
280101409	375463	4359381	195	85	Xb
280701515	377148	4357884	65	55	Xb
280901802	376713	4358903	350	70	Xb
281001901	378815	4355050	355	60	Xb
281302003	377009	4359404	165	90	Xb
281302004	377111	4359247	140	90	Xb
281302005	377114	4359203	140	90	Xb
281302009	377066	4359074	147	75	Xb
281302010	377062	4359051	133	87	Xb
281302015	376949	4358863	285	85	Xb
281302102	375415	4358671	297	85	Xb
281402201	379585	4359298	267	74	Xb
281402202	379486	4359923	0	0	Xb
281402203	379402	4359454	261	79	Xb
281402204	379264	4359447	265	90	Xb
7261602304	372098	4358577	243	82	Xb
7261603204	371310	4357036	238	72	Xb
7271603301	371297	4356657	97	71	Xb
7271603404	370787	4356782	259	57	Xb
7271603501	370741	4356829	90	65	Xb
7271603502	370741	4356829	58	80	Xb
7271603601	370672	4356954	58	81	Xb
7271603706	370840	4356824	246	72	Xb
7271603708	371336	4356913	275	62	Xb
7271603710	371499	4356810	272	85	Xb
7271603714	371773	4356718	269	56	Xb
7271603715	372148	4356806	179	61	Xb
7271603801	372118	4356980	247	84	Xb
7271603803	371804	4356922	270	64	Xb
7281604101	374741	4357702	256	82	Xb
7291604303	374483	4357597	287	78	Xb
7291604408	374014	4356028	248	32	Xb
7291604410	374050	4355750	293	27	Xb
7291604502	374334	4355617	40	11	Xb
7291604503	374383	4355494	69	9	Xb

7291604504	374699	4354126	91	50	Xb
8021604903	372098	4346488	306	22	Xb
8031605001	375032	4349399	224	49	Xb
8031605002	374440	4349597	316	79	Xb
8031605101	374446	4349731	197	88	Xb
8031605201	372609	4351012	165	38	Xb
8031605202	372550	4351200	141	38	Xb
8031605301	372471	4351643	183	80	Xb
8031605406	374211	4347449	252	54	Xb
8071605801	377356	4355621	14	57	Xb
8071605805	376778	4355725	259	64	Xb
8071605806	376791	4355813	269	57	Xb
8071605904	376706	4356106	260	48	Xb
8071605905	376720	4356198	231	62	Xb
8071606003	376789	4356475	318	78	Xb
8071606104	376811	4356564	306	84	Xb
8071606106	377067	4356721	243	67	Xb
8071606107	377127	4356636	280	70	Xb
8091606301	377781	4357104	281	45	Xb
8091606302	377781	4357104	272	68	Xb
8091606503	378071	4357669	248	45	Xb
8151606701	380059	4358862	263	47	Xb
8151606803	379075	4359055	308	30	Xb
8151606804	379902	4359340	281	23	Xb
8151606903	361573	4356248	225	88	Xb
8161607001	368637	4358528	44	70	Xb
8161607301	369422	4357947	90	17	Xb
6090581	374624	4357965	281	83	Xb
6090583	374521	4357871	281	85	Xb
6090584	374493	4357808	289	90	Xb
6090604	374779	4358604	136	90	Xb
6090606	374849	4358726	139	76	Xb
6090607	374640	4358924	337	86	Xb
61206301	375251	4348356	273	55	Xb
61206302	375266	4348341	259	34	Xb
6160721	374582	4357786	104	79	Xb
6160725	374237	4357680	110	74	Xb
6160726	374205	4357630	88	90	Xb
6160731	374204	4357176	241	85	Xb
6160733	374164	4356855	282	81	Xb
6160735	374284	4356984	252	74	Xb
6170741	375084	4358726	127	90	Xb
6170742	375141	4358977	129	84	Xb
6170743	375214	4358830	131	76	Xb

6170744	375295	4358659	161	85	Xb
6170746	375346	4358316	152	86	Xb
6170747	375331	4357821	277	81	Xb
6170748	375289	4357614	85	77	Xb
61707409	375211	4357528	115	87	Xb
62408101	374150	4357972	270	90	Xb
62508501	374322	4357537	290	90	Xb
62508502	374276	4357499	270	85	Xb
62508506	374170	4357376	289	85	Xb
62508602	374163	4357206	75	75	Xb
62508604	374102	4356969	75	85	Xb
62508701	374069	4357080	260	65	Xb
62508702	374056	4357086	78	80	Xb
62508703	374074	4357023	61	90	Xb
70110501	377567	4356723	265	75	Xb
70110503	377211	4356649	285	85	Xb
70110504	377145	4356648	280	65	Xb
70110702	377373	4357067	245	90	Xb
70210701	377670	4356955	270	75	Xb
70210702	377740	4357094	235	75	Xb
70210801	377561	4357491	330	60	Xb
70210807	377917	4357695	280	20	Xb
70210901	377961	4357711	70	55	Xb
70210903	378126	4357696	325	50	Xb
70311001	375261	4348328	235	45	Xb
70911401	371519	4359286	90	60	Xb
70911402	372109	4358848	100	85	Xb
71011401	372006	4358808	60	85	Xb
71011402	371930	4358866	145	70	Xb
71011403	371940	4358853	75	55	Xb
71011501	371750	4358673	95	80	Xb
71011502	371714	4358659	85	70	Xb
71011503	371622	4358530	85	85	Xb
71011504	371667	4358535	65	75	Xb
71011505	371639	4358234	105	80	Xb
71011601	371675	4358208	80	80	Xb
71211701	371520	4357771	60	90	Xb
71212201	370898	43557179	255	65	Xb
71312402	371653	4357738	180	90	Xb
71612601	379173	4356036	215	90	Xb
71712701	378895	4357724	200	65	Xb
71712702	378793	4357760	200	85	Xb
71712703	378752	4357781	210	85	Xb
71712705	378505	4357887	55	85	Xb

71712707	378366	4357943	240	35	Xb
71712801	378341	4357958	265	55	Xb
71712802	378204	4358089	225	55	Xb
71712806	378066	4358433	268	30	Xb
71712901	378503	4357618	260	55	Xb
71712902	378505	4357597	278	35	Xb
272000201	375144	4357782	105	85	Xb
272000206	375242	4357225	110	85	Xb
272500805	373759	4357192	275	85	Xb
272500814	373394	4357912	90	90	Xb
272601001	371855	4352945	10	90	Xb
272601101	371557	4354541	174	60	Xb
272601201	371019	4355137	226	65	Xb
272601204	370919	4355175	123	55	Xb
272601205	370891	4355184	100	50	Xb
272601206	370781	4355264	136	25	Xb
272601207	371261	4356212	260	50	Xb
272601208	371262	4356265	220	75	Xb
272601213	373054	4356002	95	75	Xb
280101304	377976	4358833	15	80	Xb
280101409	375463	4359381	195	85	Xb
280701515	377148	4357884	65	55	Xb
280901802	376713	4358903	350	70	Xb
281001901	378815	4355050	355	60	Xb
281302003	377009	4359404	165	90	Xb
281302004	377111	4359247	140	90	Xb
281302005	377114	4359203	140	90	Xb
281302009	377066	4359074	147	75	Xb
281302010	377062	4359051	133	87	Xb
281302015	376949	4358863	285	85	Xb
281302102	375415	4358671	297	85	Xb
281402201	379585	4359298	267	74	Xb
281402202	379486	4359923	0	0	Xb
281402203	379402	4359454	261	79	Xb
281402204	379264	4359447	265	90	Xb
7261602304	372098	4358577	243	82	Xb
7261603204	371310	4357036	238	72	Xb
7271603301	371297	4356657	97	71	Xb
7271603404	370787	4356782	259	57	Xb
7271603501	370741	4356829	90	65	Xb
7271603502	370741	4356829	58	80	Xb
7271603601	370672	4356954	58	81	Xb
7271603706	370840	4356824	246	72	Xb
7271603708	371336	4356913	275	62	Xb

7271603710	371499	4356810	272	85	Xb
7271603714	371773	4356718	269	56	Xb
7271603715	372148	4356806	179	61	Xb
7271603801	372118	4356980	247	84	Xb
7271603803	371804	4356922	270	64	Xb
7281604101	374741	4357702	256	82	Xb
7291604303	374483	4357597	287	78	Xb
7291604408	374014	4356028	248	32	Xb
7291604410	374050	4355750	293	27	Xb
7291604502	374334	4355617	40	11	Xb
7291604503	374383	4355494	69	9	Xb
7291604504	374699	4354126	91	50	Xb
8021604903	372098	4346488	306	22	Xb
8031605001	375032	4349399	224	49	Xb
8031605002	374440	4349597	316	79	Xb
8031605101	374446	4349731	197	88	Xb
8031605201	372609	4351012	165	38	Xb
8031605202	372550	4351200	141	38	Xb
8031605301	372471	4351643	183	80	Xb
8031605406	374211	4347449	252	54	Xb
8071605801	377356	4355621	14	57	Xb
8071605805	376778	4355725	259	64	Xb
8071605806	376791	4355813	269	57	Xb
8071605904	376706	4356106	260	48	Xb
8071605905	376720	4356198	231	62	Xb
8071606003	376789	4356475	318	78	Xb
8071606104	376811	4356564	306	84	Xb
8071606106	377067	4356721	243	67	Xb
8071606107	377127	4356636	280	70	Xb
8091606301	377781	4357104	281	45	Xb
8091606302	377781	4357104	272	68	Xb
8091606503	378071	4357669	248	45	Xb
8151606701	380059	4358862	263	47	Xb
8151606803	379075	4359055	308	30	Xb
8151606804	379902	4359340	281	23	Xb
8151606903	361573	4356248	225	88	Xb
8161607001	368637	4358528	44	70	Xb
8161607301	369422	4357947	90	17	Xb
6090587	374373	4357765	75	81	Xhc
6090591	374223	4357666	113	89	Xhc
6090592	374254	4357815	96	73	Xhc
6090593	374271	4357862	98	90	Xhc
6090595	374292	4357880	91	90	Xhc
6090597	374398	4358004	293	73	Xhc

6090598	374413	4358161	263	90	Xhc
6090601	374743	4358418	110	85	Xhc
6090602	374759	4358475	132	79	Xhc
6090603	374784	4358570	132	90	Xhc
6090605	374825	4358670	128	90	Xhc
6160722	374480	4357728	111	90	Xhc
6160723	374370	4357745	95	90	Xhc
6160724	374284	4357711	92	69	Xhc
6160732	374193	4356971	71	81	Xhc
62408201	374266	4357860	105	90	Xhc
62408203	374283	4357880	271	85	Xhc
62508504	374204	4357456	132	80	Xhc
62508505	374179	4357399	90	85	Xhc
62508601	374129	4357318	215	90	Xhc
62508603	374099	4356999	262	75	Xhc
62709501	374377	4356653	133	65	Xhc
62709802	374152	4356442	210	55	Xhc
62709803	374120	4356461	235	40	Xhc
71211902	371196	4357313	240	85	Xhc
71312401	371652	4357772	87	70	Xhc
71312405	372115	4357841	95	85	Xhc
71612605	379072	4355996	60	40	Xhc
71612606	379048	4356012	40	80	Xhc
272000205	375213	4357401	95	90	Xhc
272000207	375241	4357135	65	80	Xhc
280701511	377328	4358016	265	55	Xhc
280901707	377294	4358605	262	85	Xhc
280901708	377254	4358590	90	90	Xhc
280901711	376861	4358680	160	90	Xhc
6090587	374373	4357765	75	81	Xhc
6090591	374223	4357666	113	89	Xhc
6090592	374254	4357815	96	73	Xhc
6090593	374271	4357862	98	90	Xhc
6090595	374292	4357880	91	90	Xhc
6090597	374398	4358004	293	73	Xhc
6090598	374413	4358161	263	90	Xhc
6090601	374743	4358418	110	85	Xhc
6090602	374759	4358475	132	79	Xhc
6090603	374784	4358570	132	90	Xhc
6090605	374825	4358670	128	90	Xhc
6160722	374480	4357728	111	90	Xhc
6160723	374370	4357745	95	90	Xhc
6160724	374284	4357711	92	69	Xhc
6160732	374193	4356971	71	81	Xhc

62408201	374266	4357860	105	90	Xhc
62408203	374283	4357880	271	85	Xhc
62508504	374204	4357456	132	80	Xhc
62508505	374179	4357399	90	85	Xhc
62508601	374129	4357318	215	90	Xhc
62508603	374099	4356999	262	75	Xhc
62709501	374377	4356653	133	65	Xhc
62709802	374152	4356442	210	55	Xhc
62709803	374120	4356461	235	40	Xhc
71211902	371196	4357313	240	85	Xhc
71312401	371652	4357772	87	70	Xhc
71312405	372115	4357841	95	85	Xhc
71612605	379072	4355996	60	40	Xhc
71612606	379048	4356012	40	80	Xhc
272000205	375213	4357401	95	90	Xhc
272000207	375241	4357135	65	80	Xhc
280701511	377328	4358016	265	55	Xhc
280901707	377294	4358605	262	85	Xhc
280901708	377254	4358590	90	90	Xhc
280901711	376861	4358680	160	90	Xhc
6090594	374286	4357871	88	90	Xhca
70110502	377404	4356680	295	65	Xhca
71211906	371108	4357101	100	75	Xhca
7271603604	370572	4357009	216	49	Xhch
7271603605	370657	4356999	248	55	Xhch
7271603702	370757	4356948	69	69	Xhch
7271603705	370807	4356883	76	90	Xhch
7291604403	374126	4356671	285	71	Xhch
8071605902	376757	4355908	268	32	Xhch
8091606401	377811	4357245	230	69	Xhch
62710201	377040	4355970	275	65	Xhch
62408102	374188	4357876	90	82	Xhch
62408103	374195	4357850	90	90	Xhch
62408105	374251	4357833	275	88	Xhch
62408202	374273	4357866	95	90	Xhch
62509103	374308	4357055	75	75	Xhch
62509105	374302	4357070	98	15	Xhch
62509106	374286	4357804	255	85	Xhch
62709502	374356	4356667	200	75	Xhch
62709503	374354	4356630	200	75	Xhch
62709504	374341	4356586	200	70	Xhch
62709801	374297	4356521	190	75	Xhch
62709901	374093	4356495	120	80	Xhch
62709903	374439	4356526	215	60	Xhch

63010301	376971	4356249	86	82	Xhch
63010302	376982	4356263	260	65	Xhch
63010403	377114	4356355	245	75	Xhch
63010405	377198	4356476	250	55	Xhch
63010406	377204	4356523	270	75	Xhch
70110505	377139	4356700	225	70	Xhch
70110506	377103	4356742	250	75	Xhch
70110509	376951	4356744	260	60	Xhch
70110510	376858	4356709	245	65	Xhch
70110511	376822	4356724	245	55	Xhch
70110514	376743	4357053	290	90	Xhch
70110605	377169	4357217	265	75	Xhch
70110606	377212	4357160	240	90	Xhch
70110610	377368	4357102	60	75	Xhch
70110701	377366	4357089	65	86	Xhch
70210704	377702	4357312	240	90	Xhch
71211801	371358	4357549	119	90	Xhch
71211805	371274	4357435	85	85	Xhch
71211903	371208	4357270	275	75	Xhch
71211904	371159	4357217	240	80	Xhch
71212002	371040	4356946	250	80	Xhch
71212101	370864	4356906	90	90	Xhch
71212102	370864	4356937	75	80	Xhch
71212103	370866	4356980	70	80	Xhch
71212104	370864	4357087	60	45	Xhch
71212105	370857	4357102	260	75	Xhch
71212204	371251	4357486	70	75	Xhch
71612604	379128	4345928	240	65	Xhch
272000203	375311	4357609	100	75	Xhch
272500809	373859	4357505	305	45	Xhch
272500813	373898	4357914	70	90	Xhch
272500815	373368	4357854	95	90	Xhch
272500901	373337	4357733	240	75	Xhch
272500906	373245	4357306	255	65	Xhch
272601003	371901	4353114	10	85	Xhch
280101301	377452	4359092	15	17	Xhch
280101306	377664	4358828	307	80	Xhch
280101307	377611	4358835	340	80	Xhch
280101309	377515	4358899	140	80	Xhch
280101310	377484	4358910	170	55	Xhch
280101311	377460	4358949	327	90	Xhch
280101312	377459	4358967	185	90	Xhch
280101403	377277	4359008	110	60	Xhch
280101404	377221	4358983	350	88	Xhch

280101405	377141	4358933	290	88	Xhch
280101407	376987	4359332	190	85	Xhch
280101408	376936	4359377	110	90	Xhch
280101410	375415	4359378	165	90	Xhch
280701507	377618	4358202	323	40	Xhch
280701508	377599	4358181	325	65	Xhch
280701509	377596	4358172	338	65	Xhch
280701510	377381	4358036	310	48	Xhch
280701513	377274	4357972	0	0	Xhch
280701514	377204	4357946	65	65	Xhch
280901601	376902	4358416	268	77	Xhch
280901602	376947	4358360	125	75	Xhch
280901604	377138	4358271	45	25	Xhch
280901607	377260	4358257	320	55	Xhch
280901610	377360	4358266	330	90	Xhch
280901702	377496	4358613	350	80	Xhch
280901710	377086	4358633	80	80	Xhch
281001902	378847	4355383	350	55	Xhch
281001904	377119	4353978	230	90	Xhch
281001905	377184	4353827	105	70	Xhch
281302008	377079	4359104	130	90	Xhch
281302012	377077	4358961	110	90	Xhch
7261602706	371466	4357357	270	87	Xhch
62710201	377040	4355970	275	65	Xhch
62408102	374188	4357876	90	82	Xhch
62408103	374195	4357850	90	90	Xhch
62408105	374251	4357833	275	88	Xhch
62408202	374273	4357866	95	90	Xhch
62509103	374308	4357055	75	75	Xhch
62509105	374302	4357070	98	15	Xhch
62509106	374286	4357804	255	85	Xhch
62709502	374356	4356667	200	75	Xhch
62709503	374354	4356630	200	75	Xhch
62709504	374341	4356586	200	70	Xhch
62709801	374297	4356521	190	75	Xhch
62709901	374093	4356495	120	80	Xhch
62709903	374439	4356526	215	60	Xhch
63010301	376971	4356249	86	82	Xhch
63010302	376982	4356263	260	65	Xhch
63010403	377114	4356355	245	75	Xhch
63010405	377198	4356476	250	55	Xhch
63010406	377204	4356523	270	75	Xhch
70110505	377139	4356700	225	70	Xhch
70110506	377103	4356742	250	75	Xhch

70110509	376951	4356744	260	60	Xhch
70110510	376858	4356709	245	65	Xhch
70110511	376822	4356724	245	55	Xhch
70110514	376743	4357053	290	90	Xhch
70110605	377169	4357217	265	75	Xhch
70110606	377212	4357160	240	90	Xhch
70110610	377368	4357102	60	75	Xhch
70110701	377366	4357089	65	86	Xhch
70210704	377702	4357312	240	90	Xhch
71211801	371358	4357549	119	90	Xhch
71211805	371274	4357435	85	85	Xhch
71211903	371208	4357270	275	75	Xhch
71211904	371159	4357217	240	80	Xhch
71212002	371040	4356946	250	80	Xhch
71212101	370864	4356906	90	90	Xhch
71212102	370864	4356937	75	80	Xhch
71212103	370866	4356980	70	80	Xhch
71212104	370864	4357087	60	45	Xhch
71212105	370857	4357102	260	75	Xhch
71212204	371251	4357486	70	75	Xhch
71612604	379128	4345928	240	65	Xhch
272000203	375311	4357609	100	75	Xhch
272500809	373859	4357505	305	45	Xhch
272500813	373898	4357914	70	90	Xhch
272500815	373368	4357854	95	90	Xhch
272500901	373337	4357733	240	75	Xhch
272500906	373245	4357306	255	65	Xhch
272601003	371901	4353114	10	85	Xhch
280101301	377452	4359092	15	17	Xhch
280101306	377664	4358828	307	80	Xhch
280101307	377611	4358835	340	80	Xhch
280101309	377515	4358899	140	80	Xhch
280101310	377484	4358910	170	55	Xhch
280101311	377460	4358949	327	90	Xhch
280101312	377459	4358967	185	90	Xhch
280101403	377277	4359008	110	60	Xhch
280101404	377221	4358983	350	88	Xhch
280101405	377141	4358933	290	88	Xhch
280101407	376987	4359332	190	85	Xhch
280101408	376936	4359377	110	90	Xhch
280101410	375415	4359378	165	90	Xhch
280701507	377618	4358202	323	40	Xhch
280701508	377599	4358181	325	65	Xhch
280701509	377596	4358172	338	65	Xhch

280701510	377381	4358036	310	48	Xhch
280701513	377274	4357972	0	0	Xhch
280701514	377204	4357946	65	65	Xhch
280901601	376902	4358416	268	77	Xhch
280901602	376947	4358360	125	75	Xhch
280901604	377138	4358271	45	25	Xhch
280901607	377260	4358257	320	55	Xhch
280901610	377360	4358266	330	90	Xhch
280901702	377496	4358613	350	80	Xhch
280901710	377086	4358633	80	80	Xhch
281001902	378847	4355383	350	55	Xhch
281001904	377119	4353978	230	90	Xhch
281001905	377184	4353827	105	70	Xhch
281302008	377079	4359104	130	90	Xhch
281302012	377077	4358961	110	90	Xhch
7261602706	371466	4357357	270	87	Xhch
7271603504	370711	4356856	59	86	Xhcm
7281603801	371321	4357406	255	81	Xhcm
7291604313	374200	4357355	258	87	Xhcm
7291604315	374164	4356926	253	85	Xhcm
7291604402	374153	4356703	291	73	Xhcm
6090586	374373	4357765	89	86	Xhcm
6090588	374347	4357725	272	78	Xhcm
6160734	374175	4356930	254	76	Xhcm
6160736	374345	4357003	84	74	Xhcm
61707410	375086	4357396	253	80	Xhcm
61707411	375076	4357372	262	90	Xhcm
62408301	374369	4357619	116	80	Xhcm
62508804	374105	4356724	260	65	Xhcm
62508901	374111	4356745	260	65	Xhcm
62508905	374187	4356717	285	90	Xhcm
62508908	374207	4356803	305	80	Xhcm
62509104	374300	4357064	225	55	Xhcm
6090586	374373	4357765	89	86	Xhcm
6090588	374347	4357725	272	78	Xhcm
6160734	374175	4356930	254	76	Xhcm
6160736	374345	4357003	84	74	Xhcm
61707410	375086	4357396	253	80	Xhcm
61707411	375076	4357372	262	90	Xhcm
62408301	374369	4357619	116	80	Xhcm
62508804	374105	4356724	260	65	Xhcm
62508901	374111	4356745	260	65	Xhcm
62508905	374187	4356717	285	90	Xhcm
62508908	374207	4356803	305	80	Xhcm

62509104	374300	4357064	225	55	Xhcm
6090582	374550	4357895	290	90	Xhcq
6090585	374471	4357790	90	85	Xhcq
62508704	374086	4356929	87	80	Xhcq
62508801	374052	4356797	250	75	Xhcq
62508902	374128	4356736	270	55	Xhcq
62508903	374174	4356726	310	80	Xhcq
62508904	3374184	4356734	260	75	Xhcq
62508906	374219	4356769	140	70	Xhcq
62508907	374206	4356794	310	80	Xhcq
62508909	374237	4356840	290	86	Xhcq
62508910	374219	4356864	285	85	Xhcq
62509001	374239	4356865	285	85	Xhcq
62509002	374248	4356884	300	85	Xhcq
62509101	374292	4356978	160	65	Xhcq
62509102	374316	4357009	70	85	Xhcq
62709804	374114	4356511	272	75	Xhcq
62709902	374402	4356446	225	55	Xhcq
63010401	376994	4356270	250	85	Xhcq
63010402	377016	4356310	95	75	Xhcq
63010404	377160	4356385	265	85	Xhcq
63010407	377205	4356557	245	55	Xhcq
70110507	377045	4356756	280	75	Xhcq
70110508	376986	4356747	260	80	Xhcq
70110512	376808	4356754	245	70	Xhcq
70110513	376793	4356792	265	85	Xhcq
70110515	376794	4357139	200	75	Xhcq
70110601	376850	4357235	230	65	Xhcq
70110602	376921	4357281	240	75	Xhcq
70110603	376949	4357294	245	75	Xhcq
70110604	377056	4357284	245	70	Xhcq
70110607	377301	4357114	250	90	Xhcq
70110608	377329	4357113	50	70	Xhcq
70110609	377355	4357103	75	85	Xhcq
70210703	377771	4357206	230	85	Xhcq
70210705	377668	4357384	45	75	Xhcq
70210706	377647	4357439	260	80	Xhcq
70210707	377629	4357458	270	90	Xhcq
70210708	377580	4357447	260	80	Xhcq
70210802	377683	4357754	275	45	Xhcq
70210803	377728	4357766	330	50	Xhcq
70210804	377741	4357757	5	65	Xhcq
70210805	377858	4357709	0	0	Xhcq
70210806	377894	4357694	295	50	Xhcq

70210902	378081	4357690	285	30	Xhcq
70210904	378163	4357672	315	40	Xhcq
70210905	378192	4357682	220	25	Xhcq
70210906	378133	4357640	310	27	Xhcq
70210907	378201	4357390	245	40	Xhcq
70210908	378194	4357236	245	70	Xhcq
70210909	378127	4357174	75	90	Xhcq
71211803	371309	4357511	80	85	Xhcq
71211804	371237	4357480	235	65	Xhcq
71211806	371311	4357428	75	90	Xhcq
71211901	371235	4357337	70	90	Xhcq
71211905	371119	4357168	20	60	Xhcq
71212001	371065	4356992	255	80	Xhcq
71212202	370923	4357246	75	90	Xhcq
71212203	371211	4357450	75	85	Xhcq
71212205	371409	4357594	270	85	Xhcq
71312403	371931	4357722	100	85	Xhcq
71312404	372076	4357786	105	80	Xhcq
71612602	379196	4356012	233	75	Xhcq
71612603	379202	4356009	210	85	Xhcq
71712706	378489	4357893	74	86	Xhcq
71712803	378138	4358137	310	25	Xhcq
71712804	378130	4358201	322	50	Xhcq
71712805	378042	4358343	142	80	Xhcq
272000202	375247	4357688	105	80	Xhcq
272000204	375266	4357503	95	90	Xhcq
272000301	375203	4357076	87	80	Xhcq
272000302	375222	4357058	90	90	Xhcq
272000303	375288	4356944	80	90	Xhcq
272000305	375312	4356736	260	80	Xhcq
272000306	375290	4356608	135	85	Xhcq
272000307	375267	4356547	105	90	Xhcq
272000308	375221	4356369	255	70	Xhcq
272000310	375157	4356281	326	65	Xhcq
272100401	374341	4355335	155	65	Xhcq
272100501	374385	4355471	108	30	Xhcq
272100502	374426	4355475	208	30	Xhcq
272500801	373398	4356607	180	25	Xhcq
272500802	373442	4356675	300	20	Xhcq
272500803	373535	4356798	350	20	Xhcq
272500804	373617	4356939	330	35	Xhcq
272500806	373770	4357291	250	80	Xhcq
272500807	373843	4357516	205	90	Xhcq
272500808	373843	4357516	135	85	Xhcq

272500810	373866	4357679	95	90	Xhcq
272500811	373871	4357713	280	85	Xhcq
272500812	373898	4357827	70	90	Xhcq
272500902	373316	4357644	250	85	Xhcq
272500903	373312	4357515	240	90	Xhcq
272500904	373271	4357397	115	80	Xhcq
272601002	371825	4353029	186	80	Xhcq
272601202	370992	4355132	120	65	Xhcq
272601203	370947	4355147	115	75	Xhcq
272601209	372990	4355964	105	60	Xhcq
272601210	372961	4355873	110	75	Xhcq
272601211	372994	4355914	95	60	Xhcq
272601212	373019	4355952	110	40	Xhcq
272601214	373153	4356014	95	90	Xhcq
273001301	371563	4357691	235	5	Xhcq
280101303	377919	4359014	331	16	Xhcq
280101305	377929	4358861	32	72	Xhcq
280101308	377568	4358852	335	80	Xhcq
280101401	377439	4358977	17	75	Xhcq
280101402	377423	4358952	350	70	Xhcq
280101411	375297	4359281	80	80	Xhcq
280701502	377956	4358478	192	42	Xhcq
280701503	377860	4358449	340	46	Xhcq
280701504	377762	4358333	323	35	Xhcq
280701506	377698	4358271	325	75	Xhcq
280701512	377328	4358012	305	70	Xhcq
280901605	377175	4358283	295	70	Xhcq
280901606	377210	4358272	340	90	Xhcq
280901608	377275	4358255	0	60	Xhcq
280901611	377352	4358364	315	60	Xhcq
280901612	377375	4358400	355	65	Xhcq
280901701	377443	4358506	85	55	Xhcq
7261602701	371333	4357488	65	72	Xhcq
7261602702	371378	4357432	71	83	Xhcq
7261602705	371435	4357375	231	80	Xhcq
7261602802	371364	4357247	66	18	Xhcq
7261602803	371301	4357162	256	72	Xhcq
7271603506	370699	4356938	71	73	Xhcq
7271603701	370673	4356933	70	67	Xhcq
7271603704	370762	4356907	259	74	Xhcq
7291604309	374235	4357550	251	72	Xhcq
7291604312	374217	4357423	96	79	Xhcq
7291604401	374158	4356859	264	74	Xhcq
7291604404	374089	4356555	274	67	Xhcq

8071605906	376720	4356253	251	70	Xhcq
8071605907	376728	4356283	266	63	Xhcq
8071606001	376730	4356284	256	78	Xhcq
8071606002	376676	4356284	266	72	Xhcq
8071606105	376835	4356680	211	74	Xhcq
8071606108	377182	4356510	276	82	Xhcq
8091606402	377761	4357229	231	88	Xhcq
8091606502	377761	4357229	252	70	Xhcq
8091606504	378085	4357836	218	41	Xhcq
8151606707	379038	4358971	254	55	Xhcq
6090582	374550	4357895	290	90	Xhcq
6090585	374471	4357790	90	85	Xhcq
62508704	374086	4356929	87	80	Xhcq
62508801	374052	4356797	250	75	Xhcq
62508902	374128	4356736	270	55	Xhcq
62508903	374174	4356726	310	80	Xhcq
62508904	3374184	4356734	260	75	Xhcq
62508906	374219	4356769	140	70	Xhcq
62508907	374206	4356794	310	80	Xhcq
62508909	374237	4356840	290	86	Xhcq
62508910	374219	4356864	285	85	Xhcq
62509001	374239	4356865	285	85	Xhcq
62509002	374248	4356884	300	85	Xhcq
62509101	374292	4356978	160	65	Xhcq
62509102	374316	4357009	70	85	Xhcq
62709804	374114	4356511	272	75	Xhcq
62709902	374402	4356446	225	55	Xhcq
63010401	376994	4356270	250	85	Xhcq
63010402	377016	4356310	95	75	Xhcq
63010404	377160	4356385	265	85	Xhcq
63010407	377205	4356557	245	55	Xhcq
70110507	377045	4356756	280	75	Xhcq
70110508	376986	4356747	260	80	Xhcq
70110512	376808	4356754	245	70	Xhcq
70110513	376793	4356792	265	85	Xhcq
70110515	376794	4357139	200	75	Xhcq
70110601	376850	4357235	230	65	Xhcq
70110602	376921	4357281	240	75	Xhcq
70110603	376949	4357294	245	75	Xhcq
70110604	377056	4357284	245	70	Xhcq
70110607	377301	4357114	250	90	Xhcq
70110608	377329	4357113	50	70	Xhcq
70110609	377355	4357103	75	85	Xhcq
70210703	377771	4357206	230	85	Xhcq

70210705	377668	4357384	45	75	Xhcq
70210706	377647	4357439	260	80	Xhcq
70210707	377629	4357458	270	90	Xhcq
70210708	377580	4357447	260	80	Xhcq
70210802	377683	4357754	275	45	Xhcq
70210803	377728	4357766	330	50	Xhcq
70210804	377741	4357757	5	65	Xhcq
70210805	377858	4357709	0	0	Xhcq
70210806	377894	4357694	295	50	Xhcq
70210902	378081	4357690	285	30	Xhcq
70210904	378163	4357672	315	40	Xhcq
70210905	378192	4357682	220	25	Xhcq
70210906	378133	4357640	310	27	Xhcq
70210907	378201	4357390	245	40	Xhcq
70210908	378194	4357236	245	70	Xhcq
70210909	378127	4357174	75	90	Xhcq
71211803	371309	4357511	80	85	Xhcq
71211804	371237	4357480	235	65	Xhcq
71211806	371311	4357428	75	90	Xhcq
71211901	371235	4357337	70	90	Xhcq
71211905	371119	4357168	20	60	Xhcq
71212001	371065	4356992	255	80	Xhcq
71212202	370923	4357246	75	90	Xhcq
71212203	371211	4357450	75	85	Xhcq
71212205	371409	4357594	270	85	Xhcq
71312403	371931	4357722	100	85	Xhcq
71312404	372076	4357786	105	80	Xhcq
71612602	379196	4356012	233	75	Xhcq
71612603	379202	4356009	210	85	Xhcq
71712706	378489	4357893	74	86	Xhcq
71712803	378138	4358137	310	25	Xhcq
71712804	378130	4358201	322	50	Xhcq
71712805	378042	4358343	142	80	Xhcq
272000202	375247	4357688	105	80	Xhcq
272000204	375266	4357503	95	90	Xhcq
272000301	375203	4357076	87	80	Xhcq
272000302	375222	4357058	90	90	Xhcq
272000303	375288	4356944	80	90	Xhcq
272000305	375312	4356736	260	80	Xhcq
272000306	375290	4356608	135	85	Xhcq
272000307	375267	4356547	105	90	Xhcq
272000308	375221	4356369	255	70	Xhcq
272000310	375157	4356281	326	65	Xhcq
272100401	374341	4355335	155	65	Xhcq

272100501	374385	4355471	108	30	Xhcq
272100502	374426	4355475	208	30	Xhcq
272500801	373398	4356607	180	25	Xhcq
272500802	373442	4356675	300	20	Xhcq
272500803	373535	4356798	350	20	Xhcq
272500804	373617	4356939	330	35	Xhcq
272500806	373770	4357291	250	80	Xhcq
272500807	373843	4357516	205	90	Xhcq
272500808	373843	4357516	135	85	Xhcq
272500810	373866	4357679	95	90	Xhcq
272500811	373871	4357713	280	85	Xhcq
272500812	373898	4357827	70	90	Xhcq
272500902	373316	4357644	250	85	Xhcq
272500903	373312	4357515	240	90	Xhcq
272500904	373271	4357397	115	80	Xhcq
272601002	371825	4353029	186	80	Xhcq
272601202	370992	4355132	120	65	Xhcq
272601203	370947	4355147	115	75	Xhcq
272601209	372990	4355964	105	60	Xhcq
272601210	372961	4355873	110	75	Xhcq
272601211	372994	4355914	95	60	Xhcq
272601212	373019	4355952	110	40	Xhcq
272601214	373153	4356014	95	90	Xhcq
273001301	371563	4357691	235	5	Xhcq
280101303	377919	4359014	331	16	Xhcq
280101305	377929	4358861	32	72	Xhcq
280101308	377568	4358852	335	80	Xhcq
280101401	377439	4358977	17	75	Xhcq
280101402	377423	4358952	350	70	Xhcq
280101411	375297	4359281	80	80	Xhcq
280701502	377956	4358478	192	42	Xhcq
280701503	377860	4358449	340	46	Xhcq
280701504	377762	4358333	323	35	Xhcq
280701506	377698	4358271	325	75	Xhcq
280701512	377328	4358012	305	70	Xhcq
280901605	377175	4358283	295	70	Xhcq
280901606	377210	4358272	340	90	Xhcq
280901608	377275	4358255	0	60	Xhcq
280901611	377352	4358364	315	60	Xhcq
280901612	377375	4358400	355	65	Xhcq
280901701	377443	4358506	85	55	Xhcq
7261602302	372096	4358644	253	56	Ygs
7261602303	372096	4358644	253	64	Ygs
7261602306	372036	4358290	216	74	Ygs

7261602703	371400	4357400	176	90	Ygs
7261602704	371400	4357400	201	90	Ygs
7271603302	371154	4356618	252	86	Ygs
7271603401	371071	4356596	75	72	Ygs
7271603402	370944	4356638	250	81	Ygs
7271603403	370865	4356669	260	48	Ygs
7271603503	370711	4356856	228	72	Ygs
7271603603	370572	4357009	245	85	Ygs
7271603709	371373	4356869	282	59	Ygs
7271603711	371499	4356810	276	85	Ygs
7271603712	371603	4356780	254	68	Ygs
7271603713	371639	4356762	250	71	Ygs
7271603716	372169	4356897	274	53	Ygs
7271603804	371804	4356922	268	49	Ygs
7271603805	371724	4356823	269	54	Ygs
7291604311	374226	4357508	272	83	Ygs
7291604314	374149	4357225	261	87	Ygs
7291604405	373998	4356392	288	43	Ygs
7291604406	373962	4356293	90	81	Ygs
7291604407	373994	4356159	290	41	Ygs
7291604409	374052	4355884	277	51	Ygs
7291604501	374289	4355649	235	33	Ygs
7291604506	373544	4352780	281	35	Ygs
7291604507	373413	4352647	272	59	Ygs
8021604801	374140	4347340	46	90	Ygs
8021604802	374140	4347340	246	71	Ygs
8021604803	373995	4347290	194	73	Ygs
8021604804	373284	4347149	218	76	Ygs
8021604805	373150	4347110	345	46	Ygs
8021604901	372932	4347210	338	49	Ygs
8021604902	372059	4346382	338	0	Ygs
8031605203	372511	4351438	135	57	Ygs
8031605303	372657	4351236	158	90	Ygs
8031605305	376055	4347825	151	80	Ygs
8031605401	376085	4347059	187	78	Ygs
8031605402	377548	4346139	222	72	Ygs
8031605403	375618	4347062	11	4	Ygs
8031605405	374211	4347449	293	67	Ygs
8051605501	378895	4352492	131	12	Ygs
8051605502	378746	4352788	73	32	Ygs
8051605503	378317	4353288	136	67	Ygs
8051605602	378068	4353534	226	51	Ygs
8051605603	378103	4353597	81	78	Ygs
8051605701	378290	4353853	290	49	Ygs

8051605702	374283	4347343	85	78	Ygs
8071605802	377184	4355651	310	75	Ygs
8071605804	377033	4355642	117	78	Ygs
8071605901	376779	4355858	274	35	Ygs
8071605903	376730	4355981	271	56	Ygs
8161607005	369065	4358152	36	72	Ygs
7261603205	371262	4356935	236	50	Yhd
7271603405	370804	4356799	263	75	Yhd
7291604308	374240	4357580	266	85	Yhd
7261602910	371336	4357094	151	73	Yint
7261602911	371336	4357094	231	53	Yint
7261602913	371336	4357094	178	68	Yint
7261602914	371336	4357094	225	73	Yint
7261602915	371336	4357094	134	63	Yint
7261602916	371336	4357094	160	76	Yint
7261603105	371336	4357094	182	78	Yint
7261603106	371336	4357094	259	79	Yint
7261603107	371336	4357094	74	71	Yint
7261603108	371336	4357094	248	30	Yint
7261603109	371336	4357094	201	75	Yint
7261603110	371336	4357094	150	70	Yint
7261602305	372042	4358317	256	85	Yml
7261602401	371956	4358192	76	84	Yml
7261602402	371956	4358192	82	75	Yml
7261602501	371854	4358113	81	85	Yml
7261602502	371763	4358034	72	90	Yml
7261602601	371726	4358005	253	84	Yml
7261602602	371726	4358005	251	85	Yml
7261602604	371589	4357784	66	80	Yml
7261602801	371450	4357326	256	80	Yml
7261602804	371311	4357161	86	76	Yml
7261602805	371336	4357094	70	70	Yml
7261602901	371336	4357094	281	60	Yml
7261602906	371336	4357094	196	65	Yml
7261602907	371336	4357094	186	74	Yml
7261602908	371336	4357094	267	38	Yml
7261603001	371336	4357094	129	90	Yml
7261603101	371336	4357094	91	82	Yml
7261603102	371336	4357094	206	90	Yml
7261603103	371336	4357094	246	43	Yml
7261603104	371336	4357094	169	80	Yml
7261603201	371310	4357036	239	49	Yml
7261603202	371310	4357036	6	58	Yml
7261603203	371310	4357036	270	60	Yml

7271603602	370672	4356954	271	74	Yml
7271603707	370897	4356814	268	86	Yml
7271603802	371869	4356945	263	51	Yml
7281603802	371315	4357426	262	76	Yml
7281603903	371318	4357443	247	84	Yml
7291604305	374404	4357604	81	88	Yml
7291604508	373226	4352618	129	77	Yml
8031605102	374456	4349739	216	90	Yml
8071606101	376811	4356564	263	82	Yml
8091606403	377761	4357229	250	74	Yml
8091606501	377761	4357229	256	64	Yml
8151606702	380059	4358862	274	44	Yml
8151606704	380059	4358862	275	43	Yml
8151606706	379038	4358971	259	67	Yml
8151606708	379038	4358971	242	67	Yml
8151606801	379067	4359042	318	37	Yml
8151606802	379067	4359042	317	36	Yml
8151606805	379902	4359340	321	26	Yml
8151606902	361573	4356248	57	36	Yml
8161607002	368637	4358528	73	85	Yml
8161607004	368637	4358528	250	70	Yml
8161607101	369318	4358004	1	82	Yml
8161607201	369422	4357947	109	16	Yml
8161607202	369422	4357947	81	23	Yml
8171607404	369395	4358050	63	45	Yml
8171607501	369395	4358050	61	46	Yml
8171607502	369465	4358004	67	35	Yml
8171607504	369546	5467847	69	36	Yml
8171607505	369556	4357819	75	48	Yml
8171607601	369528	4357754	88	39	Yml
8171607602	369550	4357725	58	62	Yml
8171607603	369550	4357725	87	44	Yml
8171607604	369550	4357725	74	53	Yml
8171607605	369541	4357694	61	71	Yml
6170745	375333	4358502	118	81	Yml
62408104	374074	4357730	262	82	Yml
6170745	375333	4358502	118	81	Yml
62408104	374074	4357730	262	82	Yml
8091606305	377781	4357104	288	46	Yml Leucosome
8091606306	377781	4357104	274	47	Yml Leucosome
8091606307	377781	4357104	262	47	Yml Leucosome
8151606703	380059	4358862	286	38	Yml Leucosome
70210803	377728	4357766	330	50	Ymyl
70210804	377741	4357757	5	65	Ymyl

70210805	377858	4357709	0	0	Ymyl
70210806	377894	4357694	295	50	Ymyl
70210807	377917	4357695	280	20	Ymyl
70210902	378081	4357690	285	30	Ymyl
70210904	378163	4357672	315	40	Ymyl
70210906	378133	4357640	310	27	Ymyl
71712705	378505	4357887	55	85	Ymyl
71712707	378366	4357943	240	35	Ymyl
71712801	378341	4357958	265	55	Ymyl
71712803	378138	4358137	310	25	Ymyl
71712804	378130	4358201	322	50	Ymyl
71712805	378042	4358343	142	80	Ymyl
71712806	378066	4358433	268	30	Ymyl
280701502	377956	4358478	192	42	Ymyl
281402201	379585	4359298	267	74	Ymyl
281402203	379402	4359454	261	79	Ymyl
8071606001	376730	4356284	256	78	Ymyl
8091606503	378071	4357669	248	45	Ymyl
8151606705	379038	4358971	249	76	Ymyl
8151606803	379075	4359055	308	30	Ymyl
8161607301	369422	4357947	90	17	Ymyl
70210803	377728	4357766	330	50	Ymyl
70210804	377741	4357757	5	65	Ymyl
70210805	377858	4357709	0	0	Ymyl
70210806	377894	4357694	295	50	Ymyl
70210807	377917	4357695	280	20	Ymyl
70210902	378081	4357690	285	30	Ymyl
70210904	378163	4357672	315	40	Ymyl
70210906	378133	4357640	310	27	Ymyl
71712705	378505	4357887	55	85	Ymyl
71712707	378366	4357943	240	35	Ymyl
71712801	378341	4357958	265	55	Ymyl
71712803	378138	4358137	310	25	Ymyl
71712804	378130	4358201	322	50	Ymyl
71712805	378042	4358343	142	80	Ymyl
71712806	378066	4358433	268	30	Ymyl
280701502	377956	4358478	192	42	Ymyl
281402201	379585	4359298	267	74	Ymyl
281402203	379402	4359454	261	79	Ymyl
8071606001	376730	4356284	256	78	Ymyl
8091606503	378071	4357669	248	45	Ymyl
8151606705	379038	4358971	249	76	Ymyl
8151606803	379075	4359055	308	30	Ymyl
8161607301	369422	4357947	90	17	Ymyl

7281604104	374741	4357702	352	84	Ypst

APPENDIX C

LINEATIONS

ID	Easting	Northing	Plunge	Bearing	Rock Type
8151606803	379075	4359055	12	338	bg
8161607301	369422	4357947	25	185	bg
7261602706	371466	4357357	80	0	hblg
7261602707	371466	4357357	70	81	hblg
7261603205	371262	4356935	85	326	hd
7291604302	374537	4357604	59	349	hd
7261602402	371956	4358192	45	246	ml
7261602403	371956	4358192	75	176	ml
7261602501	371854	4358113	75	181	ml
7261602502	371763	4358034	68	21	ml
7261602601	371726	4358005	47	6	ml
7261602602	371726	4358005	65	331	ml
7261602603	371726	4358005	48	341	ml
7261602604	371589	4357784	72	6	ml
7261602801	371450	4357326	60	26	ml
7261602804	371311	4357161	80	16	ml
7261602902	371336	4357094	86	171	ml
7261602903	371336	4357094	83	166	ml
7261602904	371336	4357094	60	331	ml
7261602905	371336	4357094	70	257	ml
7261602909	371336	4357094	81	175	ml
7271603505	370711	4356856	75	328	ml
7271603707	370897	4356814	78	1	ml
7271603802	371869	4356945	49	9	ml
7281603802	371315	4357426	60	2	ml
7281603903	371318	4357443	55	326	ml
7281603904	371318	4357443	78	293	ml
7281604102	374741	4357702	77	341	ml
7281604103	374741	4357702	70	341	ml
7291604305	374404	4357604	74	344	ml
7291604307	374248	4357589	78	7	ml
7291604310	374235	4357550	73	351	ml
8071606101	376811	4356564	78	26	ml
8071606102	376811	4356564	63	10	ml
8071606103	376811	4356564	68	6	ml
8091606303	377781	4357104	58	347	ml
8091606304	377781	4357104	66	354	ml
8091606501	377761	4357229	62	343	ml
8091606601	378089	4357828	48	338	ml
8091606602	378089	4357828	6	346	ml
8151606702	380059	4358862	32	7	ml
8151606704	380059	4358862	38	345	ml
8151606706	379038	4358971	49	313	ml

8151606708	379038	4358971	58	334	ml
8151606801	379067	4359042	13	326	ml
8151606802	379067	4359042	13	331	ml
8151606805	379902	4359340	12	344	ml
8151606901	361573	4356248	22	73	ml
8151606902	361573	4356248	2	59	ml
8161607002	368637	4358528	67	168	ml
8161607003	368637	4358528	65	22	ml
8161607004	368637	4358528	74	16	ml
8161607006	369318	4358004	60	156	ml
8161607007	369318	4358004	63	161	ml
8161607008	369318	4358004	60	198	ml
8161607009	369318	4358004	64	248	ml
8161607101	369318	4358004	75	203	ml
8161607201	369422	4357947	18	182	ml
8161607202	369422	4357947	18	181	ml
8161607302	369393	4357932	20	218	ml
8171607401	369364	4358027	21	206	ml
8171607402	369364	4358027	4	206	ml
8171607403	369364	4358027	21	203	ml
8171607404	369395	4358050	22	216	ml
8171607501	369395	4358050	24	219	ml
8171607502	369465	4358004	24	212	ml
8171607503	369465	4358004	18	187	ml
8171607504	369546	5467847	14	179	ml
8171607505	369556	4357819	55	182	ml
8171607506	369556	4357819	43	192	ml
8171607507	369556	4357819	54	188	ml
8171607601	369528	4357754	25	208	ml
8171607602	369550	4357725	45	154	ml
8171607603	369550	4357725	43	190	ml
8171607604	369550	4357725	29	160	ml
8171607605	369541	4357694	64	167	ml
8151606705	379038	4358971	61	317	myl
7261602912	371336	4357094	53	348	vein
8161607401	369393	4357932	22	194	ygs

APPENDIX D

TITANIQ DATA

Day 2 Aggregation Off

				ELEM:	Ti PPM	ti ka	Ti PPM
				BGD:		MAN	
				SPEC:		1	
				CRYST:		PET	
	SAMPLE	NUMBER	LINE			Ti WT%	
	Quartz Harvard (521	138	99	-2		-0.00015	-1
	Quartz Harvard (521	138	100	-1		-0.00007	0
Average	0	138	99.5	**-1**		-0.00011	**0**
StdDev	0	0	0.707107	1		0.000061	1
StdErr	0	0	0.5			0.000043	
	Rutile, synthetic - SK	139	101	600219		60.0219	599439
	Rutile, synthetic - SK	139	102	600020		60.002	600080
Average	0	139	101.5	**600120**		60.01197	**599760**
StdDev	0	0	0.707107	141		0.014048	453
StdErr	0	0	0.5	141		0.009933	453
	Corundum, synthetic	148	103	156		0.015551	125
	Corundum, synthetic	148	104	157		0.015707	125
Average	0	148	103.5	**156**		0.015629	**125**
StdDev	0	0	0.707107	1		0.00011	0
StdErr	0	0	0.5	1		0.000078	0
	UO SiO2 for blank (st	10	105	-0.2		-0.00002	-6.7
	UO SiO2 for blank (st	10	106	-2.4		-0.00024	-14.7
	UO SiO2 for blank (st	10	107	-7.2		-0.00072	3.9
	UO SiO2 for blank (st	10	108	9.6		0.000955	7.4
	UO SiO2 for blank (st	10	109	7.3		0.000733	-0.5
	UO SiO2 for blank (st	10	110	8.4		0.00084	14.4
	UO SiO2 for blank (st	10	111	-1.9		-0.00019	12.8
	UO SiO2 for blank (st	10	112	-3.8		-0.00038	-5.0
Average	0	10	108.5	**1.2**		0.000121	**1.4**
StdDev	0	0	2.44949	6.3		0.000633	10.1
StdErr	0	0	0.866025	1		0.000224	13
	9ZP-013 Quartz grair	11	113	11		0.001102	28
	9ZP-013 Quartz grair	11	114	7		0.000677	15
	9ZP-013 Quartz grair	11	115	7		0.000724	35

Average	0	11	114	**8**	0.000834	**26**
StdDev	0	0	1	2	0.000233	10
StdErr	0	0	0.57735	0	0.000135	15
	9ZP-013 Quartz grair	12	116	139	0.01385	170
	9ZP-013 Quartz grair	12	117	151	0.015062	156
	9ZP-013 Quartz grair	12	118	102	0.010203	111
	9ZP-013 Quartz grair	12	119	129	0.012864	146
	9ZP-013 Quartz grair	12	120	310	0.031023	318
Average	0	12	118	**166**	0.0166	**180**
StdDev	0	0	1.581139	83	0.008259	80
StdErr	0	0	0.707107	128	0.003693	122
	9ZP-013 Quartz grair	13	121	174	0.017407	178
	9ZP-013 Quartz grair	13	122	48	0.004798	47
	9ZP-013 Quartz grair	13	123	22	0.002209	49
	9ZP-013 Quartz grair	13	124	16	0.001553	33
Average	0	13	122.5	**65**	0.006492	**77**
StdDev	0	0	1.290994	74	0.00741	68
StdErr	0	0	0.645497	5	0.003705	11
	9ZP-013 Quartz grair	14	125	302	0.030211	315
	9ZP-013 Quartz grair	14	126	64	0.006422	47
	9ZP-013 Quartz grair	14	127	49	0.004884	43
Average	0	14	126	**138**	0.013839	**135**
StdDev	0	0	1	142	0.014199	156
StdErr	0	0	0.57735	11	0.008198	3
	9ZP-013 Quartz grair	15	128	19	0.001867	35
	9ZP-013 Quartz grair	15	129	89	0.008875	86
	9ZP-013 Quartz grair	15	130	102	0.01024	141
	9ZP-013 Quartz grair	15	131	142	0.014199	162
	9ZP-013 Quartz grair	15	132	110	0.010974	95
	9ZP-013 Quartz grair	15	133	62	0.006165	84
Average	0	15	130.5	**87**	0.00872	**101**
StdDev	0	0	1.870829	43	0.004264	45
StdErr	0	0	0.763763	34	0.001741	8
	9ZP-013 Quartz grair	16	134	11	0.001094	2
Average	0	16	134		0.001094	
StdDev	0	4	11.57584		0.033072	
StdErr	0	0	0		0	

	9ZP-013 Quartz grair	17	135	12	0.001161	-4
	9ZP-013 Quartz grair	17	136	11	0.00114	12
Average	0	17	135.5	**12**	0.001151	**4**
StdDev	0	0	0.707107	0	0.000015	12
StdErr	0	0	0.5		0.000011	
	9ZP-013 Quartz grair	18	137	18	0.001761	9
	9ZP-013 Quartz grair	18	138	20	0.00201	21
Average	0	18	137.5	**19**	0.001886	**15**
StdDev	0	0	0.707107	2	0.000176	8
StdErr	0	0	0.5		0.000124	
	UO SiO2 for blank (st	19	139	18.0	0.001802	7.1
	UO SiO2 for blank (st	19	140	-3.2	-0.00032	-10.5
	UO SiO2 for blank (st	19	141	6.4	0.000641	-17.6
	UO SiO2 for blank (st	19	142	-2.3	-0.00023	22.9
	UO SiO2 for blank (st	19	143	5.3	0.000527	3.5
	UO SiO2 for blank (st	19	144	-0.5	-0.00005	20.0
	UO SiO2 for blank (st	19	145	16.4	0.001644	-6.4
	UO SiO2 for blank (st	19	146	8.8	0.000875	2.3
Average	0	19	142.5	**6.1**	0.000612	**2.6**
StdDev	0	0	2.44949	8.1	0.000808	14.1
StdErr	0	0	0.866025	5	0.000286	6

		Xenon	Xenon
	SPEC:	1	**2**
	CRYST:	**PET**	**LiF**
Blank Standard Initial Set	Average	1.2	1.4
	StdDev	6.3	10.1
Blank Standard Ending Set	Average	6.1	2.6
	StdDev	8.1	14.1
	Change	4.9	1.2
		Drift not significant (less than 1 sigma)	Drift not significant (less than 1 sigma)

ti ka MAN 2 LiF	Ti PPM	ti ka MAN 4 LiF	i PPM	ti ka MAN 5 PET	Ti PPM	ti ka MAN 6 PET	Al ppm	al ka MAN 3 RAP
Ti WT%		Ti WT%		Ti WT%		Ti WT%		Al WT%
-0.00014	-13	-0.0013	0	0	28	0.002763	15	0.001466
0.000046	-4	-0.00039	0	0	22	0.002249	23	0.002279
-0.00005	**-8**	-0.00085	**0**	0	**25**	0.002506	**19**	0.001873
0.000134	6	0.000644	0	0	4	0.000363	6	0.000575
0.000095		0.000455		0		0.000257		0.000407
59.9439	599984	59.9984	0	0	605106	60.5106	-22	-0.00224
60.008	599485	59.9485	0	0	594466	59.4466	-3	-0.00026
59.97595	**599735**	59.97343	**0**	0	**599786**	59.97861	**-13**	-0.00125
0.045322	353	0.035325	0	0	7524	0.752342	14	0.001401
0.032047	353	0.024979	0	0	7524	0.531986	14	0.00099
0.012504	134	0.013381	0	0	81	0.008122	525076	52.5076
0.012477	126	0.012578	0	0	73	0.007314	533430	53.343
0.01249	**130**	0.01298	**0**	0	**77**	0.007718	**529253**	52.92528
0.000019	6	0.000568	0	0	6	0.000571	5907	0.590663
0.000013	6	0.000401	0	0	6	0.000404	5907	0.417662
-0.00067	7.5	0.000747	0.0	0	-1.0	-0.0001	16.6	0.00166
-0.00147	17.4	0.001735	0.0	0	1.5	0.000145	26.1	0.002613
0.000391	7.8	0.000777	0.0	0	1.1	0.000111	9.3	0.000932
0.000736	-19.0	-0.0019	0.0	0	-0.2	-0.00002	21.6	0.002162
-0.00005	1.2	0.000123	0.0	0	3.0	0.000303	12.1	0.001208
0.001439	4.3	0.000427	0.0	0	-0.2	-0.00002	16.3	0.001628
0.001282	-3.3	-0.00033	0.0	0	-0.2	-0.00002	9.0	0.000901
-0.0005	-5.1	-0.00051	0.0	0	6.8	0.000679	8.6	0.000864
0.000145	**1.3**	0.000133	**0.0**	0	**1.3**	0.000133	**15.0**	0.001496
0.001007	10.8	0.001082	0.0	0	2.5	0.000255	6.4	0.000643
0.000356	1	0.000383	0	0	5	0.00009	0	0.000227
0.002773	12	0.001199	0	0	17	0.001715	38	0.003778
0.001495	20	0.001974	0	0	26	0.002593	35	0.003489
0.003548	21	0.002125	0	0	24	0.002403	79	0.007879

0.002605	**18**	0.001766	**0**	0	**22**	0.002237	**50**	0.005049
0.001037	5	0.000497	0	0	5	0.000462	25	0.002456
0.000599	1	0.000287	0	0	1	0.000267	31	0.001418
0.016986	175	0.01746	0	0	99	0.009944	207	0.02073
0.015592	185	0.018508	0	0	99	0.009947	88	0.008798
0.011077	104	0.01036	0	0	70	0.007017	204	0.020378
0.014576	153	0.01526	0	0	87	0.008661	156	0.015582
0.03184	334	0.03344	0	0	194	0.019401	116	0.011628
0.018014	**190**	0.019005	**0**	0	**110**	0.010994	**154**	0.015423
0.008032	87	0.008657	0	0	49	0.004851	53	0.005269
0.003592	129	0.003872	0	0	76	0.00217	28	0.002356
0.017758	202	0.02016	0	0	99	0.009918	18	0.001763
0.004737	48	0.004764	0	0	29	0.002868	19	0.001911
0.004912	27	0.002746	0	0	20	0.002035	-14	-0.00137
0.003289	25	0.002474	0	0	21	0.002057	-12	-0.0012
0.007674	**75**	0.007536	**0**	0	**42**	0.004219	**3**	0.000276
0.006762	85	0.008478	0	0	38	0.003819	18	0.001805
0.003381	2	0.004239	0	0	0	0.001909	1	0.000903
0.031527	299	0.029888	0	0	182	0.018161	129	0.012922
0.004692	55	0.005492	0	0	47	0.004729	25	0.002518
0.004263	37	0.003701	0	0	45	0.004501	14	0.001365
0.013494	**130**	0.013027	**0**	0	**91**	0.00913	**56**	0.005602
0.015619	146	0.01463	0	0	78	0.007822	64	0.006366
0.009017	13	0.008447	0	0	2	0.004516	8	0.003675
0.003517	43	0.004341	0	0	44	0.004425	36	0.003637
0.008579	106	0.010635	0	0	75	0.007533	78	0.007819
0.01412	105	0.010524	0	0	89	0.0089	50	0.004982
0.016211	154	0.01544	0	0	110	0.011049	18	0.001753
0.009482	103	0.010329	0	0	77	0.007693	36	0.003572
0.00841	73	0.007251	0	0	61	0.006061	41	0.004077
0.010053	**98**	0.009753	**0**	0	**76**	0.00761	**43**	0.004307
0.004525	37	0.003731	0	0	23	0.002282	20	0.002018
0.001847	22	0.001523	0	0	12	0.000932	4	0.000824
0.000188	6	0.000638	0	0	25	0.002467	35	0.003515
0.000188		0.000638		0		0.002467		0.003515
0.013722		0.025266		0		0.049669		0.059288
0		0		0		0		0

-0.00042	17	0.001656	0	0	30	0.002981	186	0.0186
0.00121	-11	-0.00111	0	0	30	0.002999	1287	0.128685
0.000397	**3**	0.000274	**0**	0	**30**	0.00299	**736**	0.073643
0.001149	20	0.001954	0	0	0	0.000013	778	0.077842
0.000813		0.001382		0		0.000009		0.055042
0.000905	20	0.001989	0	0	29	0.00292	35	0.003489
0.002069	10	0.001016	0	0	32	0.003223	25	0.002454
0.001487	**15**	0.001503	**0**	0	**31**	0.003072	**30**	0.002971
0.000823	7	0.000688	0	0	2	0.000214	7	0.000732
0.000582		0.000486		0		0.000152		0.000518
0.000706	-6.7	-0.00067	0.0	0	22.1	0.002214	2.5	0.000253
-0.00105	10.3	0.001034	0.0	0	30.1	0.003007	1.4	0.000141
-0.00176	10.5	0.00105	0.0	0	25.8	0.002575	-3.7	-0.00037
0.002286	-2.3	-0.00023	0.0	0	25.2	0.00252	13.6	0.001357
0.000347	-3.5	-0.00035	0.0	0	29.7	0.002974	5.6	0.000555
0.001998	10.9	0.001093	0.0	0	25.6	0.00256	-6.3	-0.00063
-0.00064	5.8	0.000578	0.0	0	25.7	0.002565	-12.9	-0.00129
0.000231	7.3	0.000729	0.0	0	33.9	0.003388	-4.3	-0.00043
0.000264	**4.0**	0.000405	**0.0**	0	**27.3**	0.002725	**-0.5**	-0.00005
0.001412	7.1	0.000711	0.0	0	3.7	0.00037	8.1	0.00081
0.000499	1	0.000251	0	0	6	0.000131	6	0.000286

Xenon	P-10	P-10	P-10	
4	**5**	**6**	**3**	0
LiF	**PET**	**PET**	**RAP**	EDS
1.3		1.3	15.0	
10.8		2.5	6.4	
4.0		27.3	-0.5	
7.1		3.7	8.1	
2.7		25.9	-15.5	

Drift not significant (less than 1 sigma)

Drift significant

6 sigma!